**Coastal Systems Station, Dahlgren Division
Naval Surface Warfare Center**
Panama City, Florida 32407-7001

TECHNICAL REPORT
CSS TR 456-93
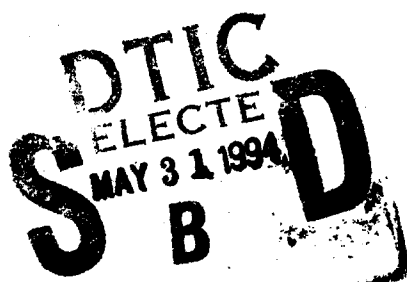
DECEMBER 1993

AD-A279 824

IDENTIFICATION OF UNDERWATER TARGETS VIA ACTIVE SONAR

GLENN N. REID AND
DR. CHUNG TSUI (UNIVERSITY OF MARYLAND)

DTIC
ELECTE
MAY 3 1 1994
S B D

94-15955

94 5 26 11 8

Coastal Systems Station, Dahlgren Division
Naval Surface Warfare Center
PANAMA CITY, FLORIDA 32407-7001

CAPT D. C. STEERE,
USN

MR. TED C. BUCKLEY
Executive Director

ADMINISTRATIVE INFORMATION

Released by
D. P. SKINNER, Head
Coastal Research and
Technology Department

Under authority of
T. C. BUCKLEY
Executive Director

REPORT DOCUMENTATION PAGE

Public reporting burden for this collection of information is estimated to average 1 hour per response, including the time for reviewing instructions, searching existing data sources, gathering and maintaining the data needed, and completing and reviewing the collection of information. Send comments regarding this burden estimate or any other aspect of this collection of information, including suggestions for reducing this burden, to Washington Headquarters Services, Directorate for Information Operations and Reports, 1215 Jefferson Davis Highway, Suite 1204, Arlington, VA 22202-4302, and to the Office of Management and Budget, Paperwork Reduction Project (0704-0188), Washington, DC 20503.

1. AGENCY USE ONLY (Leave blank)	2. REPORT DATE December 1993	3. REPORT TYPE AND DATES COVERED Final

4. TITLE AND SUBTITLE
Identification of Underwater Targets via Active Sonar

5. FUNDING NUMBERS

6. AUTHOR(S)
Glenn N
Glenn N. Reid and Dr. Chung Tsui (University of Maryland)

7. PERFORMING ORGANIZATION NAME(S) AND ADDRESS(ES)

Commanding Officer
CSSDD NSWC
6703 W. Highway 98
Panama City, FL 32407-7001

8. PERFORMING ORGANIZATION REPORT NUMBER

CSS TR 456-93

9. SPONSORING/MONITORING AGENCY NAME(S) AND ADDRESS(ES)

10. SPONSORING/MONITORING AGENCY REPORT NUMBER

11. SUPPLEMENTARY NOTES

12a. DISTRIBUTION/AVAILABILITY STATEMENT
Approved for public release; distribution is unlimited.

12b. DISTRIBUTION CODE

13. ABSTRACT (Maximum 200 words)

The main thrust of this research was to experimentally determine the resonances in cylindrical-like structures. When such a structure is insonified with a single frequency sinusoidal acoustic energy, there will be some deformation of the structure and internal waves will propagate through it. Some waves will travel from one edge, through the center, to the other edge, and be reflected back. Others will travel around the structure circumferentially. If the driving frequency, the radial waves, and the circumferential waves are in phase at the driving point, resonance will occur. The circumferential waves are usually described by sinusoidal functions while the radial waves are described by Bessel and Hankel functions.

14. SUBJECT TERMS

Identification	Underwater	Cylinders	
Active	Sonar	Resonance	Experimental

15. NUMBER OF PAGES
75

16. PRICE CODE

17. SECURITY CLASSIFICATION OF REPORT UNCLASSIFIED	18. SECURITY CLASSIFICATION OF THIS PAGE UNCLASSIFIED	19. SECURITY CLASSIFICATION OF ABSTRACT UNCLASSIFIED	20. LIMITATION OF ABSTRACT SAR

GENERAL INSTRUCTIONS FOR COMPLETING SF 298

The Report Documentation Page (RDP) is used in announcing and cataloging reports. It is important that this information be consistent with the rest of the report, particularly the cover and its title page. Instructions for filling in each block of the form follow. It is important to *stay within the lines* to meet *optical scanning requirements*.

Block 1. Agency Use Only (Leave blank).

Block 2. Report Date. Full publication date including day, month, and year, if available (e.g. 1 Jan 88). Must cite at least the year.

Block 3. Type of Report and Dates Covered. State whether report is interim, final, etc. If applicable, enter inclusive report dates (e.g. 10 Jun 87 - 30 Jun 88).

Block 4. Title and Subtitle. A title is taken from the part of the report that provides the most meaningful and complete information. When a report is prepared in more than one volume, repeat the primary title, add volume number, and include subtitle for the specific volume. On classified documents enter the title classification in parentheses.

Block 5. Funding Numbers. To include contract and grant numbers; may include program element number(s), project number(s), task number(s), and work unit number(s). Use the following labels:

```
C  - Contract      PR - Project
G  - Grant         TA - Task
PE - Program       WU - Work Unit
     Element            Accession No.
```

BLOCK 6. Author(s). Name(s) of person(s) responsible for writing the report, performing the research, or credited with the content of the report. If editor or compiler, this should follow the name(s).

Block 7. Performing Organization Name(s) and Address(es). Self-explanatory.

Block 8. Performing Organization Report Number. Enter the unique alphanumeric report number(s) assigned by the organization performing the report.

Block 9. Sponsoring/Monitoring Agency Name(s) and Address(es). Self-explanatory.

Block 10. Sponsoring/Monitoring Agency Report Number. (If Known)

Block 11. Supplementary Notes. Enter information not included elsewhere such as: Prepared in cooperation with...; Trans. of...; To be published in.... When a report is revised, include a statement whether the new report supersedes or supplements the older report.

Block 12a. Distribution/Availability Statement. Denotes public availability or limitations. Cite any availability to the public. Enter additional limitations or special markings in all capitals (e.g. NOFORN, REL, ITAR).

```
DOD  - See DoDD 5230.24, "Distribution
         Statements on Technical Documents."
DOE  - See authorities.
NASA - See Handbook NHB 2200.2
NTIS - Leave blank.
```

Block 12b. Distribution Code.

```
DOD  - Leave blank.
DOE  - Enter DOE distribution categories
         from the Standard Distribution for
         Unclassified Scientific and Technical
         Reports.
NASA - Leave blank.
NTIS - Leave blank.
```

Block 13. Abstract. Include a brief *(Maximum 200 words)* factual summary of the most significant information contained in the report.

Block 14. Subject Terms. Keywords or phrases identifying major subjects in the report.

Block 15. Number of Pages. Enter the total number of pages.

Block 16. Price Code. Enter appropriate price code *(NTIS only)*

Blocks 17.-19. Security Classifications. Self-explanatory. Enter U.S. Security Classification in accordance with U.S. Security Regulations (i.e., UNCLASSIFIED). If form contains classified information, stamp classification on the top and bottom of the page.

Block 20. Limitation of Abstract. This block must be completed to assign a limitation to the abstract. Enter either UL (unlimited) or SAR (same as report). An entry in this block is necessary if the abstract is to be limited. If blank, the abstract is assumed to be unlimited.

CONTENTS

Accession For
NTIS GRA&I
DTIC TAB
Unannounced
Justification

By
Distribution/
Availability Codes
Dist | Avail and/or Special
A-1

ILLUSTRATIONS

TABLES

CHAPTER 1

INTRODUCTION

The Naval Surface Warfare Center, Dahlgren Division (NSWCDD) has been one of the prime forces behind the resonant scattering theory (RST) venture during the last two decades. NSWCDD patronage and sponsorship led to numerous publications in archive journals[1-36] and in book chapters.[37-39] At least three U. S. Patents[40-42] were granted as a result of research and development (R&D) efforts on the RST and related topics. Notable contributions are attributed to G. Gaunaurd (R42) and collaborators D. Brill (The United States Naval Academy) and H. Uberall (Catholic University of America). Experimental verification and development by the authors of this report started several years ago in the Underwater Systems Department (U). The Instrumentation and Electronics Branch (U42) portion of that department where this work was done was reorganized to the Panama City, Coastal System Station, Code 2620, Mine Systems Branch.

The concept behind active sonar and the RST is deceptively simple and has been known since the advent of classical physics. When a load is applied to a structure, the structure reacts accordingly. According to Newton's laws, objects at rest tend to remain at rest and if in motion, tend to stay in motion. Relating this to a structure, when a sinusoidal load is applied to a structure, most of the energy will be reflected until steady motion is achieved. The body will then vibrate at all the resonant modes that fall within the power spectrum of the load. The energy associated with these modes will be absorbed and stored in the structures and the remainder of the energy will be reflected.

The main thrust of this research was to experimentally determine the resonances in cylindrical like structures. When such a structure is insonified with a single frequency sinusoidal acoustic energy there will be some deformation of the structure and internal waves will propagate through it. Some waves will travel from one edge, through the center, to the other edge, and be reflected back. Others will travel around the structure circumferentially. If the driving frequency, the radial waves, and the circumferential waves are in phase at the driving point, resonance will occur. The circumferential waves are usually described by sinusoidal functions while the radial waves are described by Bessel and Hankel functions. If the incident frequency increases, higher resonance frequencies will occur in both waves, thus indices must be applied. For the circumferential waves the index of n will be used, and for the radial waves l. Since the necessary condition for resonance is that both the circumferential and the radial be excited, resonances are classified by their pairs of indices, (n,l). When the n index is determined experimentally, the number of standing waves developed around the

circumference of the cylinder is known. Basically the resonance of the structure is dependent on the size, shape and material it is manufactured from. A review of theory reveals that the velocity of sound in material is the square root of the ratio of one of the material moduli and the material density $c = \sqrt{E/\rho}$. The wave number of the material is ($k = 2\pi f/c$) and for a cylinder, the radius (a) is the important size, each resonant frequency will provide a data point in the ka domain and a set of these resonances will identify the target. Knowing that targets are only made out of a limited class of materials and a limited number of sizes, a library of resonances for possible targets can be determined theoretically and compared to the measured values.

Stated another way the dynamic response at any point of the structure is the sum of the individual modal responses. These responses, fashioned after the modal power partitions from the total input, are governed by the so-called frequency equation which is a function of the structural parameters and the input frequency. In the cases where one input frequency matches one of the structural natural frequencies, the mode associated with this frequency is vigorously excited to result in a resonance vibration. At resonance, the majority of the input power is directed to this excited mode to sustain its vigorous motion at the expense of the others. Should the input last for a while, the structure will enter into a steady motion. Energy continues to enter the structure only to be reradiated due to the motion of the body, be stored as kinetic energy or be converted into heat through a frictional mechanism internally and is released into the surroundings. At the cessation of the input, the structure will revert to free vibration and the stored energy will eventually be dissipated.

If the assumption is made that the structure in water is lightly damped, this will be discussed later, the behavior of structures underwater is the same as that described in the last paragraphs. When a wave insonifies a target, energy of the wave input penetrates into the target and sets its internal elements in motion. The balance of the insonification is reflected. The reflection yields the bistatic crosssection which can be measured by a hydrophone slowly revolving around the structure at the far field. Normally, the bistatic crosssection has a very complicated pattern because it is a result of a conglomeration of many partial waves scattered by the target at broadside. It also has a large magnitude since most energy is reflected and little penetrates into the target. At a resonant state, the monochromatic bistatic crosssection will display a much simpler, symmetrical pattern known as the "rosetta." This rosetta pattern has a simple mathematical description so an amplitude measured at the maximum value suffices to specify the amount of the reradiated power and, by deduction, the amount which is penetrated into the target. The magnitude of the broadside steady state reflection is expected to be much smaller at resonance since most of the input power is penetrating the target.

The comparison of energy returned from the target at resonance frequency (when it is compliant) and off resonance (when it is rigid) gives rise to the idea of experimentally locating the unique set of resonances which is the signature of the structure. Determining the location of several of these frequencies is sufficient to ascertain the signature for the target identification and classification purposes.

The goal of the investigation reported here was to develop a methodology for the extraction of energy data from the return at resonance and off resonance states such that the signature of a target underwater can be measured. This measured signature contains the resonance frequencies of the target which identifies its shape, size, and composition which can be used for its identification and classification. It was decided that the simplest targets would be used because experimental results can be verified from the readily available predictions of the theory. A successful completion of this endeavor will validate the assumptions and approaches taken in the RST development and will provide a solid foundation for further research directed toward securing signatures for complicated and realistic targets. This has important and practical implications since the more complex or real life targets are impractical to model analytically, the experimental methodology will be the only means of securing the signatures.

The following chapters will provide a brief description of the theoretical approach to the RST solution by way of an example, followed by the experimental arrangements and procedures and by selected experimental results. Recommendation for future investigation is also presented.

CHAPTER 2

RST AND ITS FORMULATION

The equations leading to the RST formulation are derived from standard formulas in linear theories of elasticity on isotropic solids and in linear acoustics in an inviscid fluid media. The two sets of formulas are linked by boundary conditions at the interface, namely, the pressure at the fluid side must be equal to the normal stress in the solid side and the normal displacement at both sides must be equal. In addition, since an inviscid fluid can not sustain shear, the shear stress at the interface must vanish. Solving this boundary-value problem for the pressure distribution in the fluid medium has been performed for many geometrically simple targets such as infinitely long, elastic cylinders,[13,43-48] spheres,[8,15,16,25,31,43,46,49,50] cylindrical shells,[1,4,18,20,21,24,46,51-53] hollow spheres[12,26,32] and spheroids,[34] where the insonification by a plane wave is at a direction perpendicular to a geometrical axis of the target. For an illustration of the analytical approach taken in the past, the solution for a solid cylinder, infinite in length, is presented here in detail. With respect to Figure 2-1, a plane wave impinges on a cylindrical target of radius, a, in a direction perpendicular to its axis which extends to infinity in both directions.
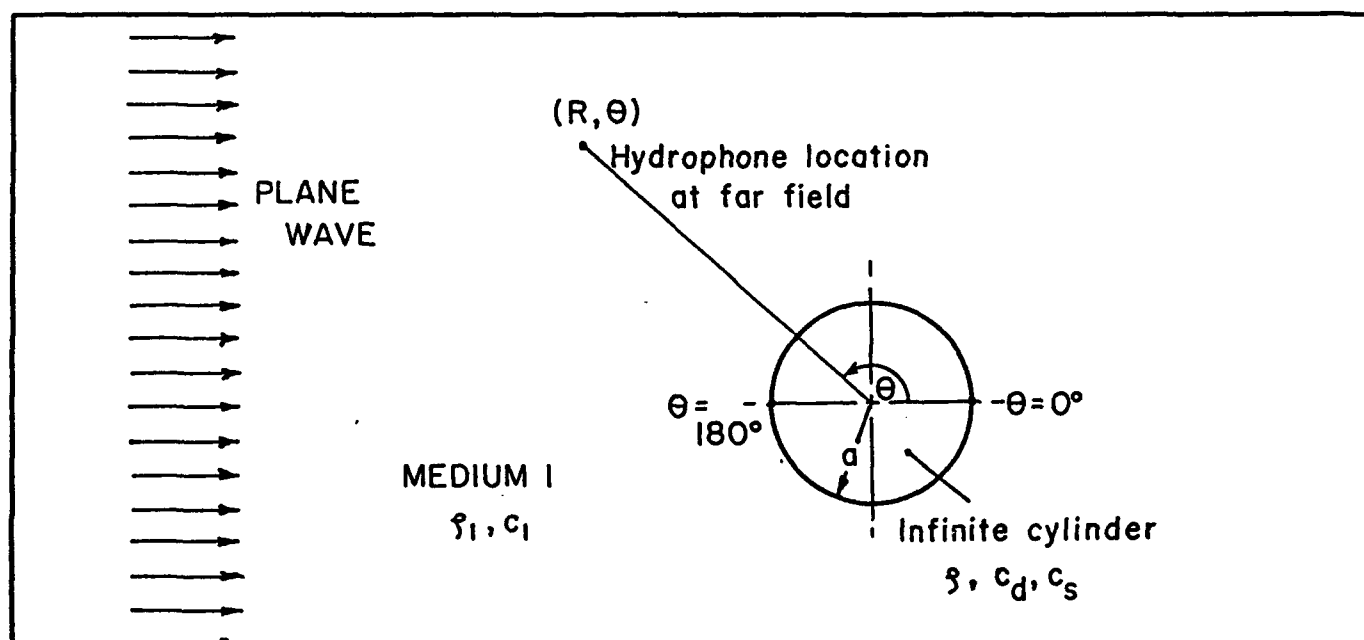
FIGURE 2-1. INSONIFICATION OF A CYLINDER

The sound pressure of interest, p, is two-dimensional, being a function of the distance from the axis, r, and the angular orientation with respect to the direction of propagation of the plane wave, θ. By this definition, the backscattered wave (echo or reflected wave) is at an orientation of $\theta = 180°$ or π radians. In the fluid side, the sound pressure, $p(r, \theta, t)$, is governed by the wave equation in cylindrical coordinates:

$$\frac{\partial^2 p}{\partial r^2} + \frac{1}{r}\frac{\partial p}{\partial r} + \frac{1}{r^2}\frac{\partial^2 p}{\partial \theta^2} - \frac{1}{c^2}\frac{\partial^2 p}{\partial t^2} = 0 \tag{2-1}$$

where c is the speed of wave propagation. Assuming a harmonic solution, the time dependent term in $p(r, \theta)e^{(-i\omega t)}$, where ω is the angular velocity of the incident wave vanishes resulting in the Helmholtz equation:

$$\frac{\partial^2 p_1}{\partial r^2} + \frac{1}{r}\frac{\partial p_1}{\partial r} + \frac{1}{r^2}\frac{\partial^2 p_1}{\partial \theta^2} + k_1^2 p_1 = 0 \tag{2-2}$$

where $k_1 = \omega/c_1$ is the wave number and the subscript 1 is added to designate the fluid medium. The solution of Equation (2-2) is:

$$p_1(r, \theta) = p_0 \sum_{n=0}^{\infty} (i)^n \varepsilon_n [J_n(k_1 r) + b_n H_n^{(1)}(k_1 r)] \cos n\theta \tag{2-3}$$

where n is a positive integer due to circumferential periodicity; $\varepsilon_n = 2$ for $n \neq 0$ and $\varepsilon_0 = 1$. In Equation (2-3), the first term is the incident plane wave of amplitude p_0 and the second term, involving the (complex) Hankel function of the first kind, gives the scattered wave. This term consists of an infinite set of partial waves, each of amplitude b_n whose magnitude can be determined from given boundary conditions. Once b_n is known, the sound pressure at any point in medium 1 and at any time is given by: $p_1(r, \theta)e^{(-i\omega t)}$. As an example, if the boundary at $r = a$ is rigid or immovable, allowing no energy penetration into the solid interior, the sole condition which remains in effect is the vanishing of the normal displacement at the boundary. Mathematically, this is given as $u_1(a, \theta) = 0$ where u_1 is the radial displacement. Then from Equation (2-3), since:

$$u_1(r, \theta) = \frac{1}{\rho_1 \omega^2}\frac{\partial p_1}{\partial r} \tag{2-4}$$

where ρ_1 is the density of the fluid,

$$u_1(r,\theta) = \frac{p_0}{\rho_1 c_1 \omega} \sum_{n=0}^{\infty} (i)^n \varepsilon_n \left[J_n'(k_1 r) + b_n H_n^{(1)'}(k_1 r) \right] \cos n\theta$$

and, at the boundary,

$$u_1(a,\theta) = 0 = \frac{p_0}{\rho_1 c_1 \omega} \sum_{n=0}^{\infty} i^n \varepsilon_n \left[J_n'(k_1 a) + b_n H_n^{(1)'}(k_1 a) \right] \cos n\theta$$

which gives:

$$b_n^{(r)} = -\frac{J_n'(k_1 a)}{H_n^{(1)'}(k_1 a)} \qquad (2-5)$$

The primes designate derivatives with respect to the argument of the function. Thus:

$$p_1^{(r)}(r,\theta) = p_0 \sum_{n=0}^{\infty} (i)^n \varepsilon_n \left[J_n(k_1 r) - \frac{J_n'(k_1 a)}{H_n^{(1)'}(k_1 a)} H_n^{(1)}(k_1 r) \right] \cos n\theta \qquad (2-6)$$

A superscript, (r), is added to designate that the equation is pertaining to a rigid target. If the boundary is nonrigid, hence movable as in the case for what is known as an elastic target, the movement of the boundary creates a stress field within the target. The governing equation, in terms of the particle displacement vector, $\bar{u}$, is:

$$\nabla^2 \bar{u} + \frac{\lambda + \mu}{\mu} \nabla(\nabla \cdot \bar{u}) - \frac{1}{c_s^2} \frac{\partial^2 \bar{u}}{\partial t^2} = 0 \qquad (2-7)$$

where λ and μ are the Lame's constants of the target material whose density is ρ and c_s is the speed of the shear wave, $(c_s = \sqrt{\mu/\rho})$. In solid, there exists additionally a dilatational wave whose speed c_d is given by $c_d = \sqrt{(\lambda + 2\mu)/\rho}$.

It can be shown[54] that the displacement vector, $\bar{u}$, is given by an irrotational potential, ϕ, and a rotational potential, $\bar{\psi}$. For the case of an infinitely long cylinder, the nonvanishing component of the vector $\bar{\psi}$ is ψ_z, its z-component. Each potential satisfies the Helmholtz equation. In summary, we have:

$$\bar{u} = \nabla \phi + \nabla \times \bar{\psi} \qquad (2-8)$$

$$\frac{\partial^2 \phi}{\partial r^2} + \frac{1}{r}\frac{\partial \phi}{\partial r} + \frac{1}{r^2}\frac{\partial^2 \phi}{\partial \theta^2} + k_d^2 \phi = 0 \qquad (2-9)$$

$$\frac{\partial^2 \psi_z}{\partial r^2} + \frac{1}{r}\frac{\partial \psi_z}{\partial r} + \frac{1}{r^2}\frac{\partial^2 \psi_z}{\partial \theta^2} + k_s^2 \psi_z = 0 \qquad (2-10)$$

where $k_d = (\omega/c_d)$ and $k_s = (\omega/c_s)$. Again, the time dependent term $e^{(-i\omega t)}$ is suppressed. The radial displacement, u_r, and the normal and shear stresses within the target, τ_{rr} and $\tau_{r\theta}$ respectively, are given by:

$$u_r = \frac{\partial \phi}{\partial r} + \frac{1}{r}\frac{\partial \psi_z}{\partial \theta} \qquad (2-11)$$

$$\tau_{rr} = -\lambda k_d^2 \phi + 2\mu\left[\frac{\partial^2 \phi}{\partial r^2} + \frac{\partial}{\partial r}\left(\frac{1}{r}\frac{\partial^2 \psi_z}{\partial \theta^2}\right)\right] \qquad (2-12)$$

$$\tau_{r\theta} = \mu\left[2\frac{\partial^2}{\partial r \partial \theta}\left(\frac{\phi}{r}\right) - \left(\frac{\partial^2 \psi_z}{\partial r^2} - \frac{1}{r}\frac{\partial \psi_z}{\partial r} - \frac{1}{r^2}\frac{\partial^2 \psi_z}{\partial \theta^2}\right)\right] \qquad (2-13)$$

The solution of the Helmholtz equations, Equations (2-9) and (2-10), can be given as:

$$\phi(r,\theta) = p_0 \sum_{n=0}^{\infty} i^n \varepsilon_n g_n J_n(k_d r)\cos n\theta \qquad (2-14)$$

$$\psi_z(r,\theta) = p_0 \sum_{n=0}^{\infty} i^n \varepsilon_n h_n J_n(k_s r)\sin n\theta \qquad (2-15)$$

The part of the solution involving the Hankel function, (see Equation (2-3)), must be excluded here due to singularity at the center of the cylinder at $r = 0$. The modal constants g_n and h_n, along with b_n in Equation (2-3) are to be solved by an alternative set of boundary conditions, namely, at $r = a$:

$$\tau_{rr}|_{r=a} = -p_1(a,\theta) \qquad (2-16)$$

$$u_r(a,\theta) = u_1(a,\theta) \qquad (2-17)$$

$$\tau_{r\theta}|_{r=a} = 0 \qquad (2-18)$$

Formally, a set of simultaneous equations involving these modal constants results:

$$d_{11}b_n + d_{12}g_n + d_{13}h_n = A_1 \qquad (2-19a)$$

$$d_{21}b_n + d_{22}g_n + d_{23}h_n = A_2 \qquad (2-19b)$$

$$d_{31}b_n + d_{32}g_n + d_{33}h_n = 0 \qquad (2-19c)$$

where

$$d_{11} = \frac{\rho_1}{\rho}[(k_s a)^2 H_n^{(1)}(k_1 a)] \tag{2-20a}$$

$$d_{12} = 2(k_d a) J_n'(k_d a) - [2n^2 - (k_s a)^2] J_n(k_d a) \tag{2-20b}$$

$$d_{13} = 2n[-(k_s a) J_n'(k_s a) + J_n(k_s a)] \tag{2-20c}$$

$$d_{21} = -(k_1 a) H_n^{(1)'}(k_1 a) \tag{2-20d}$$

$$d_{22} = (k_d a) J_n'(k_d a) \tag{2-20e}$$

$$d_{23} = n J_n(k_s a) \tag{2-20f}$$

$$d_{31} = 0 \tag{2-20g}$$

$$d_{32} = 2n[J_n(k_d a) - (k_d a) J_n'(k_d a)] \tag{2-20h}$$

$$d_{33} = 2(k_s a) J_n'(k_s a) - [2n^2 - (k_s a)^2] J_n(k_s a) \tag{2-20i}$$

Also,

$$A_1 = \frac{\rho_1}{\rho}[(k_s a)^2 J_n(k_1 a)] \tag{2-21a}$$

$$A_2 = (k_1 a) J_n'(k_1 a) \tag{2-21b}$$

Thus by Crammer's rule, b_n is given by:

$$b_n = \frac{B_n}{D_n} \tag{2-22}$$

where B_n and D_n are the determinants:

$$B_n = \begin{vmatrix} A_1 & d_{12} & d_{13} \\ A_2 & d_{22} & d_{23} \\ 0 & d_{32} & d_{33} \end{vmatrix} \qquad (2-23\,a)$$

$$D_n = \begin{vmatrix} d_{11} & d_{12} & d_{13} \\ d_{21} & d_{22} & d_{23} \\ 0 & d_{32} & d_{33} \end{vmatrix} \qquad (2-23\,b)$$

In the previous equations, quantities within the parentheses are the arguments of the Bessel's functions. Upon expansion of the determinants, its can be shown that:

$$b_n = -\frac{J_n(x)F_n - x\,J_n'(x)}{H_n^{(1)}(x)F_n - x\,H_n^{(1)\prime}(x)} \qquad (2-24)$$

where F_n is given by:

$$F_n = F_n(x) = \frac{\rho_1}{\rho}x_T^2 \frac{\begin{vmatrix} d_{22} & d_{23} \\ d_{32} & d_{33} \end{vmatrix}}{\begin{vmatrix} d_{12} & d_{13} \\ d_{32} & d_{33} \end{vmatrix}} \qquad (2-25)$$

In the above equations, $x = k_1 a$ and $x_T = k_s a$. The function F_n is a measure of the modal mechanical admittance, $\dot{u}_r/\tau_{rr}$, of the elastic cylinder. This function contains variables, x_T and x_d ($= k_d a$) which can be related to x through the Lame's constants, thus in effect, F_n is a function of x. For a solid with no damping, F_n is real. Equation (2-24) reduces to Equation (2-5) as the mechanical admittance of the target becomes nil for rigid boundaries.

In the far field where $k_1 r$ is large, the Hankel function of the first kind can be given by its asymptotic form:

$$H_n^{(1)}(k_1 r) = \sqrt{\frac{2}{i\pi k_1 r}}(-1)^n e^{(ik_1 r)} \qquad (2-26)$$

The scattering term in Equation (2-3) can thus be given by:

$$p_{sc}(k_1 r,\theta) = p_0 \sqrt{\frac{2}{i\pi k_1 r}}e^{(ik_1 r)}\sum_{n=0}^{\infty}\varepsilon_n b_n \cos n\theta \qquad (2-27)$$

For subsequent discussions, it is convenient to introduce a modal form function for the

2-6

partial waves, namely:

$$f_n(x,\theta) = \frac{2}{\sqrt{i\pi x}} \varepsilon_n b_n \cos n\theta \qquad (2-28)$$

Equation (2-27) can then be rewritten as:

$$f_\infty(x,\theta) = \frac{p_{sc}}{p_0}\sqrt{\frac{2r}{a}}e^{(-ik_1 r)} = \sum_{n=0}^{\infty} f_n(x,\theta) = \frac{2}{\sqrt{i\pi x}}\sum_{n=0}^{\infty} \varepsilon_n b_n \cos n\theta \qquad (2-29)$$

where $f_\infty(x,\theta)$ is the normalized, far-field form function for the scattering process.

In experimental investigations, the scattered power commands the utmost interest and can be presented by the bistatic or differential scattering crosssection, σ'. It is the square of the modulus of the normalized form function. For the solid cylinder of infinite length, this quantity is given as:

$$\frac{2d\sigma}{a\,d\theta} = \sigma' = |f_\infty(x,\theta)|^2 = \left|\sum_{n=0}^{\infty} f_n(x,\theta)\right|^2 = \left|\frac{2}{\sqrt{i\pi x}}\sum_{n=0}^{\infty} \varepsilon_n b_n \cos n\theta\right|^2 \qquad (2-30)$$

For backscattering at $\theta = \pi$, Equations (2-28) and (2-29) become:

$$f_n(x,\pi) = \frac{2}{\sqrt{i\pi x}}(-1)^n \varepsilon_n b_n \qquad (2-31)$$

$$f_\infty(x,\pi) = \sum_{n=0}^{\infty} f_n(x,\pi) = \frac{2}{\sqrt{i\pi x}}(-1)^n \varepsilon_n b_n \qquad (2-32)$$

and the (normalized) back-scattering cross-section, σ_B, is given by:

$$\frac{\sigma_B}{\pi a} = \left|\sum_{n=0}^{\infty} f_n(x,\pi)\right|^2 = \left|\frac{2}{\sqrt{i\pi x}}\sum_{n=0}^{\infty}(-1)^n \varepsilon_n b_n\right|^2 \qquad (2-33)$$

Similar equations for rigid targets can likewise be derived. Some of these equations for the infinite cylinder are given below with the appropriate superscript, (r), designation. The modal amplitudes b_n have already been given in Equation (2-5). Thus:

$$f_n^{(r)}(x,\theta) = -\frac{2}{\sqrt{i\pi x}}\varepsilon_n \frac{J_n'(x)}{H_n^{(1)'}(x)}\cos n\theta \qquad (2-34)$$

$$f_n^{(r)}(x,\pi) = -\frac{2}{\sqrt{i\pi x}}(-1)^n \varepsilon_n \frac{J_n'(x)}{H_n^{(1)'}(x)} \qquad (2-35)$$

The bistatic scattering and the backscattering crosssections are respectively:

$$\left[\frac{2\,d\sigma}{a\,d\theta}\right]^{(r)} = |f_\infty^{(r)}(x,\theta)|^2 = \left|\frac{2}{\sqrt{i\pi x}}\sum_{n=0}^{\infty}\varepsilon_n\frac{J_n'(x)}{H_n^{(1)\prime}(x)}\cos n\theta\right|^2 \qquad (2-36)$$

$$\left[\frac{\sigma_B}{\pi a}\right]^{(r)} = |f_\infty^{(r)}(x,\pi)|^2 = \left|\frac{2}{\sqrt{i\pi x}}\sum_{n=0}^{\infty}(-1)^n\varepsilon_n\frac{J_n'(x)}{H_n^{(1)\prime}(x)}\right|^2 \qquad (2-37)$$

The clue for the development of the RST was prompted by the realization that the scattering crosssections for the fluid loaded, elastic target, as presented by the magnitude of the far-field form functions, are very similar to those for the rigid target of identical geometry with the exceptions of frequency locations $(k_1 a)$ values very nearly equal to the natural frequencies of the rigid target. The similarity (or dissimilarity) is even more striking when individual partial waves for the two classes of boundaries are compared as shown in Figure 2-2.

(a)   (b)
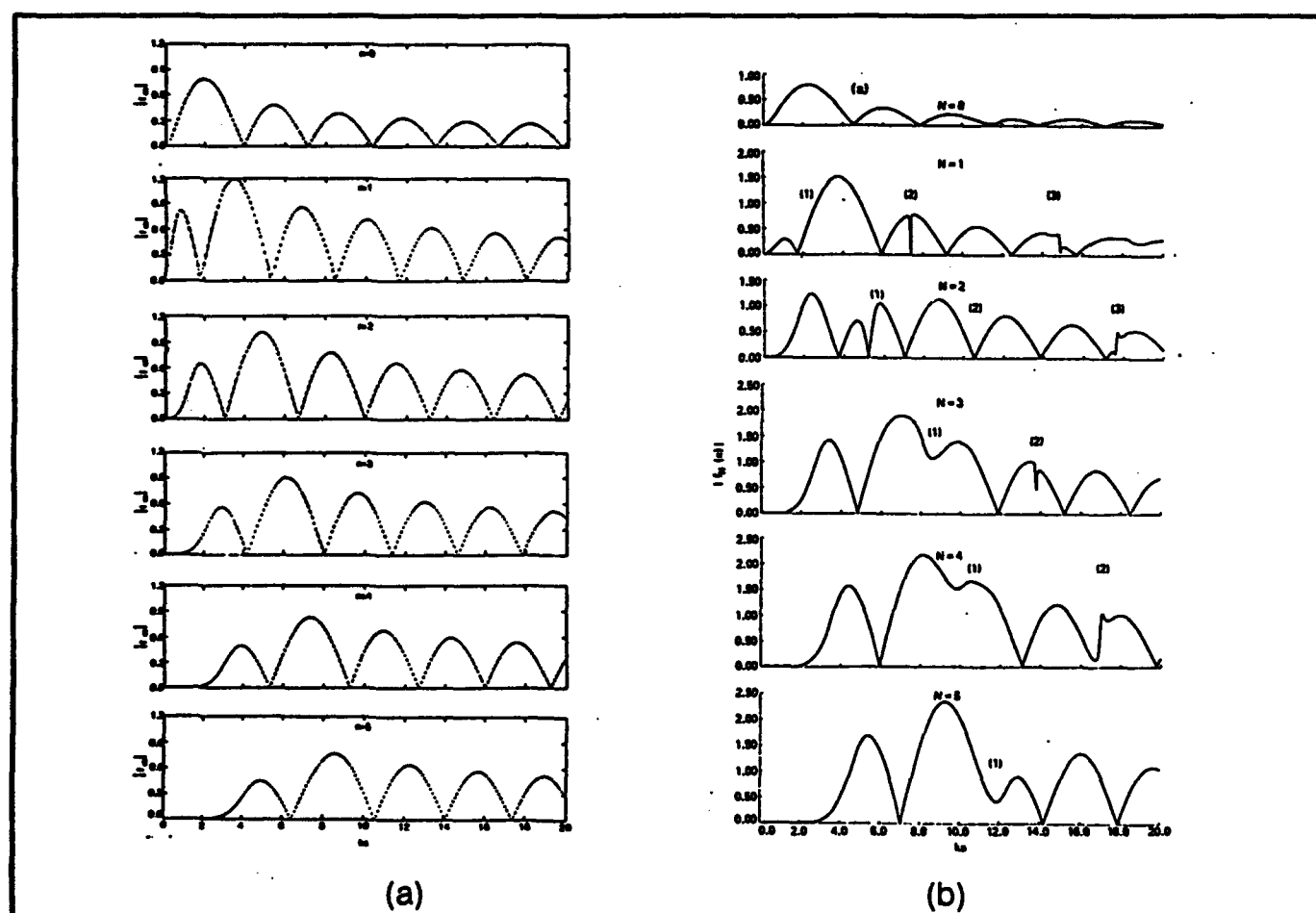
FIGURE 2-2.   BACKSCATTERED SPECTRA WITH AND WITHOUT CONSIDERATION OF RESONANCE[46]

In Figure 2-2(a), amplitudes of several partial waves from $(n = 0 \rightarrow n = 5)$ for a rigid cylinder are plotted. These curves are given by Equation (2-35) and are a set of smooth curves as compared to, in Figure 2-2(b), a similar set of more spiky ones for the elastic cylinder from Equation (2-31). The spikes occur at frequency locations corresponding to the free vibration frequencies. The latter are the real parts of the eigenfrequencies associated with the determinant D_n in Equation (2-23). These locations are marked in Figure 2-2(b), in parentheses, by an additional index l.

Figures 2-3(a) and 2-3(b) depict an overlaid comparison of the two sets of curves taken from the previous figure, for $n = 2$ and $n = 3$, with their respective resonances marked by the same indices. Thus it should be construed that in Figure 2-3(a) for $n = 2$ and for the elastic cylinder, there are resonances (2,1), (2,2), (2,3), etc., which are the solutions of $D_2 = 0$.
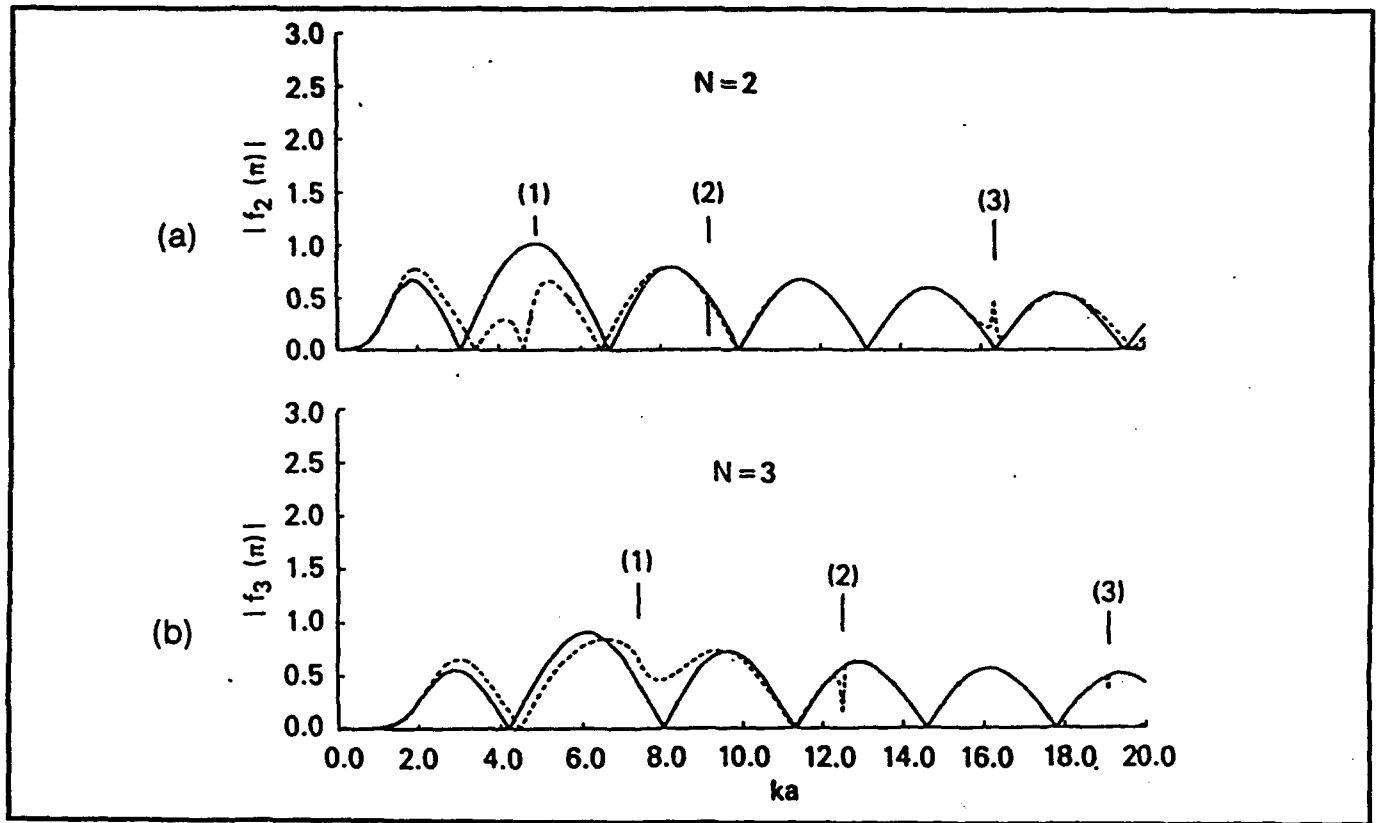
FIGURE 2-3. COMPARISON OF RIGID AND ELASTIC RESPONSES[46]

Figure 2-4 gives a plot of the difference of the two sets of curves in Figure 2-3(a) or $| f_2(\pi, k_1 a) - f_2^{(r)}(\pi, k_1 a) |$, and the contention that the scattered pressure for a fluid loaded, elastic target can be separated into a rigid background and a resonance component (so marked by doubled indices) is borne out in an even dramatic manner. The difference is due to the elasticity or penetrability of the target at resonances and the resulting circumferential waves are referred to as the Rayleigh surface waves for $l = 1$ and as whispering gallery waves for $l > 1$.

Figure 2-5(a) is an overlaid comparison of the far field form function for the two classes (rigid and elastic) of cylindrical targets as a function of the angular orientation. Backscattering occurs at $\theta = \pi$. The form functions presented are approximations containing terms of $n = 0 \rightarrow n = 22$ at $k_l a = 12.53$ which is the resonance location of the (3,2) mode.
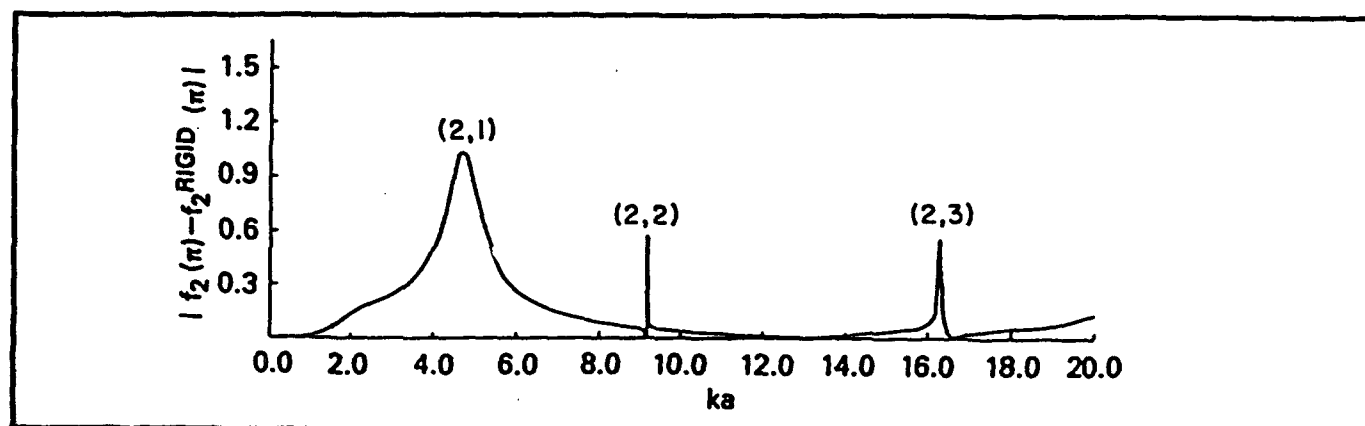
FIGURE 2-4. RESULTS OF SUBTRACTION OF RIGID AND ELASTIC RESPONSES
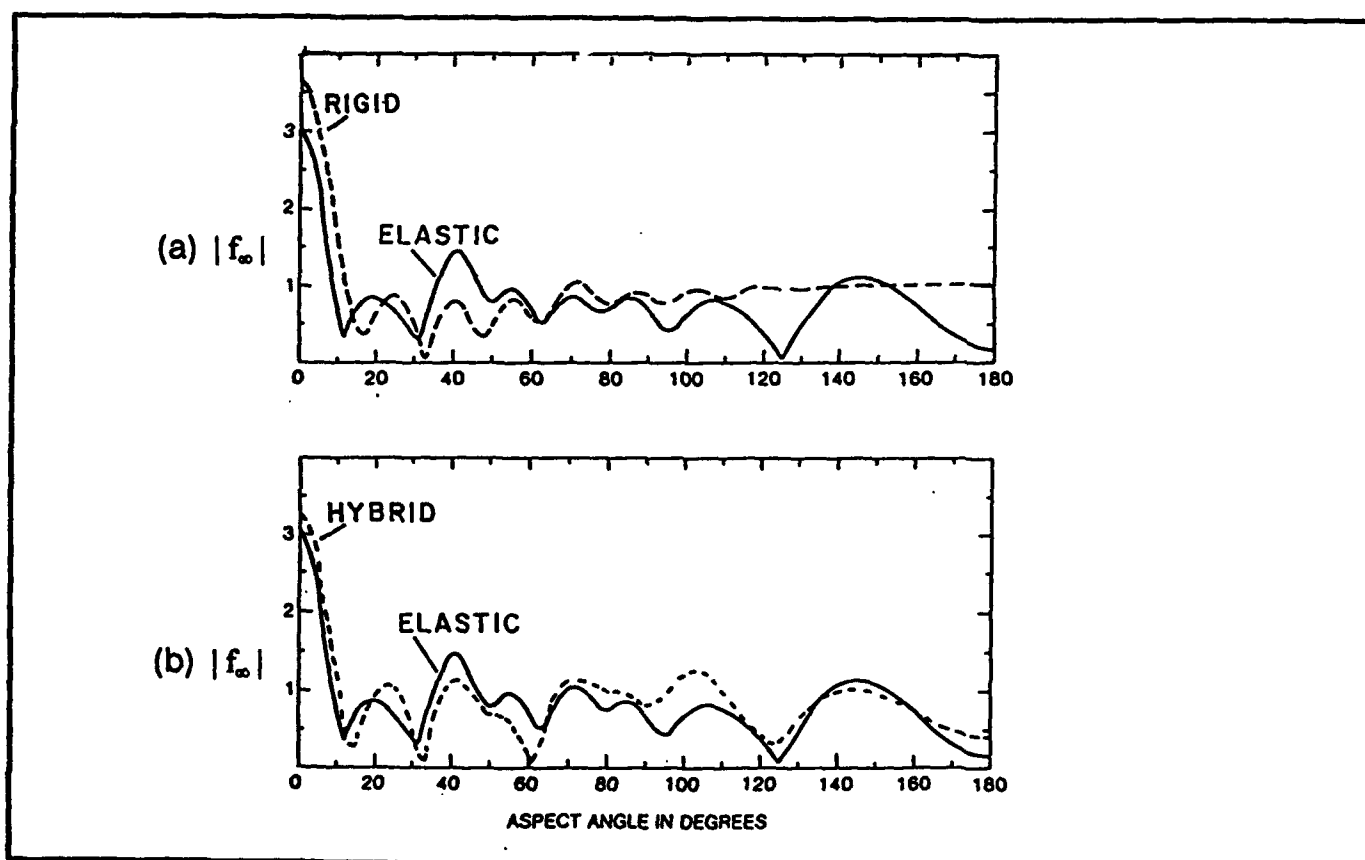
FIGURE 2-5. ASPECT DEPENDENCE OF ELASTIC AND RIGID RESPONSES

A partial expansion of the form function for the elastic cylinder, taken from Equation (2-30) is:

$$|f_\infty(12.53,\theta)| = \left| \sum_{n=0}^{\infty} f_n(12.53,\theta) \right| \sim \left| \sum_{n=0}^{22} f_n(12.53,\theta) \right|$$

$$|f_\infty(12.53,\theta)| = \frac{2}{\sqrt{12.53\pi}} \left| \frac{J_0 F_0 - 12.53\, J_0'}{H_0^{(1)} F_0 - 12.53\, H_0^{(1)'}} + 2\frac{J_1 F_1 - 12.53\, J_1'}{H_1^{(1)} F_1 - 12.53\, H_1^{(1)'}} \cos\theta \right.$$

$$+2\frac{J_2 F_2 - 12.53\, J_2'}{H_2^{(1)} F_2 - 12.53\, H_2^{(1)'}} \cos 2\theta + 2\frac{J_3 F_3 - 12.53\, J_3'}{H_3^{(1)} F_3 - 12.53\, H_3^{(1)'}} \cos 3\theta$$

$$\left. +\cdots+ 2\frac{J_{22} F_{22} - 12.53\, J_{22}'}{H_{22}^{(1)} F_{22} - 12.53\, H_{22}^{(1)'}} \cos 22\theta \right| \qquad (2-38)$$

In the above equation, the Bessel and Hankel functions and their derivatives are computed at the argument of $k_1 a = 12.53$. The functions F_0 through F_{22} are taken from Equation (2-25), which is yet another set of Bessel functions of various orders and their derivatives at $k_1 a = 12.53$. There is a similar series for the rigid cylindrical target which is the same as that given above with the exception that all the admittance functions $F_n = 0$ for $(n = 0 \rightarrow 22)$. We have:

$$|f_\infty^{(r)}(12.53,\theta)| = \left| \sum_{n=0}^{\infty} f_n^{(r)}(12.53,\theta) \right| \sim \left| \sum_{n=0}^{22} f_n^{(r)}(12.53,\theta) \right|$$

$$= \frac{2}{\sqrt{12.53\pi}} \left| \frac{J_0'}{H_0^{(1)'}} + 2\frac{J_1'}{H_1^{(1)'}} \cos\theta + 2\frac{J_2'}{H_2^{(1)'}} \cos 2\theta \right.$$

$$\left. +2\frac{J_3'}{H_3^{(1)'}} \cos 3\theta + \cdots + 2\frac{J_{22}'}{H_{22}^{(1)'}} \cos 22\theta \right| \qquad (2-39)$$

As seen from Figure 2-5(a), there are obvious differences between the two far-field form functions at several angular orientations including the backscattering direction. These differences are due to the elasticity of the target. If the fourth term $(n = 3)$ in Equation (2-39) is replaced by a similar (fourth) term for the elastic case in Equation (2-38), a hybrid equation designated by the superscript (h) in Equation (2-39a), results:

$$\left| f_\infty^{(h)}(12.53,\theta) \right| = \left| \sum_{n=0}^{\infty} f_n^{(h)}(12.53,\theta) \right| \sim \left| \sum_{n=0}^{22} f_n^{(h)}(12.53,\theta) \right|$$

$$= \frac{2}{\sqrt{12.53\pi}} \left| \frac{J_0'}{H_0^{(1)\prime}} + 2\frac{J_1'}{H_1^{(1)\prime}}\cos\theta + 2\frac{J_2'}{H_2^{(1)\prime}}\cos 2\theta \right.$$

$$\left. +2\frac{J_3 F_3 - 12.53 J_3'}{H_3^{(1)} F_3 - 12.53 H_3^{(1)\prime}}\cos 3\theta + \cdots + 2\frac{J_{22}'}{H_{22}^{(1)\prime}}\cos 22\theta \right| \qquad (2-39a)$$

When this hybrid equation is compared to that of the rigid case in Equation (2-39) as shown in Figure 2-5(b), the differences seen in Figure 2-5(a) more or less disappear. Consideration of the result in Figure 2-5 and that in Figure 2-3 presented previously strongly leads to the following points:

1. It seems, from looking at Figures 2-5(a) and 2-5(b), that the differences, at resonance, between the scattered pressure for the rigid and for the elastic cases are primarily due to the existence of a single elastic term, $f_3(12.53,\theta)$, pertinent to the (3,2) resonance and the (3,2) resonance alone. This implies that the other resonances are not at all excited at $k_1 a = 12.53$.

2. It also implies that, term for term, the elastic partial wave must virtually be equal to that for the rigid case because of the close resemblance of the elastic and the hybrid curves in Figure 2-5(b). The exception is the $f_3(12.53,\theta)$ term mentioned above.

3. In Figure 2-3, the differences of the partial waves for the two cases were shown for the backscattering direction, and these differences are reflected in the (3,2) resonance bistatic form function at $\theta = \pi$ in Figure 2-5(a), together with the differences at other angular orientations. The fact that a single elastic resonance term $f_3(12.53,\theta)$ accounts for the differences not only for $\theta = \pi$ but for all other angular orientations, see Figure 2-5(b), strongly suggests that differences in partial waves are not limited to the backscattering direction but extend to all angular orientations.

From the above discussion, it can be said with reasonable conviction that the scattered pressure from an elastic target consists of a rigid background due to specular reflection and diffraction effects and, additionally, a resonance component. The latter is due to the elasticity or penetrability of the target which, by virtue of admitting energy, gives rise to the many modes of free vibration within the target. This energy admission occurs only at, and very near one of the modal resonances of the target. There is no energy admission/penetration at other frequencies, and, in such situations, the scattered pressure can be derived as if the target is perfectly rigid. This is the qualitative statement of the RST.

The quantitative statement of the RST involves the explicit subtraction of the rigid background from the elastic form function. Defining an elastic scattering function $S_n(x)$ such that:

$$S_n(x) - 1 = 2b_n = -2\frac{J_n(x)F_n - x J_n'(x)}{H_n^{(1)}(x)F_n - x H_n^{(1)'}(x)} \qquad (2-40)$$

and further defining an elastic scattering phase shift $\eta_n(x)$ such that:

$$\tan\eta_n(x) = \frac{J_n(x)F_n - x J_n'(x)}{N_n(x)F_n - x N_n'(x)} \qquad (2-41)$$

where $N_n(x)$ is the Bessel function of the second kind and relates to the Hankel function by $H_n^{(1)}(x) = J_n(x) + i N_n(x)$. The conjugate of $H_n^{(1)}$ is $H_n^{(2)}(x) = J_n(x) - i N_n(x)$.

It can be shown by taking the reciprocal of $b_n(x)$ from Equation (2-24) and simplifying that:

$$b_n = i \sin\eta_n e^{(i\eta_n)} \qquad (2-42)$$

and by substituting $b_n(x)$ back into Equation (2-40), we have:

$$S_n = 1 + 2b_n = 1 + 2 i \sin\eta_n e^{(i\eta_n)} = e^{(i2\eta_n)} \qquad (2-43)$$

A set of equations similarly exists for the rigid case:

$$S_n^{(r)}(x) - 1 = 2b_n^{(r)} = -2\frac{J_n'(x)}{H_n^{(1)'}}(x) \qquad (2-44)$$

$$\tan\eta_n^{(r)}(x) = \frac{J_n'(x)}{N_n'(x)} \qquad (2-45)$$

$$b_n^{(r)} = i \sin\eta_n^{(r)} e^{(i\eta_n^{(r)})} \qquad (2-46)$$

$$S_n^{(r)} = 1 + 2 i \sin\eta_n^{(r)} e^{(i\eta_n^{(r)})} = e^{(i2\eta_n^{(r)})} \qquad (2-47)$$

Also from Equation (2-44),

$$S_n^{(r)}(x) = 1 - 2\frac{J_n'(x)}{H_n^{(1)'}(x)} = -\frac{J_n'(x) - i N_n'(x)}{H_n^{(1)'}(x)} = -\frac{H_n^{(2)'}(x)}{H_n^{(1)'}(x)} \qquad (2-48)$$

We now want to split the elastic scattering function, $S_n(x)$ into a rigid portion and a resonance portion:

$$S_n(x) = 1 - 2\frac{J_n(x)F_n(x) - x J_n'(x)}{H_n^{(1)}(x)F_{n(#f)x} - x H_n^{(1)'}(x)}$$

$$S_n(x) = -\frac{H_n^{(2)}(x)F_n(x) - x H_n^{(2)'}(x)}{H_n^{(1)}(x)F_n(x) - x H_n^{(1)'}(x)} = -\left[\frac{H_n^{(2)'}(x)}{H_n^{(1)'}(x)}\right]\left[\frac{F_n^{-1}(x) - \frac{H_n^{(2)}(x)}{x H_n^{(2)'}(x)}}{F_n^{-1}(x) - \frac{H_n^{(1)}(x)}{x H_n^{(1)'}(x)}}\right] \qquad (2-49)$$

It should now be recalled that $F_n(x)$ is a measure of the admittance of the target, hence its reciprocal can be viewed as the modal mechanical impedance of the target. The conjugate terms $H_n^{(i)}/x H_n^{(i)}$, $(i = 1, 2)$ can be viewed as the modal acoustical impedance of the fluid given by:

$$\frac{H_n^{(1)}(x)}{x H_n^{(1)'}(x)} = \Delta_n(x) + i K_n(x);$$

$$\frac{H_n^{(2)}(x)}{x H_n^{(2)'}(x)} = \Delta_n(x) - i K_n(x) \qquad (2-50)$$

where:

$$\Delta_n(x) = \frac{1}{x}\frac{J_n(x)J_n'(x) + N_n(x)N_n'(x)}{[J_n'(x)]^2 + [N_n'(x)]^2} \qquad (2-51)$$

$$K_n(x) = -\frac{2}{\pi x^2}\frac{1}{[J_n'(x)]^2 + [N_n'(x)]^2} \qquad (2-52)$$

The quantity $K_n(x)$ in Equation (2-52) is negative.

Let a resonance frequency, x_{nl}, be defined such that:

$$F_n^{-1}(x_{nl}) = \Re\left[\frac{H_n^{(i)}(x_{nl})}{x H_n^{(i)'}(x_{nl})}\right] = \Delta_n(x_{nl}) \qquad (2-53)$$

The above characteristic equation is equivalent to the statement attributed to Junger and Feit[55] that resonances should appear when the sum of the mechanical and the radiation

impedances goes to zero. In Equation (2-53), the resonance frequency is designated by indices n and l with the index n pertinent to each of the partial waves. The additional index l indicates the multiplicity of the solution, namely, for each partial wave, there exist the fundamental resonance $(n, 1)$ and harmonics (n, l), theoretically infinite in number. Their frequencies are very nearly equal, but not identical, to the (complex) eigenfrequencies obtained from the Equation $D_n(x) = 0$.

We now adopt the linear-approximation method of the nuclear resonance theory[56] by expanding the impedance term in the vicinity of one of the resonance frequencies, x_{nl}, in a Taylor series:

$$F_n^{-1}(x) - F_n^{-1}(x_{nl}) = F_n^{-1}(x) - A_n(x_{nl}) - \beta_{nl}(x - x_{nl}) \qquad (2-54)$$

By substituting the results in Equations (2-48), (2-54), and (2-50) into Equation (2-49) to obtain:

$$S_n(x) \sim S_n^{(t)}(x) \frac{x - x_{nl} - \frac{1}{2}i\Gamma_{nl}}{x - x_{nl} + \frac{1}{2}i\Gamma_{nl}} \qquad (2-55)$$

The quantities β_{nl} and Γ_{nl} are undefined constants and are related by:

$$\Gamma_{nl} = -\frac{2K_{nl}}{\beta_{nl}} \qquad (2-56)$$

The quantity Γ_{nl} in Equation (2-56) is positive and can be viewed as the width of the (n, l) resonance. Thus:

$$S_n(x) - 1 = S_n^{(t)}(x) \frac{x - x_{nl} - \frac{1}{2}i\Gamma_{nl}}{x - x_{nl} + \frac{1}{2}i\Gamma_{nl}} - 1$$

$$= S_n^{(t)}(x) \left[1 - \frac{i\Gamma_{nl}}{x - x_{nl} + \frac{1}{2}i\Gamma_{nl}} \right] - 1$$

$$= [S_n^{(t)}(x) - 1] - S_n^{(t)}(x) \frac{i\Gamma_{nl}}{x - x_{nl} + \frac{1}{2}i\Gamma_{nl}} \qquad (2-57)$$

and by means of Equation (2-47),

$$S_n(x) - 1 = 2i \sin \eta_n^{(r)} e^{\left(i\eta_n^{(r)}\right)} - e^{\left(i2\eta_n^{(r)}\right)} \frac{i\Gamma_{nl}}{x - x_{nl} + \frac{1}{2}i\Gamma_{nl}}$$

$$= 2 i e^{\left(i2\eta_n^{(r)}\right)} \left[\sin \eta_n^{(r)} e^{\left(-i\eta_n^{(r)}\right)} + \sum_{l=1}^{\infty} \frac{\frac{1}{2}\Gamma_{nl}}{x_{nl} - x - \frac{1}{2}i\Gamma_{nl}} \right] \qquad (2-58)$$

The summation over $l = 1 \to \infty$ is added in the last expression due to the multiplicity in the solution of Equation (2-53) as explained previously. This summation generally does not refer to the summing of infinite terms but rather it denotes the activation, one term at a time, as one of the resonances x_{nl} is approaching.

The substitution into Equation (2-28) yields the final form:

$$f_n(x,\theta) = \frac{2}{\sqrt{i\pi x}} \varepsilon_n b_n \cos n\theta = \frac{1}{\sqrt{i\pi x}} \varepsilon_n [S_n(x) - 1] \cos n\theta$$

$$= \frac{1}{\sqrt{i\pi x}} \varepsilon_n 2 i e^{\left(i2\eta_n^{(r)}\right)} \left[\sin \eta_n^{(r)} e^{\left(-i\eta_n^{(r)}\right)} + \sum_{l=1}^{\infty} \frac{\frac{1}{2}\Gamma_{nl}}{x_{nl} - x - \frac{1}{2}i\Gamma_{nl}} \right] \cos n\theta \qquad (2-59)$$

This equation explicitly shows that the form function, and the scattered pressure thereof, given by Equation (2-30), consists of a rigid background and a resonance portion which comes into effect as the resonances of the partial waves approach. It constitutes the quantitative statement of the RST.

The mathematical treatment for other cases is similar to that for the infinite, solid cylinder. For a hollow shell, two unknown constants associated with the Hankel function are to be included in Equations (2-14) and (2-15). An equation similar to Equation (2-14) to describe the pressure field in the enclosed fluid exists with an extra, unknown constant. This brings the unknown constants to a total of six and results in 6 by 6 determinants in $B_n(x)$ and $D_n(x)$ in Equation (2-22). An additional layer of shell will increase the order of the matrices by 4 to 10. For spherical cases, the elements of the matrices will have become spherical Bessel functions and the angular variable of the scattering is dictated by the Legendre polynomials with $(\cos\theta)$ as their argument.

CHAPTER 3

EXPERIMENTAL FACILITY AND ARRANGEMENT

The experimentation to verify the validity of the RST and to develop the methodology for underwater target classification by means of active sonar was conducted in the Naval Surface Warfare Center Coastal System Station (NSWCCSS) Hydroacoustic Measurements Facility at White Oak, Maryland. The facility is one of the two major testing facilities[57,58] operated and managed by the Mine Systems Branch (Code 2620) of the Mine Systems Division (Code 260) which is a division of the Costal Warfare Systems Department (Code 20).

The White Oak facility, located in Building 217, is equipped with a redwood test tank 30' in diameter and 20' in depth. This tank is placed underground within a 36' diameter, steel, earth-retaining drum which sits on a resilient support on a 2' reinforced concrete foundation. Solid earth around the drum and the concrete foundation effectively isolate the tank on all sides except the top side from building, roadway and other operating equipment vibration and noise. The arrangement also provides for electrical shielding. Built over the tank is the entire church-like building which is constructed with laminated beams with a very high-peaked roof to facilitate a precision hoisting or lifting carriage. The main floor or the test bay, which is 4' above the top of the tank, is made of 12", post-stressed, reinforced concrete with a 52" wide by 46' slot running over the diameter of the tank. Heavy covers over the slot are provided to seal off the tank from the outside resulting in an isothermal testing environment and further mitigating airborne noise intrusion. The tank is filled with continuously filtered fresh water. The filtering process not only minimizes unwanted scattering from floating or suspending particles but also affords a refraction-free test environment by eliminating temperature gradients in the water. The parking lot is at the same level as the test bay, and equipment weighing as much as 8,000 pounds can be placed on the floor and moved around using a folk lift. A transducer supporting and positioning structure is isolated mechanically from the building and the tank. It consists of a system of interconnecting vertical columns resting on long, horizontal "grade" beams underground. On the top of the structure are 65' long horizontal guide-rails (crane rail beams) which support and guide a lifting carriage with a two-ton capacity. This lifting carriage is capable of handling all moving requirements with speed and precision including horizontal movements along the tank diameter and vertical lifting and positioning of loads or transducers. A cross section of the building and the tanks is given in Figure 3-1.

At the test bay level are two "I" beams similar to the crane rail beams which are also supported independently and acoustically isolated from the vertical columns and the floor. These beams support the slot covers and two additional transducer supporting and positioning

platforms which can be moved by sliding along the slot on circular guides or by lifting and lowering to position by the lifting carriage. A standard transducer platform has fixtures which can place a transducer or projector to any depth within the tank. Precise positioning along the slot is accomplished by a motorized drive. The other platform which has a single axle that rotates above the tank and parallel to the water surface. Attached to the end of the axle is a horizontal positioner for the suspension of hydrophones or loads at a desired test level in water. The arrangement is suitable for rotating a target in a horizontal plane about a designated axis as is used to determine the directivity patterns of nonsymmetrical line hydrophones. The rotating axis is made of a hollow tube which also allows a target to be suspended axially, but at a desired angle, θ, with respect to the incoming wave, while a hydrophone riding on the positioner rotates around the target at a distance, R, from the target as depicted in Figure 2-1. Both platforms slide on two round tracks, each 46' long, which are level and at a constant separation for precise alignment.
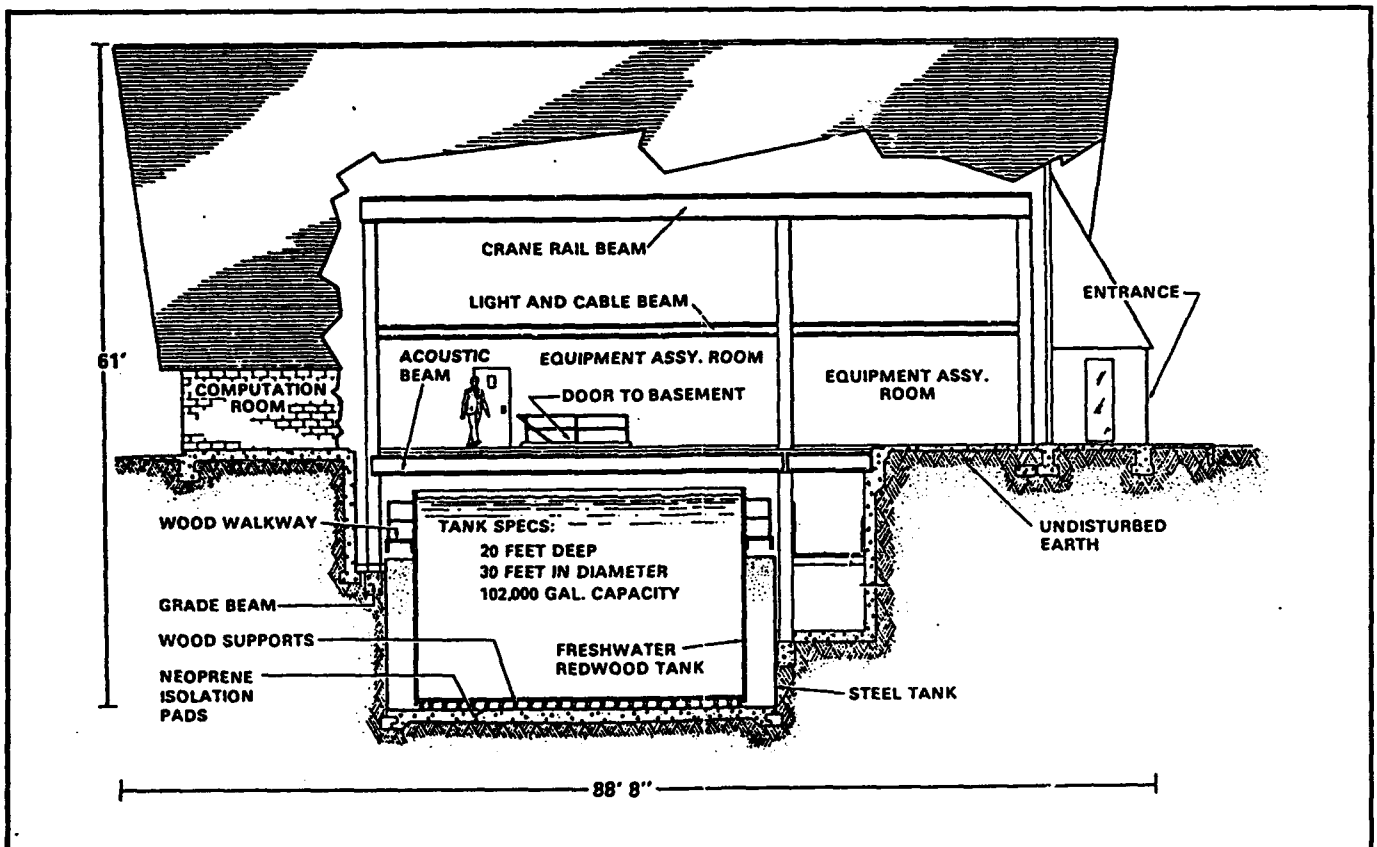
FIGURE 3-1. WHITE OAK SITE OF HYDROACOUSTIC MEASUREMENTS FACILITY

The heart of the signal generation, conditioning, and recording rests within an electronic console which is housed in a separate air-conditioned room on the main floor. The unit has a transmitting section which supplies power to the projector and a corresponding receiving section which accepts and modifies transduced signal from the hydrophone. Both sections are controlled by a pulse time generator which sets the transmitting pulse width, the receiving pulse width and its time delay with respect to the transmitted pulse. Operational frequency varies

continuously from 50 Hz to 2 MHz with a 50-dB dynamic range. The synthesizer generates CW signal adjustable from 1 to 99 seconds over a pre-determined frequency range in linear or logarithmic scale. The CW signal is broken up by the opening and closing actions of the transmitter signal gate into pulses which eventually are emitted through the projector as a train of pressure pulses in water. The (transmitted) pulse width, T_t, and the rapidity of the actions or repetition rate are set by the pulse timing generator. These pressure pulses are sampled by the hydrophone at a time delay, T_d, with respect to the opening of the transmitter signal gate and at a sampling (received) pulse width T_r. Both quantities are also set by the pulse timing generator. For each pulse, no signal will be detected by a transducer beyond (T_d+T_r). Recording instruments within the electronic console include a rectangular recorder with a linear or logarithmic paper drive and a polar recorder which are pegged automatically to the various functions and controls of the synthesizer, the pulse timing generator and the rotating mechanism. Analog signal at various points in the console is monitored by dual-beam storage oscilloscopes with delay circuitry. Pictures of the pulse at various stages of resonance can be recorded in photographs. A block diagram of the major components of the electronic console is given in Figure 3-2.

RST experiments have been done exclusively in the White Oak Site in the large tank. The other major testing facility at Brighton Dam, about 14 miles north of White Oak, Maryland, offers a comparable facility in a barge on an 800-acre reservoir. Average test depth is 25'. Future experiments, especially on CW mode, can be performed in the Brighton Site.

In summary, the electronic console, the moving carriage and the two platforms allow for a variety of projector-target-hydrophone (P-T-H) orientations and many types of experimentation for the RST investigation. Some of the notable possibilities are given as follows.

Frequency response over a predetermined frequency range in linear or log scale is very easily obtained. Figure 3-3 depicts the data from this type of tests.

For this experiment, the hydrophone is typically positioned between a projector and its target in a line, and in the middle of the tank at mid-depth. Depending on the time delay, the recorded signal can be the direct pulse which insonifies the target, as shown in the top trace, the backscattering or the monostatic cross section of the target as the middle trace, or at a further time delay, the reradiated of the target with the background suppressed as the bottom curve. The latter two curves are expected to yield the various modal resonances as speculated upon in the introductory section.

The previous description of the data collection system reflects what was used to collect the data in this report. It has since been upgraded to a computer controlled data collection system.
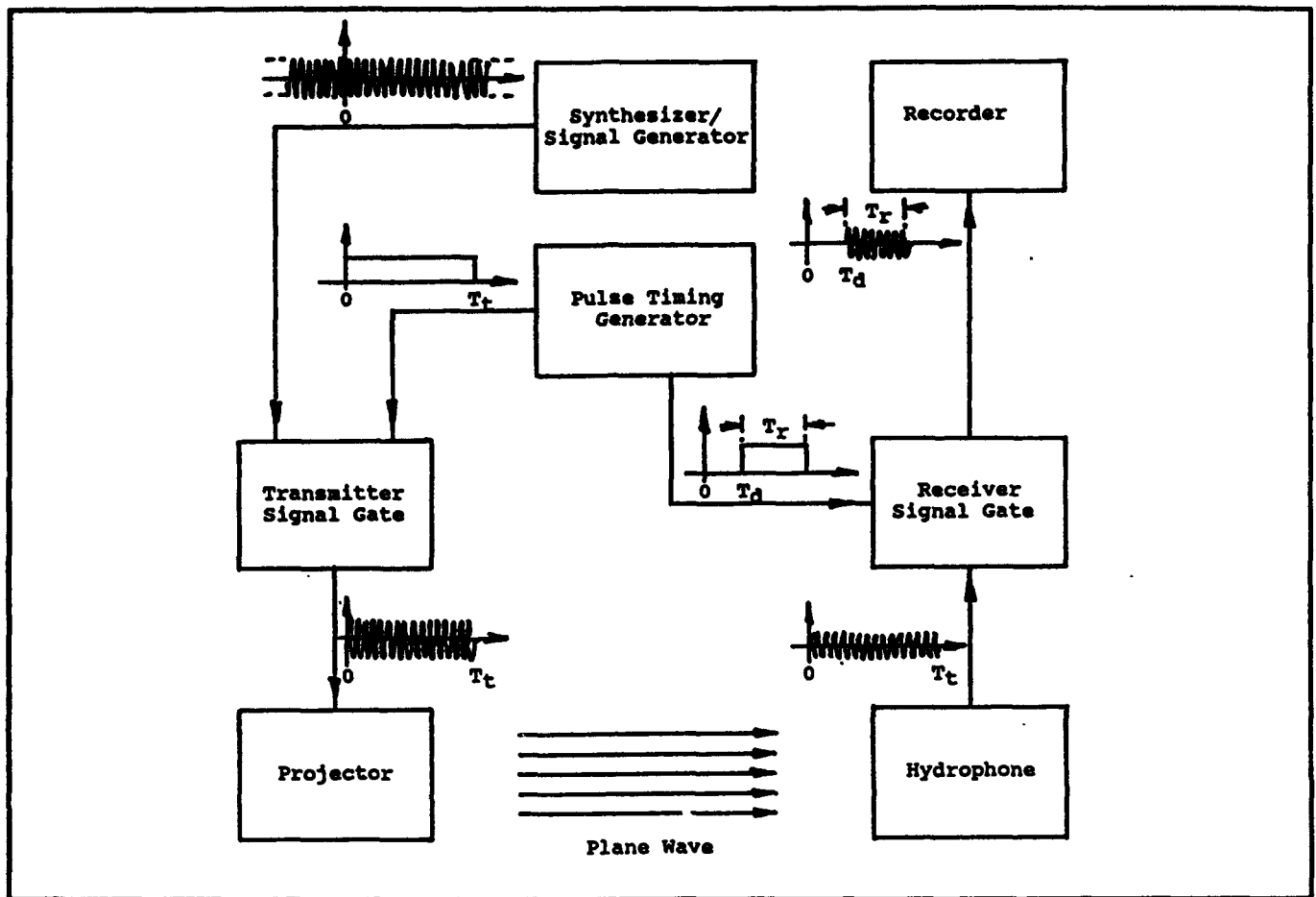
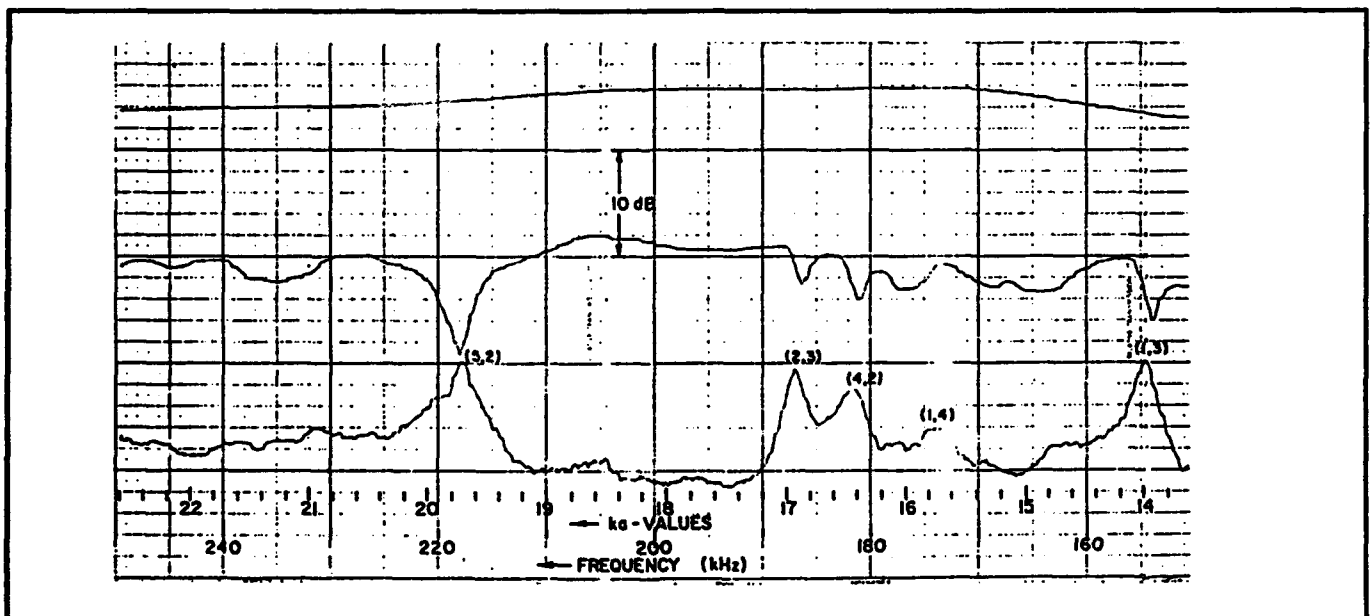FIGURE 3-2. BLOCK DIAGRAM OF MEASUREMENT SYSTEM

FIGURE 3-3. SPECTROGRAM DATA

Monostatic broadside spectrograms can be measured using the test geometries shown in Figure 3-4.
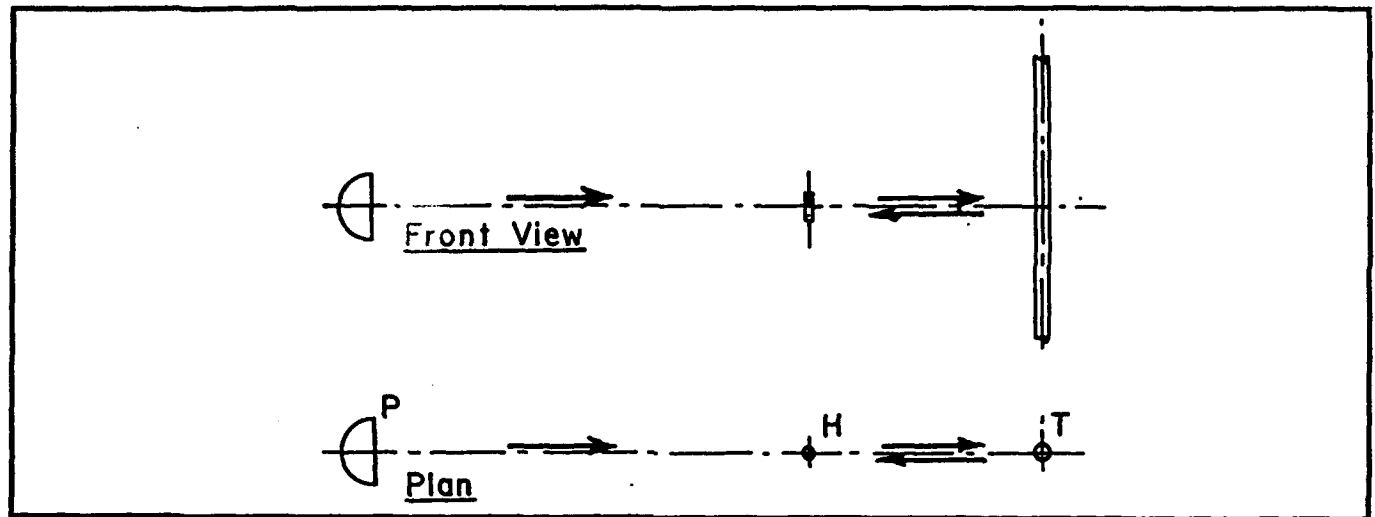
FIGURE 3-4. MONOSTATIC TEST CONDITION FOR SPECTROGRAMS

If the frequency is slowly varied by taking smaller frequency steps over less of a span a "Zoom" effect can be achieved and refined features near and at a modal resonance such as the bandwidth of the resonance peak, and its shape (the rapidity or slope at which a resonance is arrived or receded) can be obtained.

Bistatic frequency response can be obtained with a P-T-H arrangement shown in Figure 3-5 The target can either be in a vertical or a horizontal orientation. When the target is in the vertical orientation, the insonification on the target remains normal, while oblique incidence on the target will result when the target is in a horizontal orientation.

The aspect dependence of the bistatic scattering cross section can be obtained with the target suspended freely at the axis of the rotator and the hydrophone attached to the rotating positioner. The resulting directivity pattern can be at any frequency including resonance frequencies. The geometry for this test is shown In Figure 3-6.
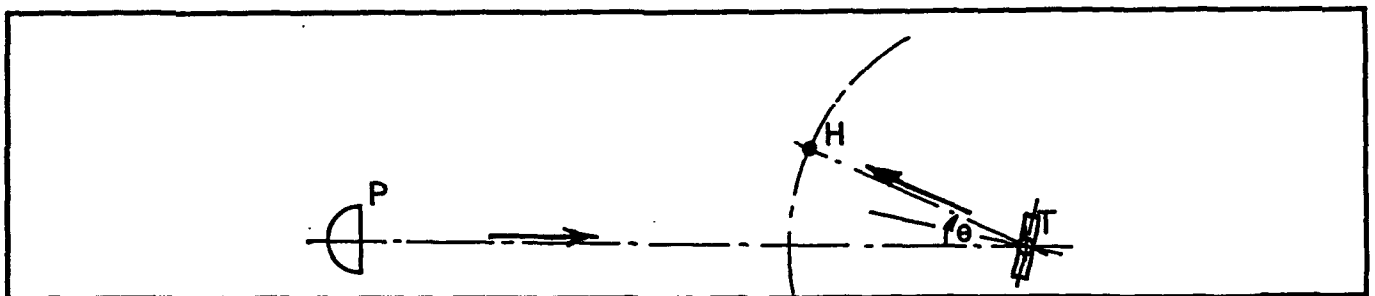
FIGURE 3-5. BISTATIC TEST CONDITION FOR SPECTROGRAMS
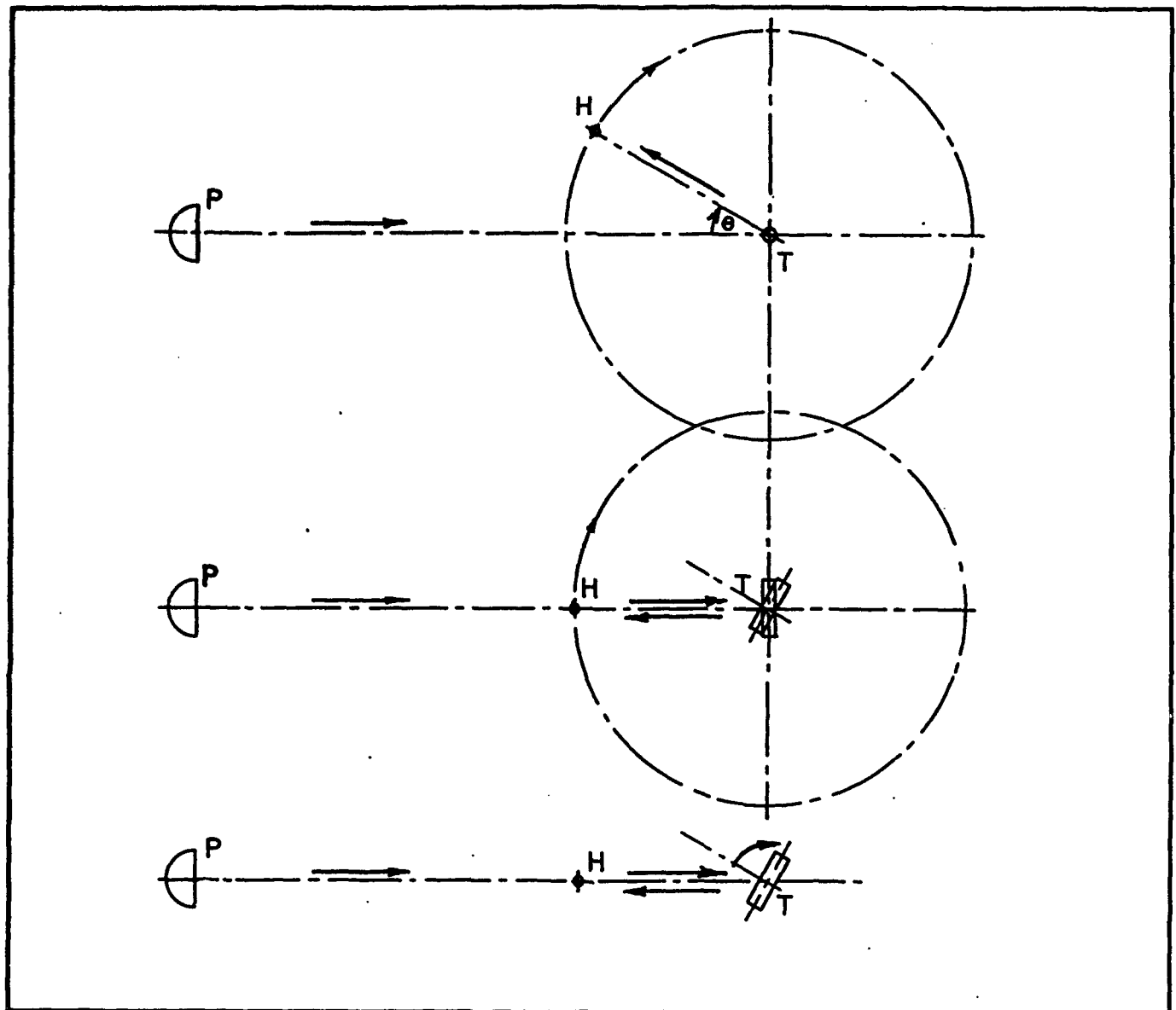
FIGURE 3-6. TEST CONDITIONS FOR ASPECT DEPENDENCE MEASUREMENTS

As shown the target can be either in the vertical or horizontal orientation. The hydrophone or the target can be rotated while the other is held stationary at any arbitrary angle or both can be rotated in synchronous fashion.

One of the most important features of any acoustic measurements system is the ability to time gate the hydrophone signal to measure the desired signal and to reject unwanted noise. In a closed environment, one source of noise is the unwanted reflections. The best way to set these delay times and to find unexpected echos is to display the pulses on an oscilloscope. It is possible, with the proper settings, to view the direct, reflected and the re-radiated pulses either individually or all at one time. Slow frequency sweeps can then be made to insure that the test geometries and delay selections are correct. Then the measurements become routine.

Figure 3-3 has three data curves on it which were collected by setting the receive gate at three different delay times referenced to the transmission of the pulse. The upper curve is the direct pulse which provides a means of determining the intensity of the signal reaching the target or being transmitted from the projector. It was collected by setting the receive gate at the delay time (plus a little extra) that it takes the signal to go from the projector to the hydrophone. The middle curve is a measure of the intensity of the signal reflected from the target and is dependent on the differential scattering cross-section pattern, as described by Equation (2-30). For this measurement the receive gate must be set toward the end of the reflected pulse. The bottom curve is a measurement of the intensity of the re-radiated energy. For this measurement the receive gate must be set toward the beginning of the re-radiated pulse. This is easy to see in Figure 3-7.
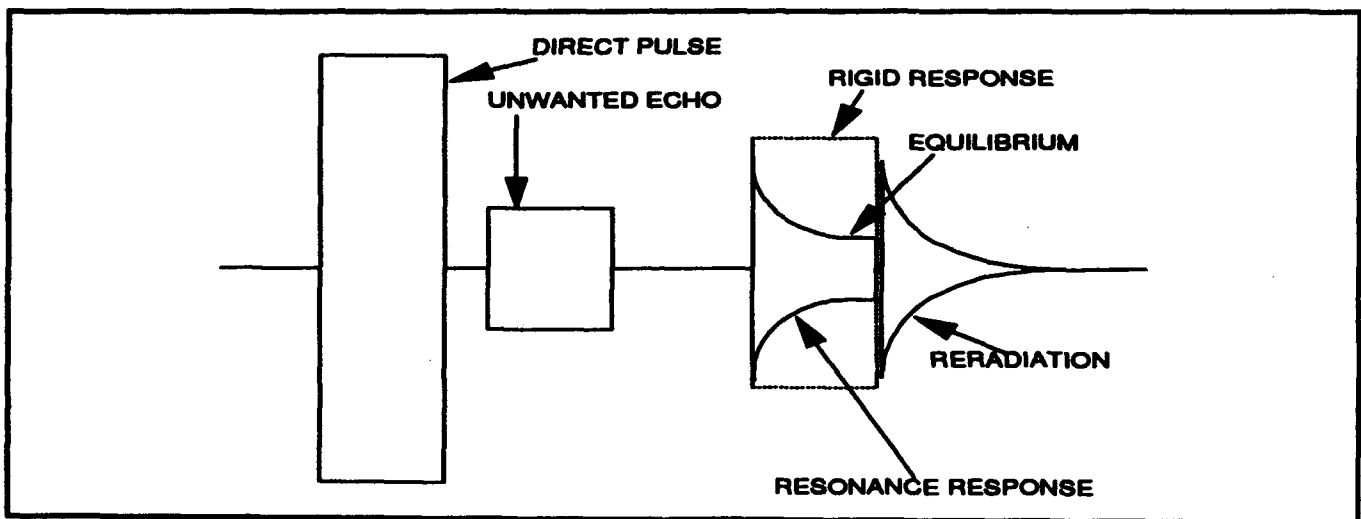
FIGURE 3-7. DEPICTION OF THE TIME DOMAIN SIGNAL

In the real world the transmitted pulses are not square since it takes a cycle or so for the transducer to attain equilibrium. There is a corresponding number of cycles at the end before the transducer comes to rest. This means that there should always be a cycle or two between the leading edge or the trailing edge of the pulse and the sampling gate in order to eliminate these unstable portions.

The arrangements discussed up to this point pertain more or less to an infinite cylinder suspended freely in the water. Of course the cylinders we measured had finite length but since the tests were conducted using signals in the hundreds of kilohertz region our projectors had finite beam width and as long as only a portion of the cylinder was insonified, it reacts like an infinite cylinder. Rotation of the cylinder by itself creates no new situation due to the symmetry of the target, in the vertical orientation, and the impingement was always normal to the target. The same applies for a target which is spherical. However, the situation changes for other targets whose surface is not symmetrical to the (vertical) axis of suspension. An example is a finite cylinder suspended with its axis in a horizontal orientation. Another example is a horizontally oriented spheroid with its circular cross section axis perpendicular to the free

surface. With the present test facility, the rotation of the target itself and the independent rotating of the hydrophone on the horizontal positioner create many additional testing possibilities.

CHAPTER 4

RST DEPLOYMENT METHODOLOGY

Before a methodology for the detection and classification of underwater targets can be finalized for deployment at sea, it is necessary to develop, within the context of the available facility and its capability, experiments which will verify the predictions of classic resonance theory. As mentioned in the introductory section, successful validation would automatically provide the sought-for methodology for the active classification of underwater targets. At the least, the experience and expertise gained by the venture will be invaluable assets for future methodology development and improvement.

In the planning of the experiments, the prevention of wave interference commanded the most attention. This consideration led to the use of the pulse mode for the experimentation; and, in turn, to the many decisions pertaining to the physical arrangements of the testing instruments, their sizes, and to the ways and timing the signals were sampled, etc. These considerations are discussed in the following paragraphs.

One of the first considerations to address was the placement of the projector, target, and the hydrophone. Recalling Figure 3-5 and the associated discussion the bulk of the consideration was to eliminate the unwanted reflections. The target should preferably be placed in the central region of the tank which is approximately 15' from the tank walls and at a mid-depth of 10' from the free surface. The projector radiates in a rather narrow beamwidth, which is inversely proportional to the driving frequency. It should be placed far from the target to assure that the rays impinging on the target are reasonably parallel and even in intensity to simulate a plane wave. The hydrophone which samples the reflection should also be placed reasonably far from the target to achieve as good a far-field condition as possible. A good compromise led to the placement of the target at the center of the tank with the projector 10' from it. The hydrophone was placed 3.5' from the target. This P-T-H arrangement was used for the majority of the experiments.

The next consideration was the selection of the size of the target, hydrophone and projector. The choice of the target size is contingent upon two major factors. First, it must be small compared to the physical arrangement described in the last paragraph to satisfy (a) the plane wave incidence condition which allows an even insonification on the target, and (b) the far field condition with respect to the hydrophone sampling for scattering or re-radiation. Secondly, the size must be small in comparison with the wavelength over the frequency (ka) range of the theoretical predictions. For most of the experiments, cylindrical rods from 0.75" to 1.87" in diameter and 6" or longer in length were used. Those diameters yielded ka values

ranging from 4 (0.75" rod at 100 kHz) to 50 (1.87" rod at 50 kHz). A length of 6" was long enough to minimize end effects and preserve the two-dimensional scattering condition of an infinite cylinder.

In addition to the cylindrical rods, other targets were chosen for experimentation, including, hollow cylindrical shells of various sizes (0.75" to 6.0") with ID/OD ratio of 2/3 and ID/OD ratio very nearly equal to 1.0 (very thin-walled cylindrical shells); an ellipsoid 3.5" by 0.7" measured in the major and the minor axes; a brass, hollow spheroid approximately 3.5" by 7" in outer size; and a 4.5" diameter, steel pressure tank. The hollow cylindrical shells of aspect ratio of 2/3 was used to verify previous RST predictions and other targets were included to add variety to the experimentation. These models represented a first step toward more practical targets. A photograph of several of the targets is given in Figure 4-1. The targets were made of aluminum unless otherwise stated. The material had not been mentioned prominently because it played very little role in the experimental verification of the theoretical prediction since the original RST formulation was developed using a ratio wave number in the material to the wave number of the medium.

In the choice of a hydrophone for the experiments, size was again an important consideration. A Celesco LC-10 hyurophone was selected mainly because its diameter of 0.250" offered very little blockage of the incident wave to the target when placed in the back-scattered position. The loss of transducer sensitivity in the choice of a small transducer was partially compensated for the gain in the applicable frequency range. It is also advisable to operate below the resonance frequency of the hydrophone, which for the LC-10 is 225 kHz.

Size was a less critical factor in the choice of a projector. A USRD E-27 transducer having an effective diameter of 0.4" was chosen because its operating range extended from 50 to 700 kHz.

The third consideration was the transmitting and receiving gate or pulse, width. As discussed in the experimental testing facility section and graphically illustrated in Figure 3-2, a transmitted pulse starts when the transmitter signal gate of the pulse timing generator is activated (goes to a logical "1" and ends when the same gate is deactivated (goes to "0"). The time lapse, T_t, is the transmitted pulse width. Similarly, after a chosen time delay with respect to the activation of the transmitted signal gate, T_d, the received signal gate is activated and deactivated over a time interval, T_r, during which a portion of the transmitted or reflected signal as received by the hydrophone is sampled. This sequence of actions is repeated many times per second and is referred to as the pulse repetition rate. Thus a train of pulses can be identified for each transmitted pulse, and the time between these pulses is the difference in time of flight. The difference in flight path is given by the product of the difference in flight time and the speed of propagation. The position of the transducers and the target must be optimized to provide minimal interference at the time and position of the measurements.

FIGURE 4-1. TEST TARGETS

This type test requires large source levels and thus a very large driving voltage. Since the electronics gating circuit does not switch this signal to zero volt, there can still be a signal being produced by the projector and received at the hydrophone that can have similar amplitude to the signal being measured. This residual, plus the fact that the projector is in vigorous motion when the pulse goes to "0" causes a exponentially decaying tail on the training edge of the pulses. Sometimes these tails cannot be avoided and also add to the sampled signal. Figure 4-2 is a depiction of the pulse as it appears in the water. In later figures the delay time to the leading edge of the pulse, in microseconds, is placed on the pulse depiction where the "XXXX" is in this figure.
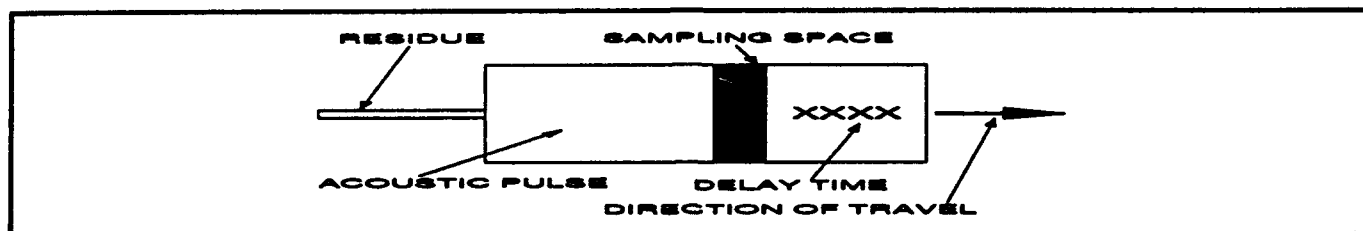
FIGURE 4-2. DEPICTION OF ACOUSTIC PULSE

In Figure 4-3, the locations of the tank walls, back (BW) and front (FW), and the projector (P), hydrophone (H), target (T), and traveling pulse are shown in a linear scale. The transmitted pulse of constant amplitude is depicted by its rectangular envelope and, based on a sound speed of 4.875 ft/ms, has a length of 4.875 ft. The ends of the envelope depict the leading and the trailing cycles of the wave train. The length of the "tail", or residue is taken as 1 ft.

FIGURE 4-3. SAMPLING OF DIRECT PULSE

A series of four pictures showing (i) the leading edge of the transmitted pulse sinusoid reaching the hydrophone, (ii) some designated time later when the wave train is first sampled, (iii) the trailing edge leaving the hydrophone, and (iv) a very short time later when the residue is sampled. The numbers on the pulse are associated with the delay time in microseconds as if

4-4

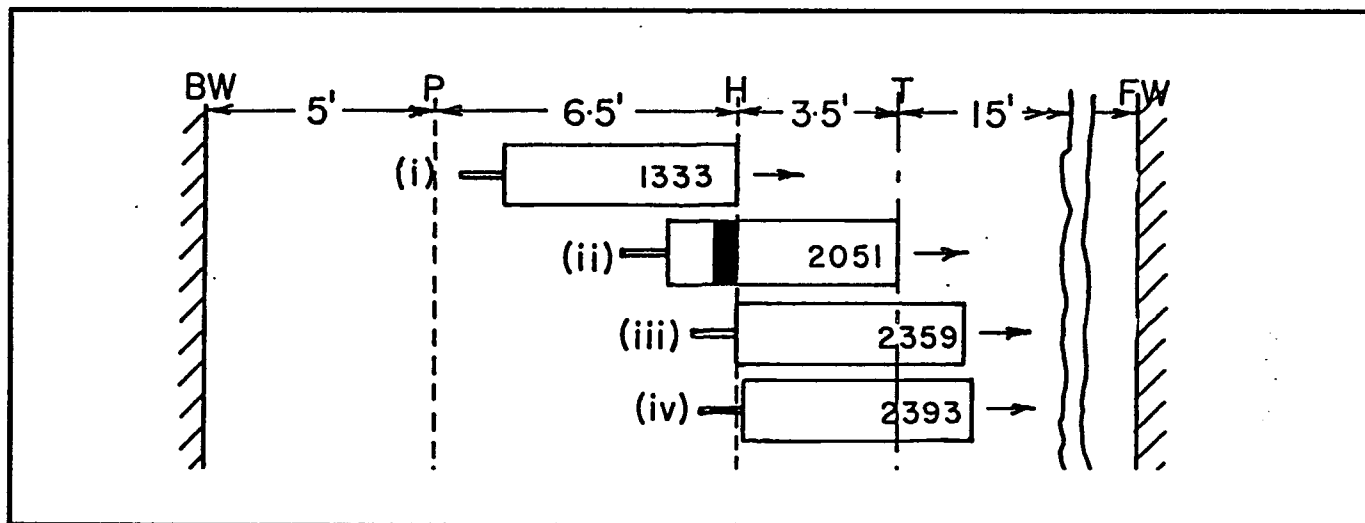the picture was frozen at that instance. The arrows indicate the direction of propagation. At this early moment, no reflection exists and the received wave train (shown darkened) sampled by the hydrophone in case (ii) corresponds to the direct signal and is a measure of the intensity of the incident signal.
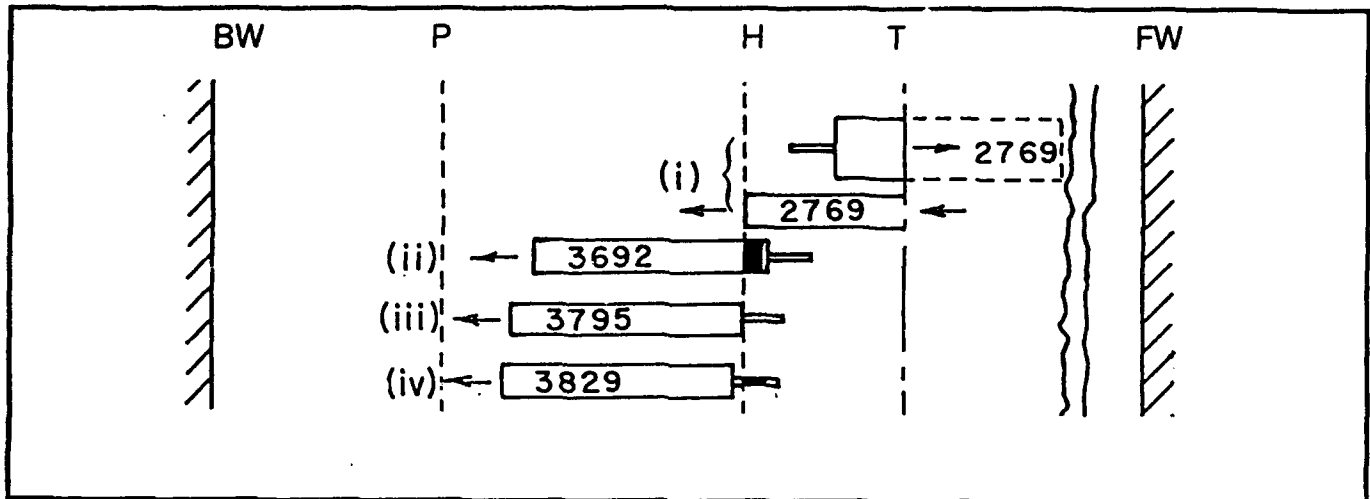

FIGURE 4-4. SAMPLING OF ECHO

In Figure 4-4, the incident wave has reached the target and reflections are shown (by solid rectangles). Recalling the discussion associated with Figure 3-7, the reflected pulse is sampled near the trailing edge to measure the maximum effect of the resonance as depicted in case (ii) of Figure 4-4. The amplitude of the reflection is generally much smaller, by some 20 db, and is therefore shown pictorially by a thinner rectangular envelope. At a resonance, the amplitude will even be smaller due to energy penetration into the target as discussed in Chapter 3. Of course, the sampling location within the envelope is immaterial for the nonresonance cases since the envelope remains rectangular. The reduction in target strength at the resonances allows one to determine the signature of a particular underwater target as shown in Figure 3-3.

The result of sampling in case (ii), whether away from resonance or at a resonance state, is due to the sum of infinite partial waves. Equation (2-33) from the theory section is repeated here for clarity.

$$\frac{\sigma_B}{\pi a} = \left| \sum_{n=0}^{\infty} f_n(x,\pi) \right|^2 = \left| \frac{2}{\sqrt{i\pi x}} \sum_{n=0}^{\infty} (-1)^n \varepsilon_n b_n \right|^2 \qquad (2-33)$$

The incident wave scatters all modes; and as long as there is wave incidence on the target, there always exist scattered waves of various frequencies. However, if sampling is slightly delayed to allow the trailing cycles of the reflected wave train to be sampled by the hydrophone as shown in case (iv), the sampling result will be that due to the reflection from the residue transient which is generally of negligible magnitude. The exception occurs when the target is at

a resonance state. At resonance, the target reradiates its stored energy at a single frequency because, as predicted by the resonant theory, only the energy associated with the resonance frequency would have penetrated into the target. The energy reradiation at the end of wave incidence at resonance is at a rate controlled by the damping of the target material and the radiation. The energy reradiation has a magnitude much larger than the reflection of the residue in the "tail"; and if sampling is made in this manner over a series of frequencies, the result is called the spectrogram of the reradiation or the free ringing curve with peaks at the various resonance frequencies. This is an alternative method to obtain the signature of the underwater target.

Figure 4-5 depicts the back wall reflection from the incident wave coming out from the back or baffled side of the projector. The amplitude of this reflection is too small to warrant serious concern pertaining to wave interference.
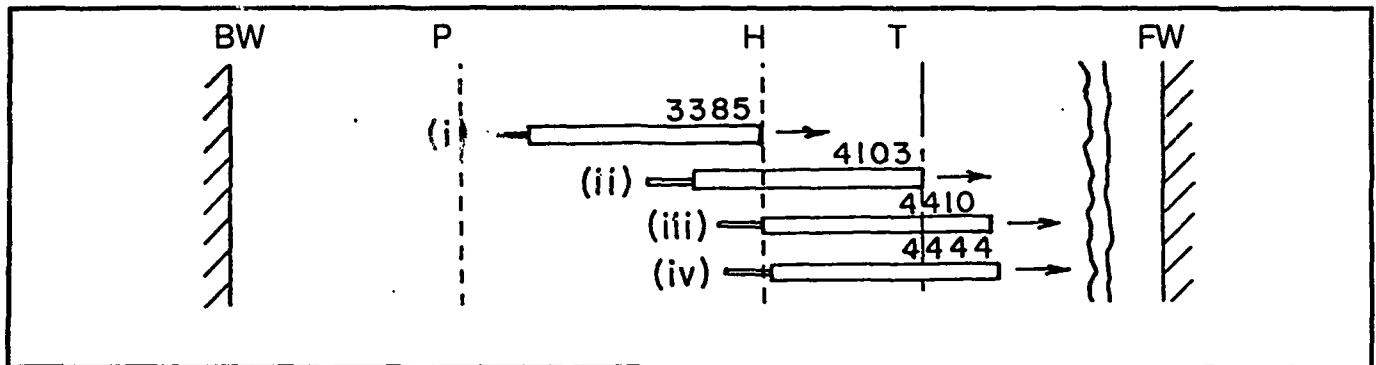

FIGURE 4-5. REFLECTION FROM BACK WALL

Figure 4-6 depicts the front wall reflection of the forward, incident wave. This pulse passes the hydrophone as depicted in Figure 4-3, proceeds to the front wall of the tank and comes back to the hydrophone after travelling through a distance of 43.5'. The amplitude of this reflected pulse is comparable to the first echo from the target in Figure 4-4, but because of an additional travel of 30', there is a considerable time delay in arrival at the hydrophone and it can be eliminated by time gating.

There is at least one more reflection worthy of consideration which is not depicted in these figures. That is the reflection from the free surface of the tank. The pulse would have travelled a distance of slightly more than 20'; 10' up from the projector to the free surface and then 10' down to reach the hydrophone. The corresponding time for the pulse to pass the hydrophone covers approximately a period from 4,300 to 5,300 μs. The amplitude of this reflection is variable depending on the directivity of the projector at the various incidence frequencies, and it may be comparable to that of the backscattered reflection. However, it is important to include this reflection in the study of wave interference because of its effect on the backscattered reflection and the ensuing reradiated. This limits the delay in sampling the reradiation of the target at resonance. There is a similar reflection coming from the bottom of the tank, but its amplitude is considerably smaller due to the high absorption of the redwood.
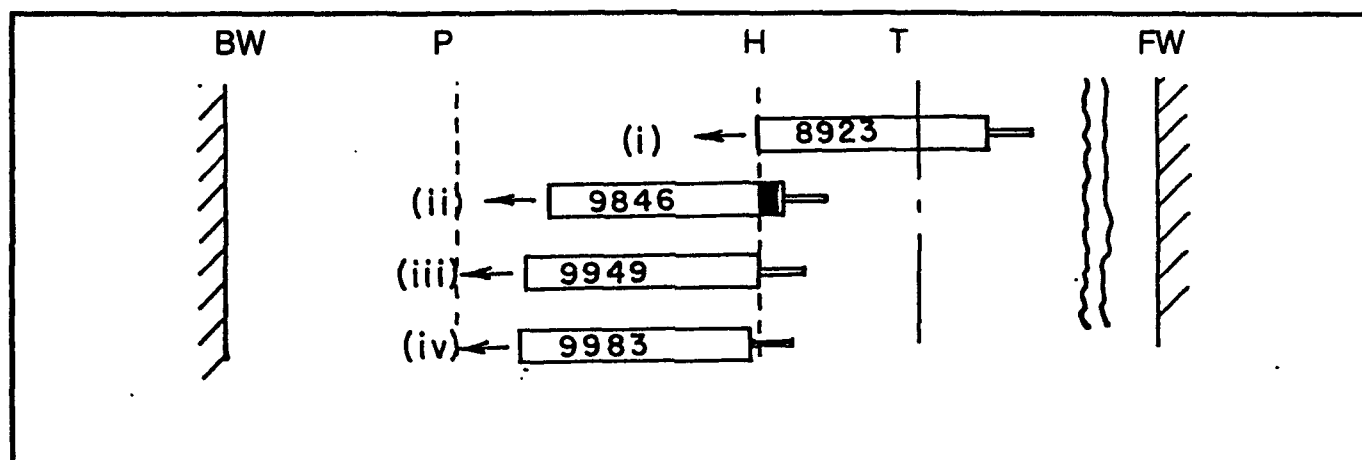
FIGURE 4-6. REFLECTIONS FROM FRONT WALL

Based on considerations outlined in the last few paragraphs, it seems that a sampling period devoid of serious wave contamination of an intended signal falls between the arrival of the backscattered return at 2796 μs to the arrival of the free surface reflection at about 4300 μs. The preferred sampling at the tail portion of the reflected pulse at about 3692 μs (see Figure 4-4 (ii)) considerably relaxes the choice of an allowable transmitted pulse width. As long as the distance from the sampling location of the reflected pulse to its trailing sinusoid is less than twice the target-hydrophone separation, no interference or overlap by the direct signal can take place irrespective of the transmitted pulse width. This is an important revelation since conceivably a pulse of longer pulse width is needed to excite large targets at resonance, and this is now permissible. For most of the experiments presented in this report, however, the transmitted pulse width of 1 ms seemed adequate, and it was chosen. This choice gave an additional advantage since the sampling of the incident and the reflected pulses occurred at different time periods, allowing each to be seen in its entirety in the scope screen as shown in Figure 4-7.

The standard arrangement to obtain the spectrograms of the target is when the projector, the hydrophone and the target are lined up along a diameter of the tank. To measure the bistatic scattering cross section or the reradiation rosetta and present the result in an angular plot, the hydrophone is located at offset positions (see Figure 3-6). The above analysis, however, can be applied in a similar manner. It can be shown that under certain hydrophone orientations, interference with the reradiation by the residual of the incident pulse is unavoidable. This will be addressed later when the measurement results are discussed.

The sampling location in the reflected pulse depends on receive time delay and the received pulse width. As discussed earlier, the first and last several cycles are avoided and since the amplitude of the reradiation decreased from cycle to cycle, it was necessary to make the received pulse width narrow, yet wide enough to enhance the signal to noise ratio. A choice of 0.1 ms for the received pulse width was found to be a good compromise for most of the experiments. The received sampling gate corresponding to this choice can be seen in lower trace of Figure 4-7.
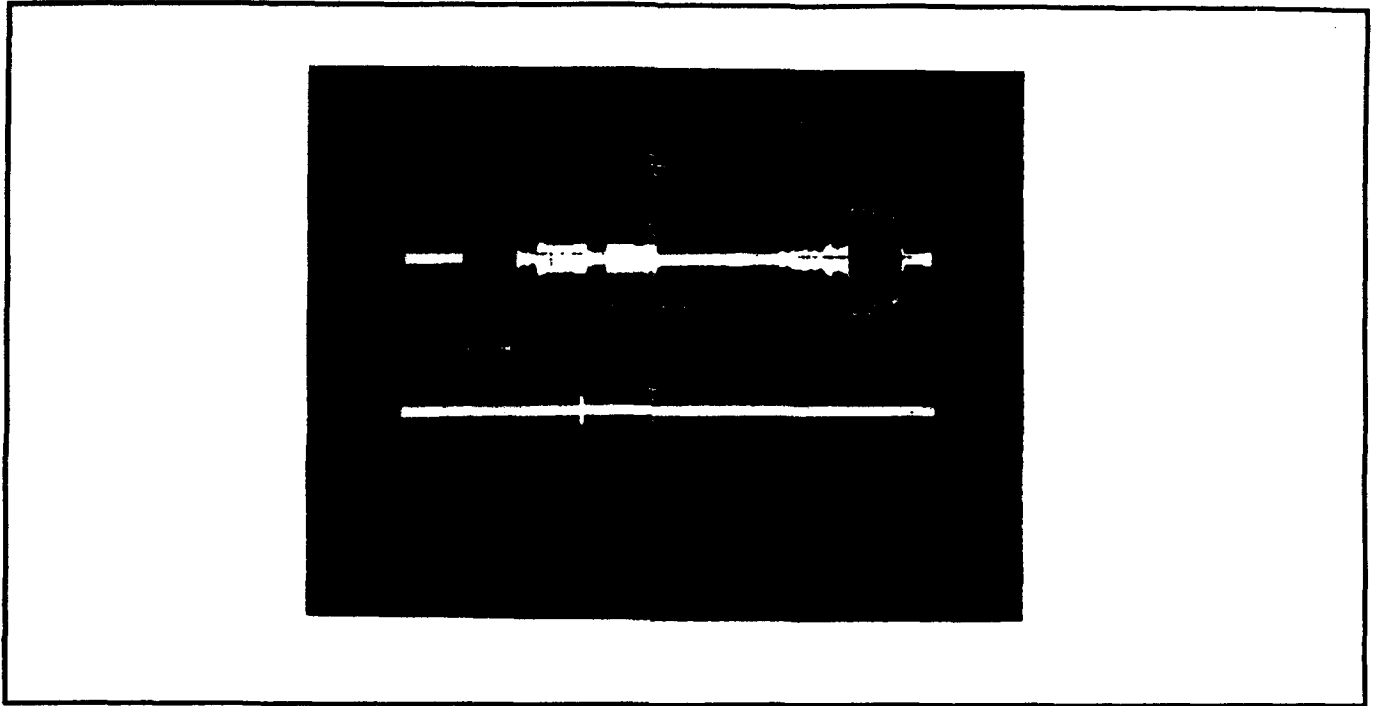
FIGURE 4-7. ACTUAL OSCILLOSCOPE TRACE

In addition to the received pulse width, the intensity of the incident wave also affects the signal-to-noise ratio. In general, the amplitude of the incident wave was set, within a specific frequency range, as high as possible without incurring saturation and distortion in the projector voltage. The same concept was applied to the receiving side with the amplification of the signal detected by the hydrophone. The product of the frequency and the pulse width gives the number of cycles impinging on the target per incident pulse. It was chosen such that a target always achieved equilibrium by the end of the insonifying. A large target might need a pulse of large pulse width and reduced repetition rate. For the samples used in the experiments, a repetition rate of 10 pulses per second was found to be adequate.

The above discussion presents, in fair detail, a comprehensive description of the approach and procedure in the choice of pertinent parameters for an exercise to extract the signature of an underwater target by an active sonar scheme based on resonances. Some of the findings, such as the relaxation of the restriction on the transmitted pulse width and the practicality of the parameter selections based on the fruitful execution of the scheme, have enhanced the probability of success with realistic targets in the future. Based on simple acoustical scaling, a comparison of several operational parameters of a typical target used in the present investigation with two future candidates is given in Table 4-1. As can be seen from the table, it is possible, without modifying the present experimental scheme, to increase the pulse width or the pulse repetition rate by, at least, a combined factor of 25 for the 36" model. Under this new condition, there will be some 900 sinusoidal impingements per second on the target at 2,778 Hz. For the 360" model, the impingements on the target could be increased to 90 per second at 278 Hz.

There is no restriction on further increase of the incident pulse width until several resonances of a target are secured by a corresponding decrease in pulse repetition rate. As long as the body of water is greater than $\lambda/4$ in its least dimension. For the 287 Hz case, this is 80'.

TABLE 4-1. PERTINENT OPERATIONAL PARAMETERS IN THE RST EXPERIMENTS

Operational Parameters	Present Model	Future Model 1	Future Model 2
Size (inches)	1	36	360
Incident Frequency (Hz)	100,000	2,778	278
Pulse width (ms)	1	36	360
Cycles in the pulse	100	100	100
Pulse rate (Hz)	10	10	10

CHAPTER 5

EXPERIMENTAL RESULTS

Many results were obtained based on the wide variety of targets measured; only a few sample results are given here. Even though these samples obviously are the best and the most representative, many others with good quality exist that could equally have been selected. Most of the samples were chosen particularly with regard to the verification of the theory and establishing a workable methodology for the classification of underwater targets via active sonar, which is the goal of the present investigation.

It is advantageous, at this point, to look at some additional theoretical solutions to be compared to the experimental results. In Chapter 2, theoretical plots were presented with discussion pertaining to the subtraction of the rigid response from the total response to leave the modal or resonant responses of the target. For simplicity, since there is only one k in the text from here to the end the subscript is dropped ($k_i = k$). Figure 5-1 shows the result of calculations by Gaunaurd and Brill[16,13] and presents the modal responses, in the ka domain, of an infinite solid cylinders and a hollow cylinder with aspect ratio of ID/OD = 2/3. The numbers beside the resonance peaks are the l index of the (n,l) mode.

The plots are for insonification by a plane wave, of constant amplitude, broadside to the axis of symmetry. It is an alternative form of the spectrogram of the reradiated return shown as the bottom trace in Figure 5-2. The theoretical data in Figure 5-1 does not include noise or any uncertainty that is associated with the real world. By comparison of the features between the theoretical, Figure 5-1 and the experimental Figure 5-2, such as the locations of the resonances, their respective amplitude (size) and shape will determine the validity of the measurements scheme and assumptions made. Note that the increasing frequency scale runs in opposite directions between the theoretical and the experimental.

A close examination of the theoretical curves in Figure 5-1 reveals that each mode has its own unique shape, amplitude, and location in the ka domain. Some resonances are wider than others, and the distance in the frequency domain between the modes is larger in hollow than in solid cylinders. This makes a hollow tube a better target for verification of the resonance theory. These unique characteristics will be used in this study to determine which mode has been experimentally determined and to compare how close it compares to theory. A review of classic vibration theory will reveal that the width of the resonances are dependent on the loss mechanisms in the structure. The targets used in this study have at least two mechanisms associated with the dissipation or loss of energy, namely the flow of energy from the target

(radiation) and the internal energy (heat). The heat will be dissipated to the surrounding water, but the process is much slower and is ignored. If a certain mode is an efficient radiator, the time domain signal of the reflected and the reradiated energy will show a quick decay and the frequency domain signal will have a large or wide resonance peak. The wide resonance indicates a low "Q" or lossy system. For these cases, it has been experimentally determined that the input energy used in this study was not sufficient, in many cases, to produce a peak much above the noise floor of the measuring system. If the heat is the dominant term, as in inefficient radiating modes, the time domain signal will have a slow decay and the frequency domain signal will have a very narrow modal response (high Q systems). These are the most likely modes to be observed experimentally, especially the ones in Figure 5-1 with the higher amplitudes. In these instances, both the frequency location and the other features, size and shape, are expected to have good theoretical to experimental correlation.
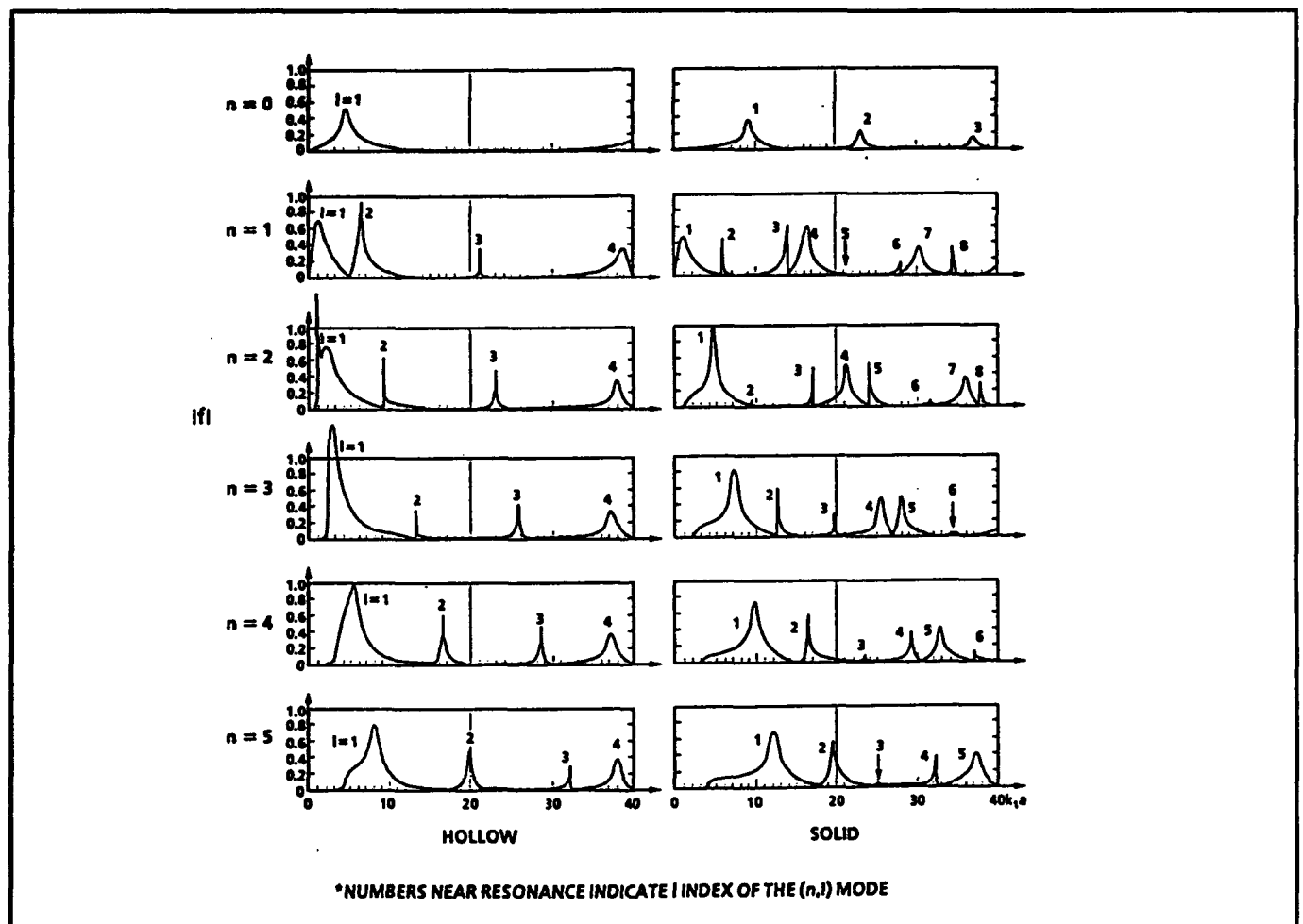

FIGURE 5-1. PREDICTED RESPONSE IN THE ka DOMAIN

At some frequencies or ka values, more than one mode may be excited. Not only would the incident energy in these cases be partitioned amongst all the modes near or at that ka value, but also the resulting peaks, due to reradiation from many modes, may not resemble any

one of the single theoretical modal responses. This phenomenon occurred rather regularly and might cast doubts about the verification of the RST predictions. However, there are remedies in the measurement of the monostatic reflections which can serve to remove most of the uncertainties. As examples of the discussions just presented, the (2,1), (2,4), and the (2,7), modes in Figure 5-1 for solid cylinders have wider (more lossy or lower Q) than the (2,3) and (2,5) modes and are less likely to be excited in an experiment than the (2,3) and the (2,5) modes. The (2,2) mode, which has a very small amplitude, is also unlikely to be observed because of the noise in the experimental system.
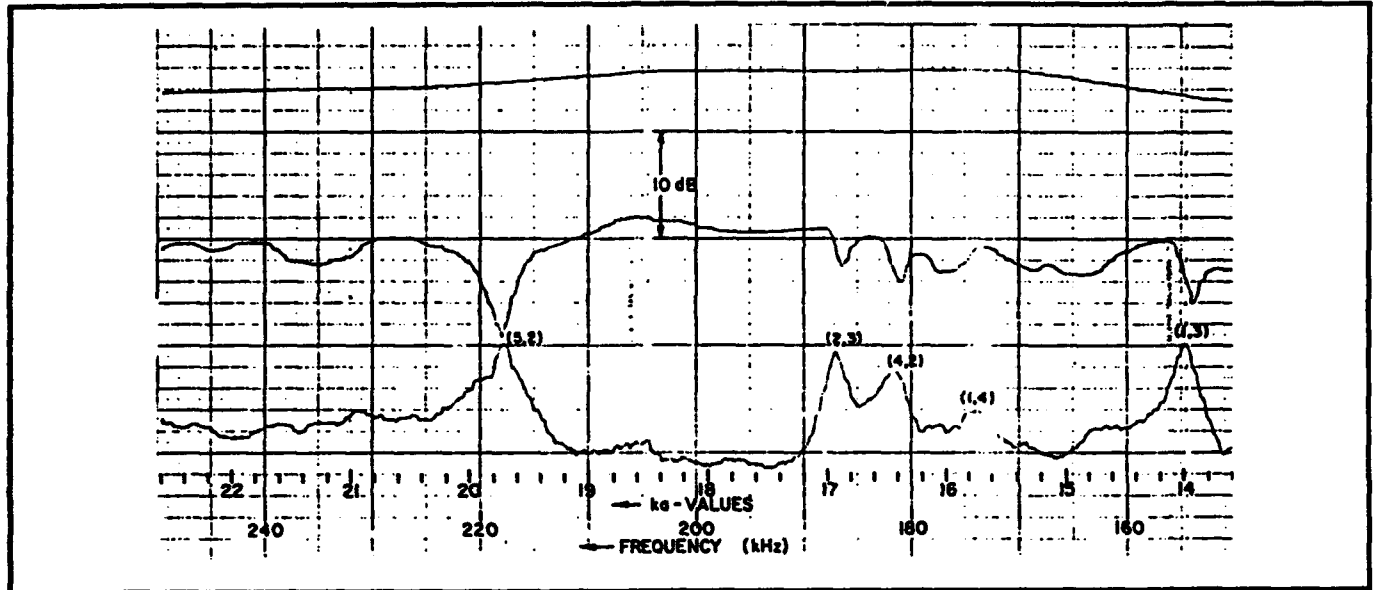

FIGURE 5-2. MEASURED RESONANCES IN A SOLID ALUMINUM ROD

Other calculations, which appear in the literature, are much less popular than those of the modal response in Figure 5-1. The most common presentation is a plot of the monostatic cross section which expresses the steady state (equilibrium) backscattered energy return. These calculations predict the drop in target strength and can be compared to the middle curve of the measured data plots in Figure 5-2. For solid cylinders, the response is predicted by Equation (2-33);

$$\frac{\sigma_B}{\pi a} = \left| \sum_{n=0}^{\infty} f_n(x,\pi) \right|^2 = \left| \frac{2}{\sqrt{i\pi x}} \sum_{n=0}^{\infty} (-1)^n \varepsilon_n b_n \right|^2 \qquad (2-33)$$

It is important to note that both the reflected and the reradiated energy are affected at or near a resonant frequency. Even though either can be used to identify the resonance, in this work both are measured and presented in order to provide direct comparison to many published predictions.

If the target is suspended horizontally, the reflected energy, in polar form, will result in a pattern that has broad lobes at and near broadside and spikes at the flat ends. It is commonly referred to as a "butterfly" pattern. At a resonance, this pattern is characterized by a deep notch in the backscattered direction at $\theta = \pi$. For example, see Figure 8 in the work by Brill and Gaunaurd[13] as well as Figure 5-3 in this report shows a notch in the backscattered signal which, of course, signifies reduced energy return at resonance and a subsequent increase in the reradiated energy at broadside. This leaves little doubt that the resonances of cylinders is a broadside phenomenon.

For a cylinder suspended vertically, the polar pattern, or directivity pattern, of the reradiation is theoretically given by $|\cos n\theta|$ which results in the familiar "figure 8" pattern for $n = 1$ and the "four-leaf clover" pattern for $n = 2$, etc. Figure 5-4 is an example of a measured ros

Many ka domain or spectral plots similar in form to Figure 5-1 are given in following figures. Figures 5-5 pertains to the solid aluminum cylinders of diameter of 1.867". As with all spectral plots, the range of the experiment is given by the frequency and corresponding ka scale.

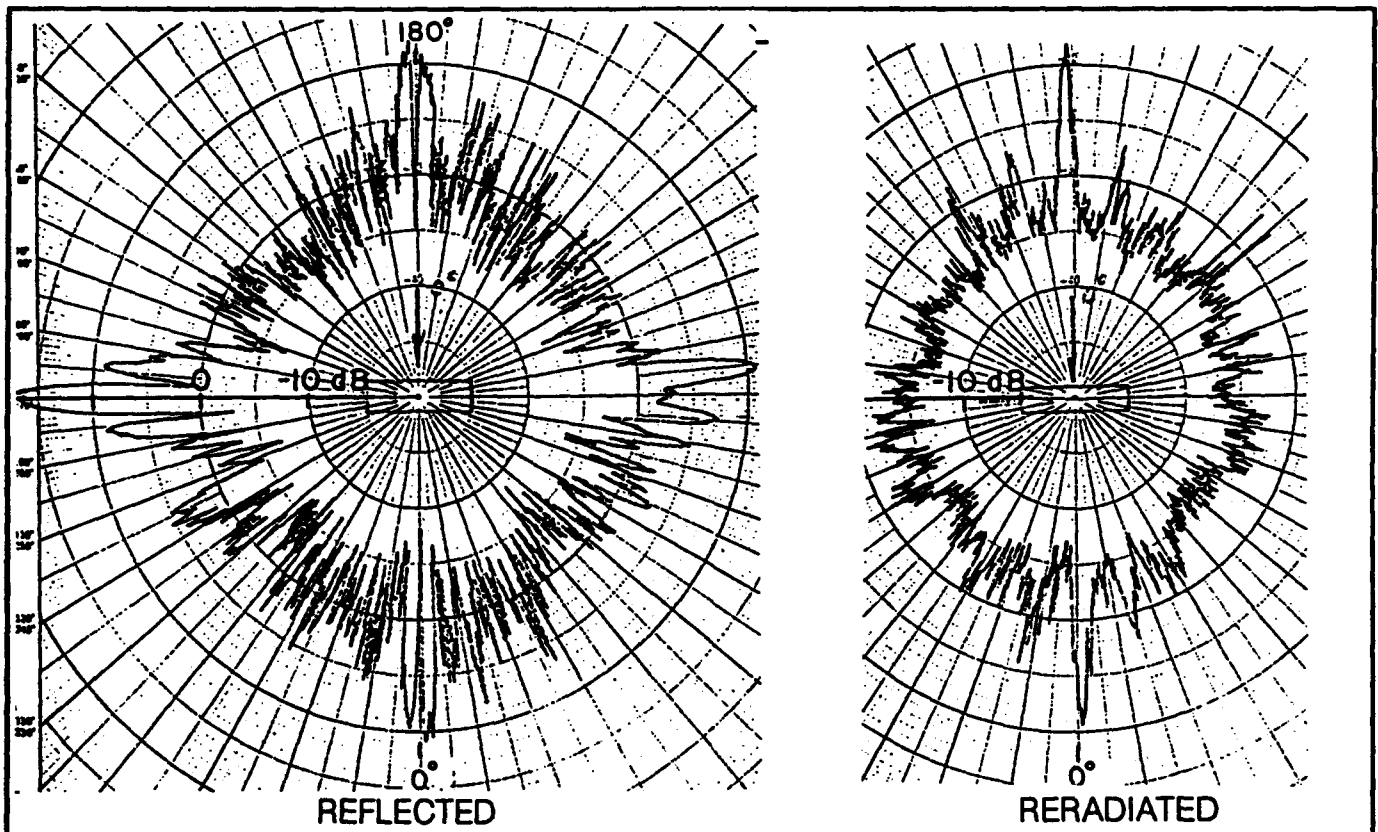FIGURE 5-3. REFLECTED AND RERADIATED ENERGY VERSUS ASPECT ANGLE AT RESONANCE

Generally the experimental results checked very well with the theoretical predictions presented in Figures 5-1 for cylindrical targets. Table 5-1 provides a tabular comparison of the theory and experimental results.
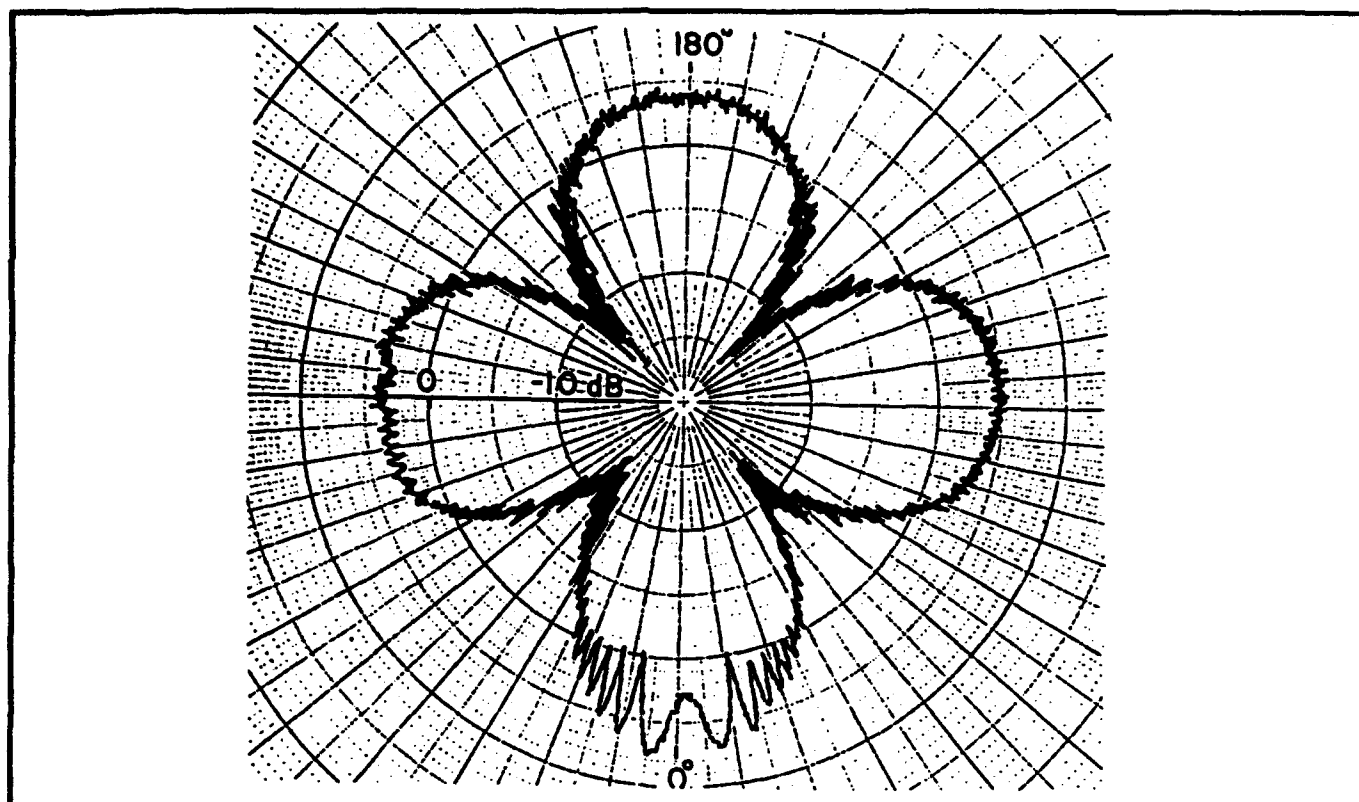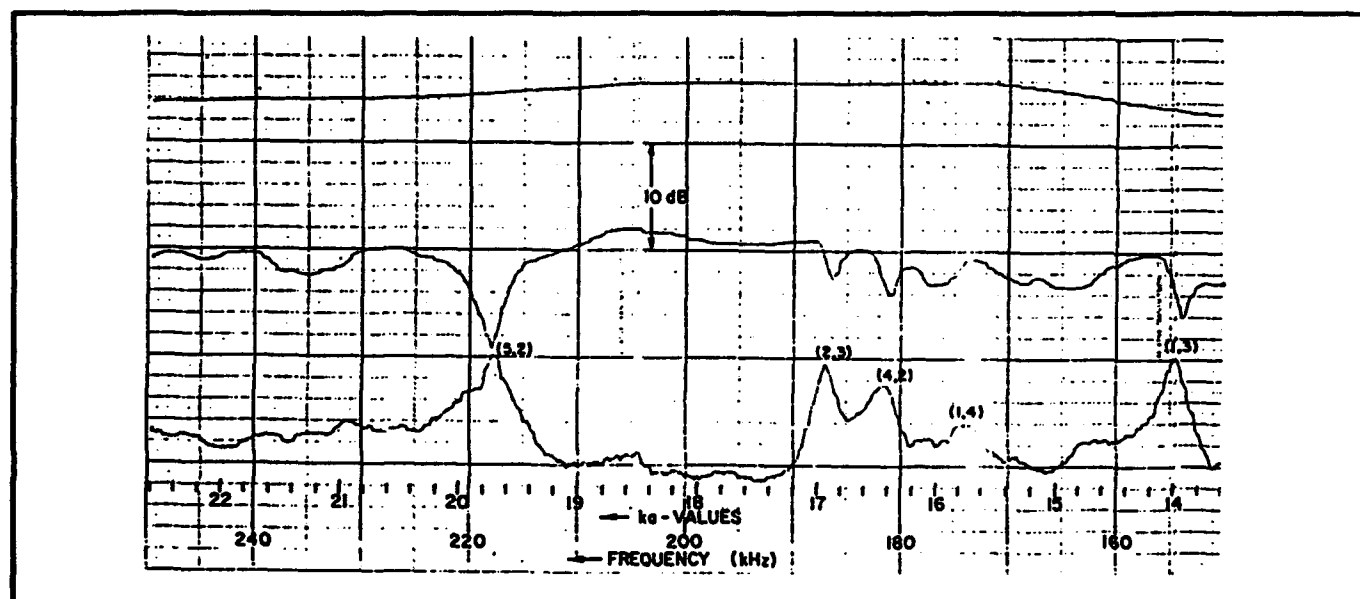
FIGURE 5-4. RERADIATED ROSETTA FOR $n = 2$

FIGURE 5-5. SPECTROGRAM FOR A 1.867" BY 6" SOLID CYLINDER

TABLE 5-1. RESONANCES OF A 1.876" BY 6" SOLID ALUMINUM CYLINDERS

Mode Number		1,2	1,3	1,4	2,2	2,3	3,3	4,2	4,3	5,2	6,1
ka	T*		13.9	16.0		16.8		16.2		19.5	
ka	M*		14.0	15.8		16.9		16.4		19.7	
Δka			0.1	0.2		0.1		0.2		0.2	
Frequency (kHz)	M*		154	174		187		181		218	
T* = Theoretical, M* = Measured											

As shown in the previous figure and table, the prominent peaks are at 154, 174, 187, 181, and 218 kHz correspond to the (1,3), (1,4), (2,3), (4,2), and (5,2) mode which occur at ka= 14.0, 15.8, 16.9, 16.4, and 19.7 respectively. The variance in the data is directly related to the width of the theoretical resonances as shown in figure 5-1 due to the low signal as discussed previously. The noisiness of the data makes determination of the exact peak difficult.
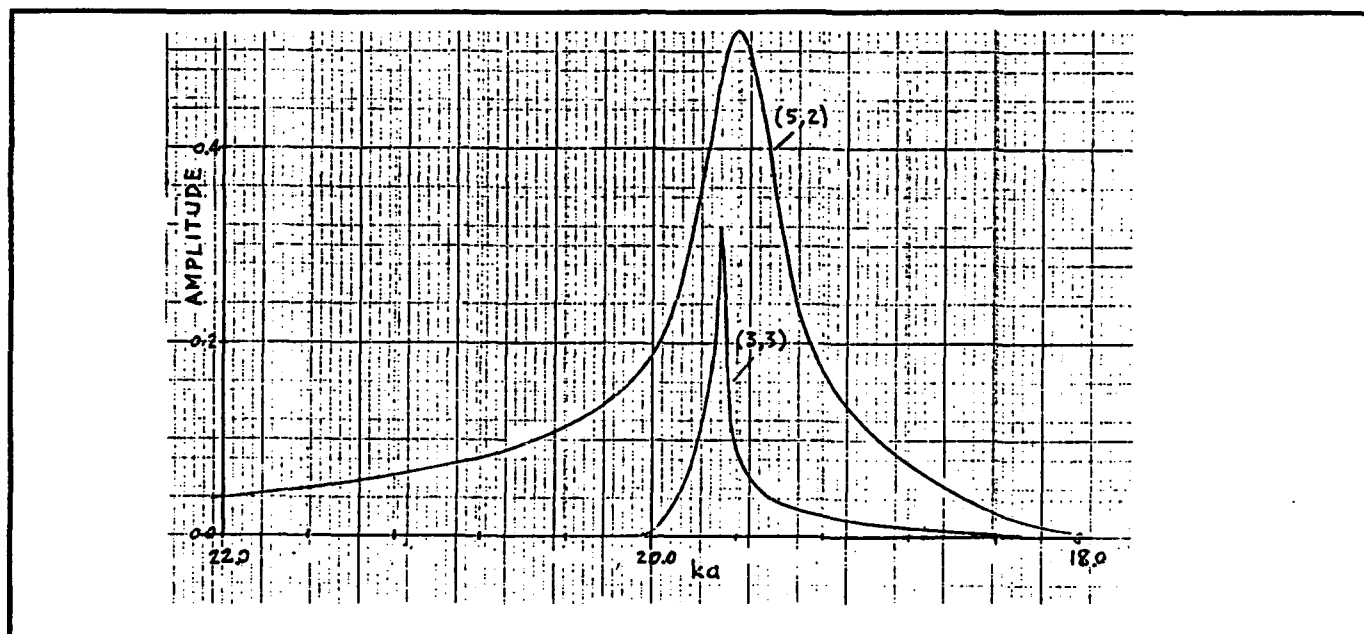
FIGURE 5-6. EXPANDED VIEW OF (5,2) AND (3,3) MODES

The peak at 154 kHz is due to the clustering of the (1,3) mode at ka=13.9 and the (6.1) mode at ka=14.1. When clustering like this occurs, the resultant peak is also affected by the relative amplitude of the resonance peak in the cluster. A case in point is the (3,3) mode which has a ka value of 19.6 and is very near that for the (5,2) mode. Even though both these resonances are very narrow and should have good experimental results the combination results in a larger error. The two resonances are plotted in Figure 5-6 with an expanded scale to show this relationship.

In Figure 5-5 The resonance was labeled for the (5,2) mode since it is dominant. Figure 5-7 is the spectrogram for a 0.978" by 6" solid aluminum cylinder and Table 5-2 is the tabular form.
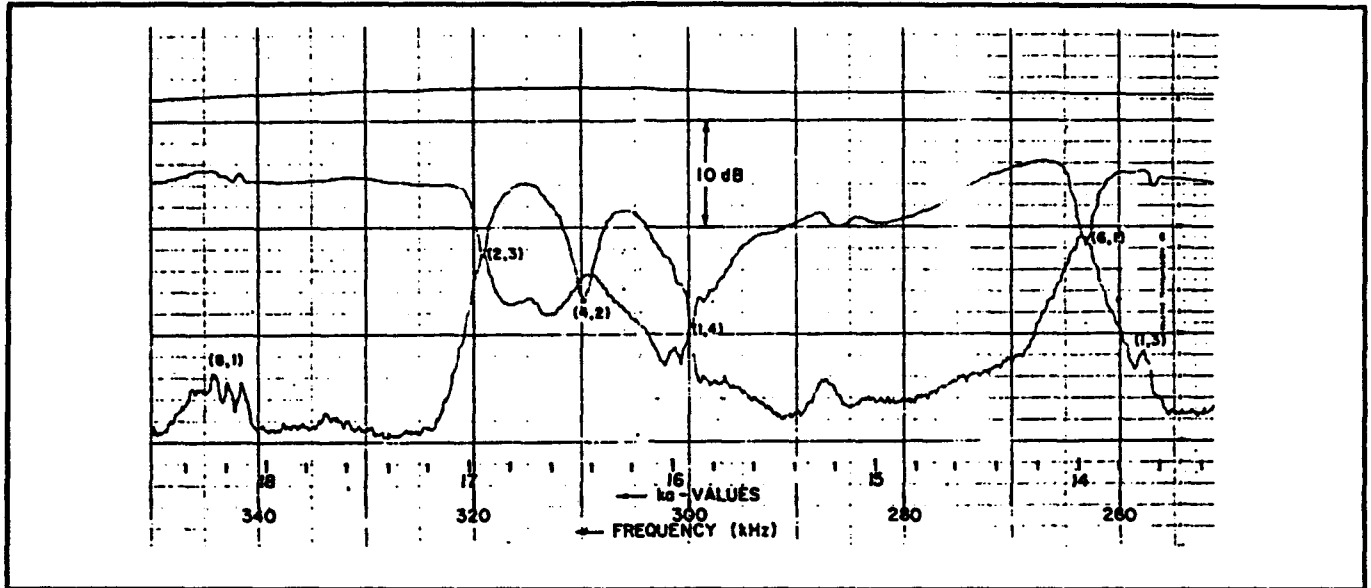

FIGURE 5-7. SPECTROGRAM FOR A 0.978" BY 6" SOLID CYLINDER

The prominent resonance frequencies occurred at 264, 300, 310, and 319 kHz. These frequencies correspond to the (6,1), (1,4), (4,2), and (2,3) modes at $ka=$ 14.0, 15.9, 16.4, and 16.9, respectively. These values are within 0.1 of theoretical. Due to the smaller size, the (6,1) mode ($ka=$ 14.0) and the (1,3) mode ($ka=$13.6) can be determined separately. The apparent resonance at 288 kHz ($ka=$15.2) seemed to indicate a resonance that is not covered by theory. The peak at 343 kHz ($ka=$18.3) is a classic example of a wide bandwidth resonance that is difficult to excite. Again, the flatness and the noisiness of the bottom trace in Figure 5-7 indicates that the data was taken near the noise floor of the measurement equipment and in several cases the reradiated energy was barely detectable above this noise floor.

TABLE 5-2. RESONANCES OF A 0.9.876" BY 6" SOLID ALUMINUM CYLINDERS

Mode Number		1,2	1,3	1,4	2,2	2,3	3,3	4,2	4,3	5,2	6,1
ka	T^*			16.0		16.2		16.3			14.1
ka	M^*			15.9		16.0		16.4			14.0
Δka				0.1		0.2		0.1			0.1
Frequency (kHz)	M^*			300		319		310			264
T^* = Theoretical, M^* = Measured											

5-7

Figure 5-8 is the spectrogram for a 0.740" by 6" solid aluminum cylinder spanning frequencies from 350 to 450 kHz. Despite the raised noise floor on the data plot (reduced signal level), prominent peaks can be detected at 396, 413, and 425 kHz which corresponds to (1,4), (4,2), and (2,3) modes at ka values of 15.8, 16.4, and 16.8. The reduced size of the target provides an advantage of separating the modes and a disadvantage of a reduced signal level. Table 5-3 provides a tabular form of the data.
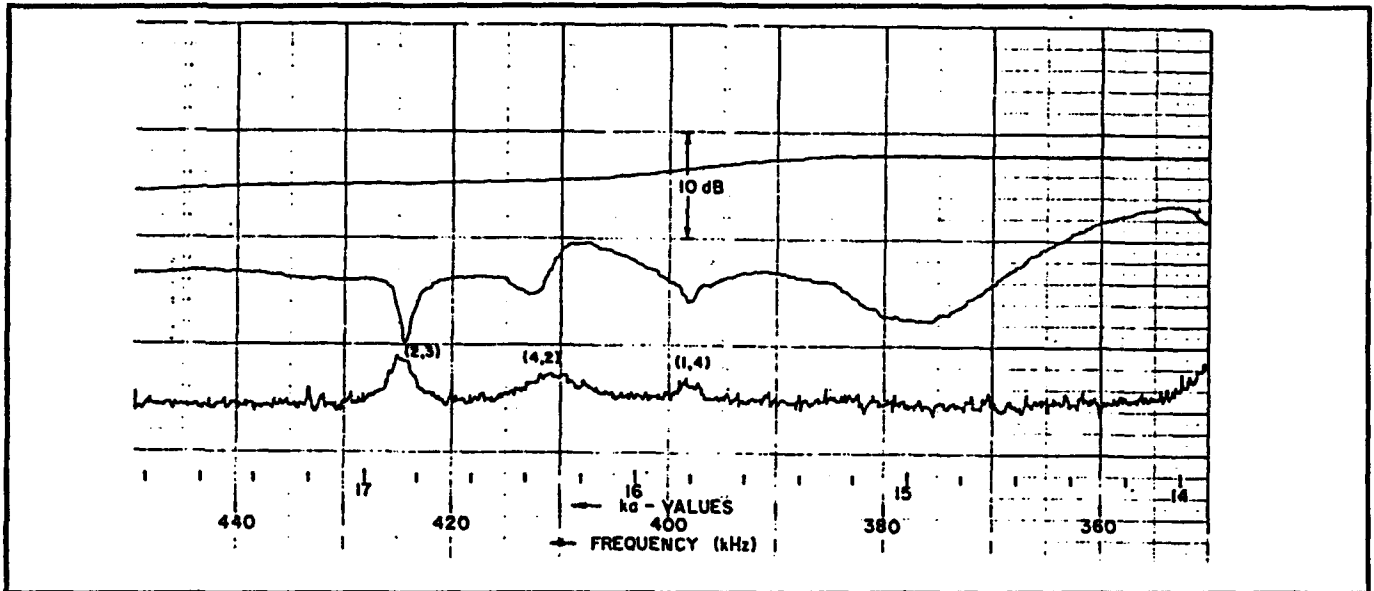

FIGURE 5-8. SPECTROGRAM FOR A 0.740" BY 6" SOLID CYLINDER

TABLE 5-3. RESONANCES OF A 0.74" BY 6" SOLID ALUMINUM CYLINDERS

Mode Number		1,2	1,3	1,4	2,2	2,3	3,3	4,2	4,3	5,2	6,1
ka	T*			16.0		16.8		16.2			
ka	M*			15.8		16.8		16.3			
Δka				0.2		0.0		0.1			
Frequency (kHz)	M*			398		425		413			
T* = Theoretical, M* = Measured											

This concludes the data for a target of a single geometry, an infinite solid cylinder, and the results are presented in Table 5-4 which shows that indeed the resonances occur at the same ka and at different frequencies for the different diameter targets.

TABLE 5-4. RESONANCES OF SOLID CYLINDERS WITH THREE DIFFERENT DIAMETERS

Mode Number		1,2	1,3	1,4	2,2	2,3	3,3	4,2	4,3	5,2	6,1
Frequency (kHz)	1˙		154	174		187		181		218	
	2˙			300		319		310			264
	3˙			398	425		413				
ka	1˙		14.0	15.8		16.9		16.4		19.7	
	2˙			15.9		16.9		16.3			14.0
	3˙			15.8		16.8		16.3			

1˙=> Diameter =1.867", 2˙=> Diameter =.987", 3˙=> Diameter= .74"

Figure 5-9 shows the comparison of the theoretical and the measured shape of the (1,2) and the (2,3) mode of a 0.989" diameter solid aluminum cylinder. The agreement is quite good.
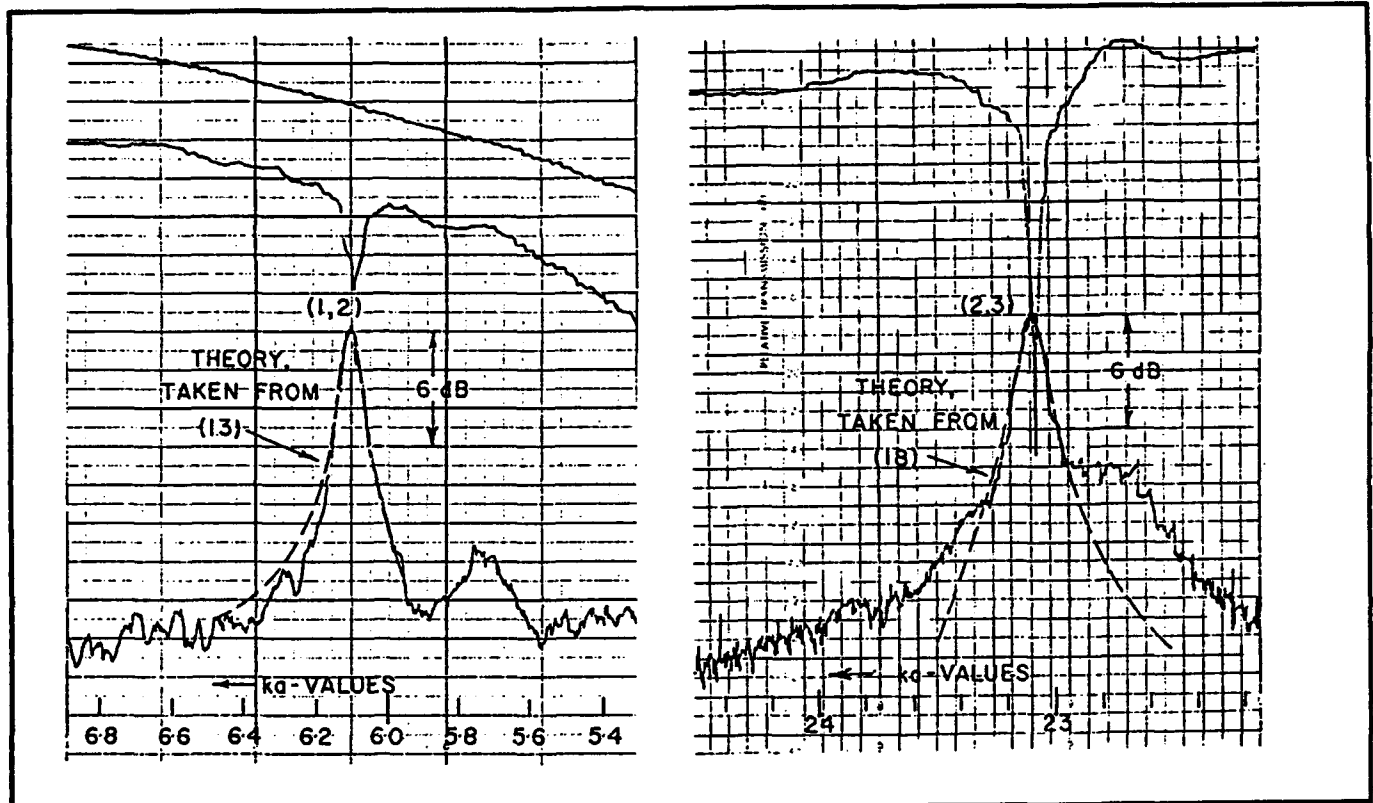

FIGURE 5-9. DETAILED SPECTROGRAM OF A (1,2) AND A (2,3) RESONANCE

Figure 5-10 comprises three spectral plots for a hollow aluminum cylinder with an ID/OD ratio of 2/3 and a diameter of 0.75". The three plots cover the frequency ranges from 50 kHz to 450 kHz or ka range from 2 to 18. The convergence and the reduction in amplitude of the direct, reflected and reradiated traces at ka = 2 is an indication that we are reaching the limit of the test set-up and higher power levels are required.
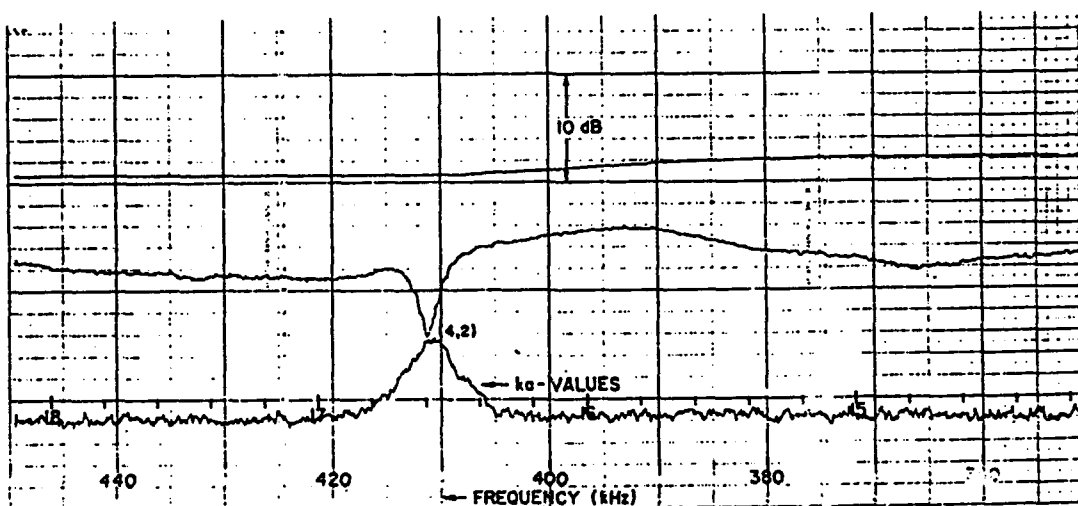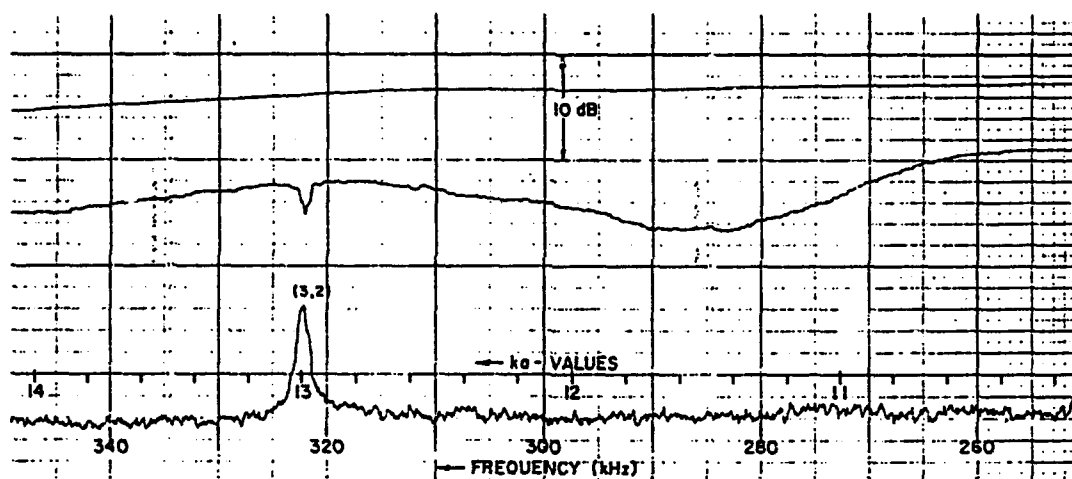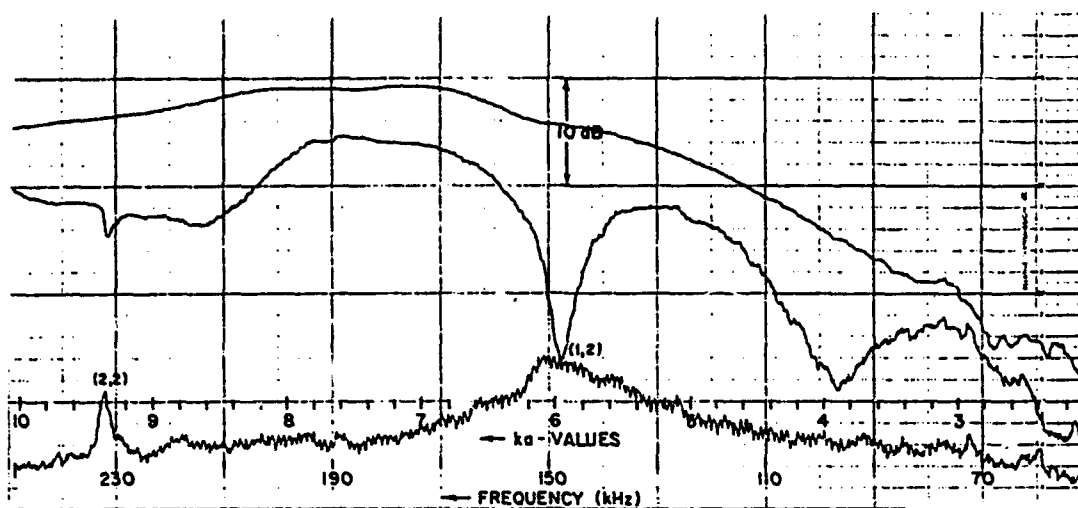
FIGURE 5-10. SPECTROGRAM OF A 0.75" DIAMETER HOLLOW CYLINDER

Table 5-5 is a tabular form of the data from the previous figure. Figure 5-11 provides the spectrogram for a 1.5" diameter hollow cylinder with the same aspect ratio (2/3) over a range of frequencies from 50 to 400 kHz and Table 5-6 provides the tabular form of the data. The spectral plots for the hollow tubes show more widely spread peaks and dips as predicted by the theory. Table 5-7 provides a comparison between the two cylinders previously presented. Again the ka values agree in each mode and the frequency is different. Measurements for these two cylinders revealed only three common modes.

TABLE 5-5. RESONANCES OF A 0.75" DIAMETER HOLLOW ALUMINUM CYLINDER

Mode Number		1,2	1,3	1,4	2,2	2,3	3,2	3,3	4,2	4,3	5,2	6,1
ka	T*	6.0			9.3		12.9		16.4			
ka	M*	5.9			9.4		13.0		16.6			
Δka		0.1			0.1		0.1		0.2			
Frequency (kHz)	M*	148			234		322		412			
T*= Theoretical, M*= Measured												

TABLE 5-6. RESONANCES OF A 1.5" DIAMETER HOLLOW ALUMINUM CYLINDER

Mode Number		1,2	1,3	1,4	2,2	2,3	3,3	4,2	4,3	5,2	5,3	6,1
ka	T*	6.1			9.3	23.0	25.4	16.4	28.6	20.0	31.4	
ka	M*	6.1			9.4	23.1	25.6	16.6	28.6	20.0	31.4	
Δka		0.1			0.1	0.1	0.2	0.2	0.0	0.0	0.0	
Frequency (kHz)	M*	75			115	286	318	208	355	258	390	
T*= Theoretical, M*= Measured												

TABLE 5-7. RESONANCES OF HOLLOW CYLINDERS WITH TWO DIFFERENT DIAMETERS

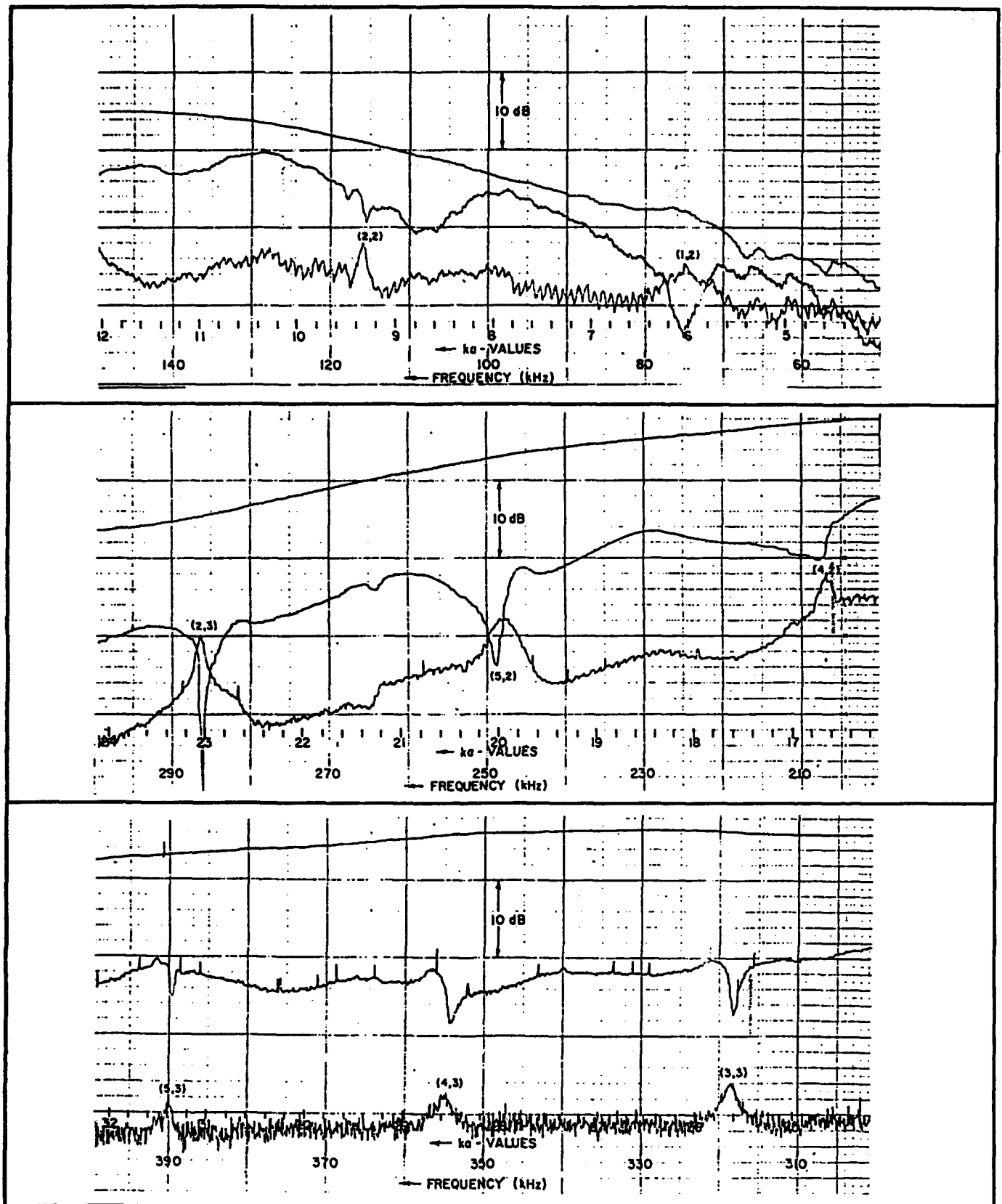| Mode Number		1,2	2,2	2,3	3,2	3,3	4,2	4,3	5,2	5,3	6,1
Frequency (kHz)	1*	148	234		322		412				
	2*	75	115	286		318	208	355	248	390	
ka	1*	5.9	9.4		13		16.6				
	2*	6.1	9.4	23.1		25.6	16.6	28.6	20.0	31.4	
1*=> Diameter=0.75", 2*=> Diameter=1.5"											

FIGURE 5-11. SPECTROGRAM OF A VERTICAL 1.5" DIAMETER HOLLOW CYLINDER

The plots up to this point pertain to targets suspended with their axis in the vertical position. In Figures 5-12 the same 1.5" hollow cylinder with aspect ratio of 2/3 was suspended with its axis in a horizontal position. Since the case of normal incidence prevailed they illustrate the effect, or the lack of it, of the positioning of the target.
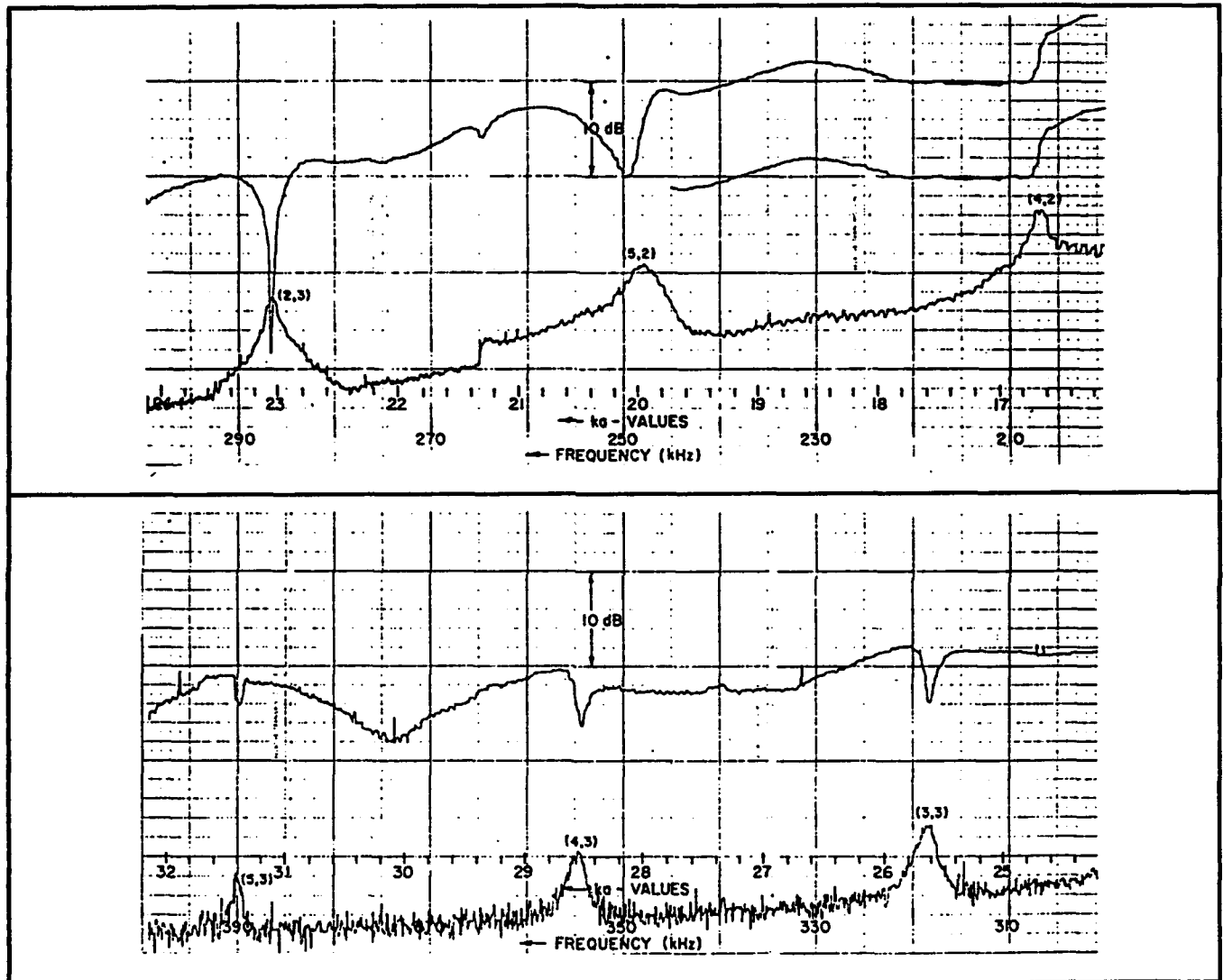

FIGURE 5-12. SPECTROGRAM OF A HORIZONTAL 1.5" DIAMETER HOLLOW CYLINDER

Next supporting data will be supplied to prove that the circumferential directivity pattern of the reradiation is given by $|\cos n\theta|$ which results in the familiar "figure 8" pattern for $n = 1$ and the "four-leaf clover" pattern for $n = 2$, etc. Figure 5-13 shows two "Rosetta" patterns for the same cylinder at two different frequencies. The theoretical curve is provided on portions of the curve in dotted lines. The oscillations around $\theta = 0°$ is due to interference between the residual of the direct energy and the reradiated energy.

Figure 5-14 is a comparison of the "Rosettas" for two different diameters (1.5" and 6.0") hollow aluminum cylinders with the same aspect ratio of 2/3.
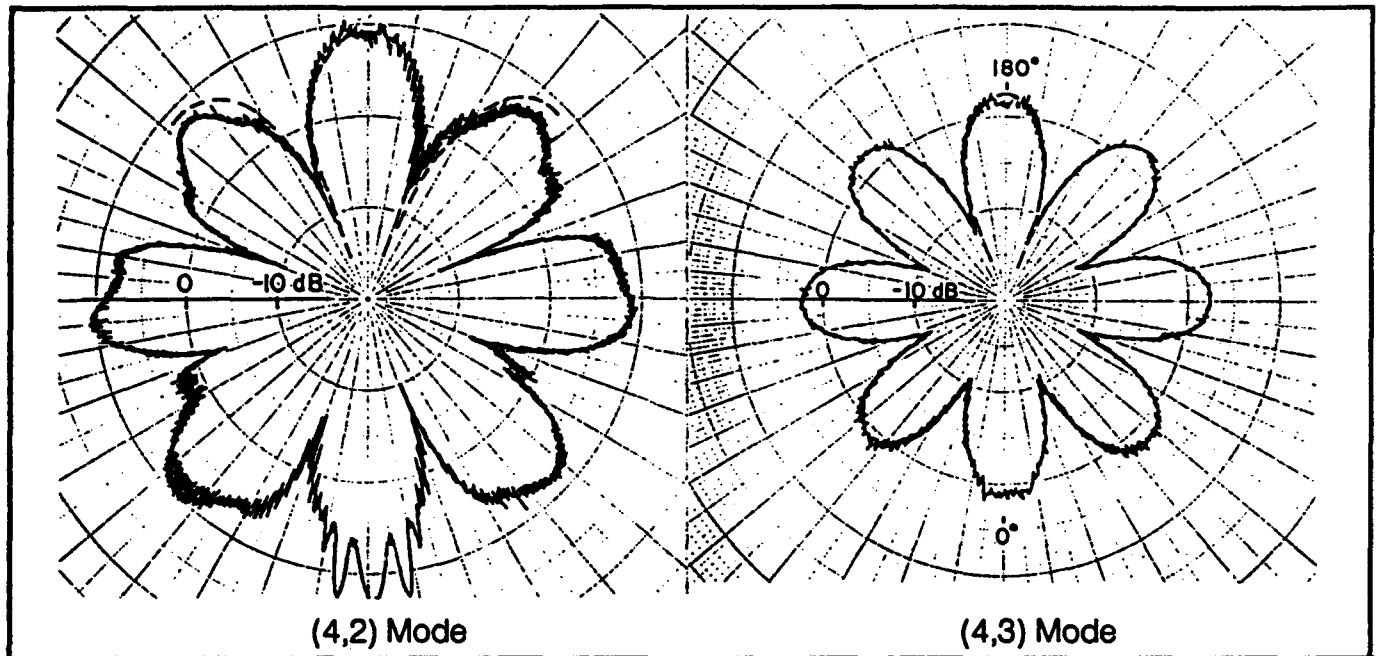
(4,2) Mode   (4,3) Mode

FIGURE 5-13. ROSETTAS OF THE (4,2) AND (4,3) MODE FOR A 1.5" HOLLOW CYLINDER

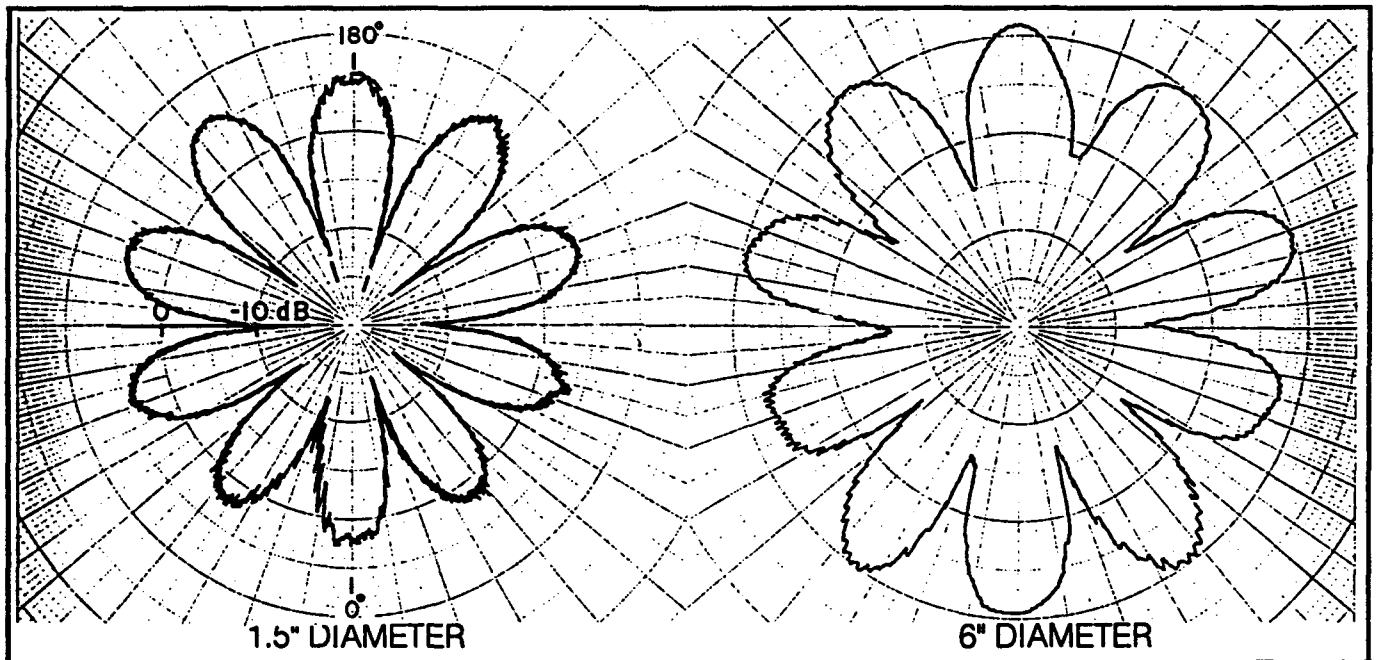1.5" DIAMETER   6" DIAMETER

FIGURE 5-14. ROSETTAS OF THE (5,2) MODE FOR TWO DIFFERENT DIAMETERS

Figure 5-15 is the "Rosettas" for the (2,3) and (3,3) mode for 1.5" hollow aluminum cylinder with aspect ratio of 2/3 showing that the first index, n, is for the circumferential wave which affects the rosetta while the second index, ℓ, is for the internal waves which is not propagated into the water.
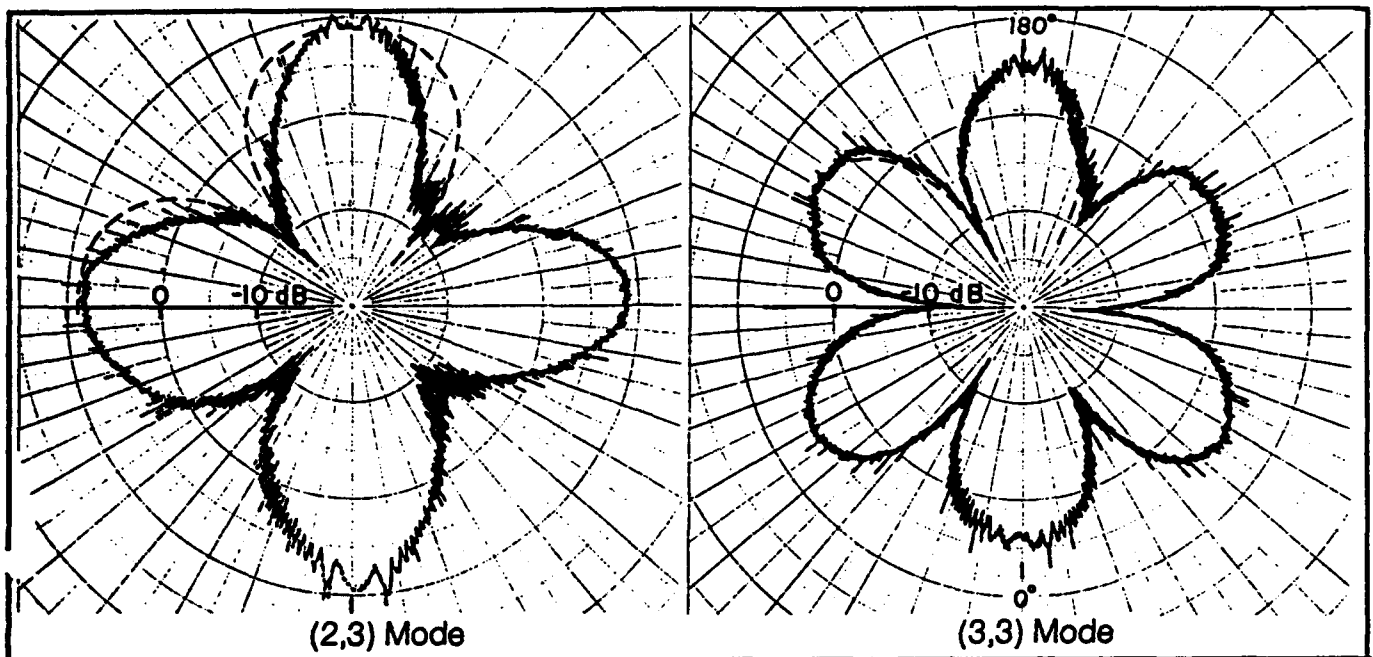
(2,3) Mode   (3,3) Mode

FIGURE 5-15. ROSETTAS OF THE (2,3) AND (3,3) MODE FOR A HOLLOW CYLINDER

As stated previously some times there are more than one mode present at a given *ka* location and the resultant shape and directivity pattern will be the sum of all modes excited. Figure 5-16 is a good example of that process. The measured data is given in the solid lines and the theoretical (in the upper left hand quadrant) is given as a dashed line for a 1.5" diameter hollow aluminum cylinder with aspect ratio of 2/3 measured at 161kHz. The agreement is good.

The final experiment associated with cylinders was to measure the effect of the target being close to but not at broadside. Figure 5-17 presents the results of a very narrow portion of the spectrogram of a 1.5" hollow cylinder with the (2,3) mode excited. The target was tested at 0°,2° ,4°, and 10° from broadside. The trend of the data was for the resonance to move to a lower frequency and for its amplitude to decrease until at 10° the resonance is barely distinguishable.
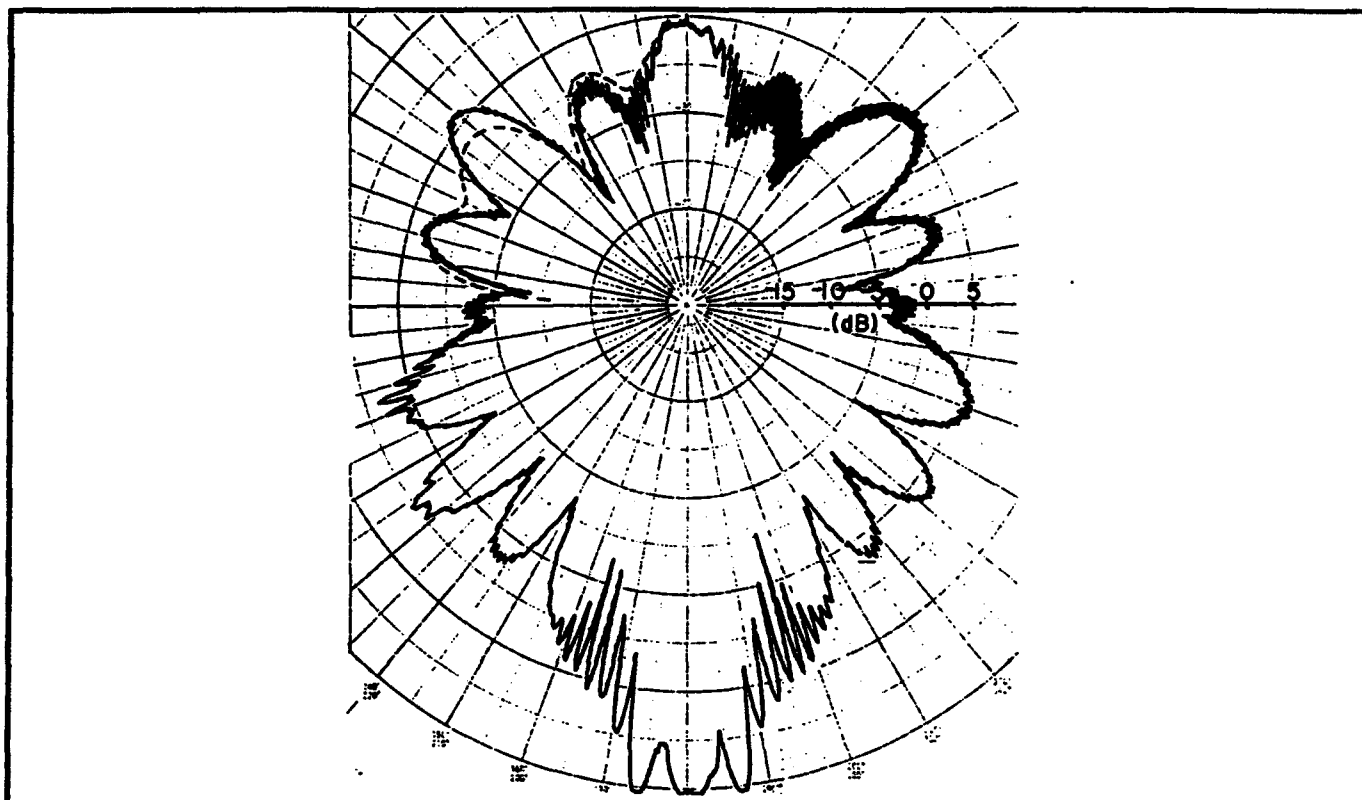
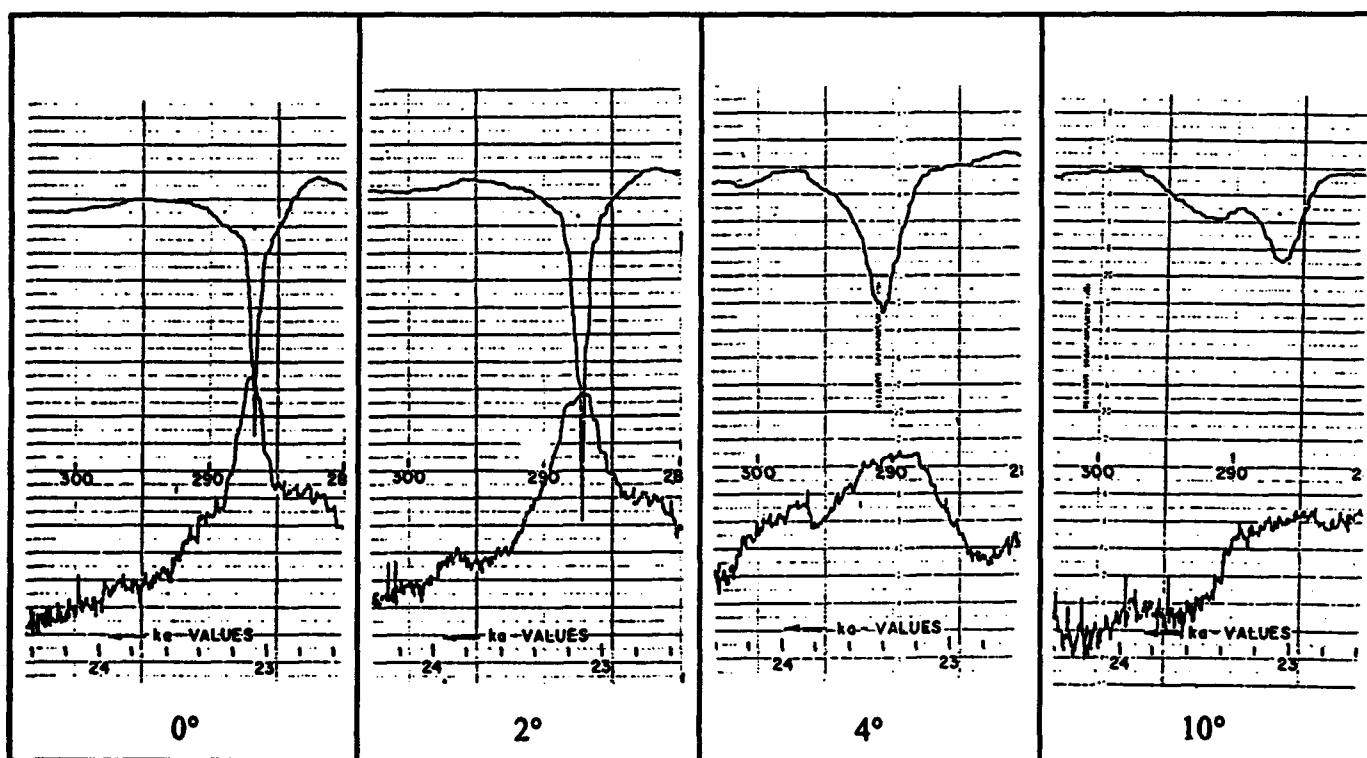FIGURE 5-16. ROSETTA SHOWING EFFECT OF TWO EXCITED MODES

FIGURE 5-17. DEPENDENCE OF THE (2,3) MODE ON ANGLE OF INCIDENCE

Considerations and measurements to this point have been associated with cylinders which are strictly a broadside phenomenon. This is not the case in the Figures 5-18 through 5-22, which provides spectral results from more realistic targets: a 1.4" by 7" solid spheroid and a 3.5" by 7" hollow spheroid with their major axes in the horizontal orientation. Figure 5-18 presents the backscattered curve and the spectrogram for the 1.4" by 7" solid aluminum spheroid at normal incidence to its major axis (broadside), while Figure 5-19 shows the same when wave incidence is at the nose of the spheroid.
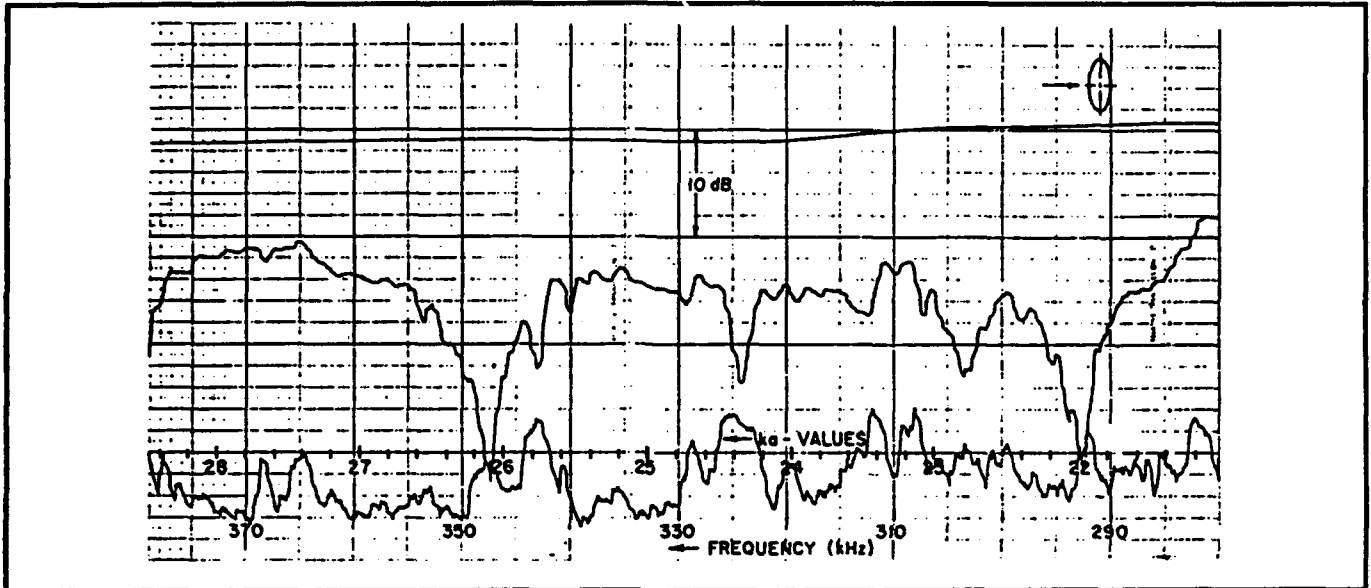
FIGURE 5-18. SPECTROGRAM OF A 1.4" BY 7" SOLID SPHEROID AT BROADSIDE
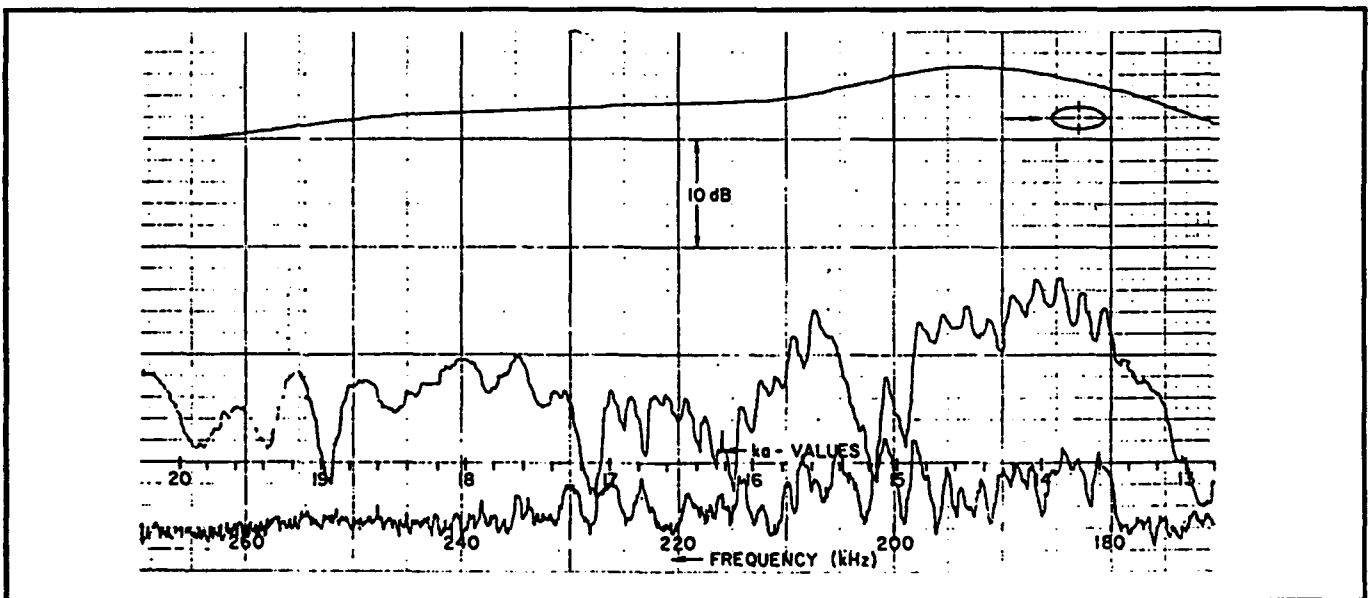
FIGURE 5-19. SPECTROGRAM OF A 1.4" BY 7" SOLID SPHEROID AT END FIRE

The next three figures pertain to spectral results from a 3.5" by 7" hollow brass ellipsoid. Broadside impingement was in the normal direction for the results in Figure 5-20 and 2.5° and 10° off the normal for those in Figures 5-21 and 5-22. Significant matches of peaks and dips could be seen in all the figures. The results further indicate that resonances occur irrespective of the target and its composition. They also present a challenge to the classification process because the unique signature may well be orientation dependent.
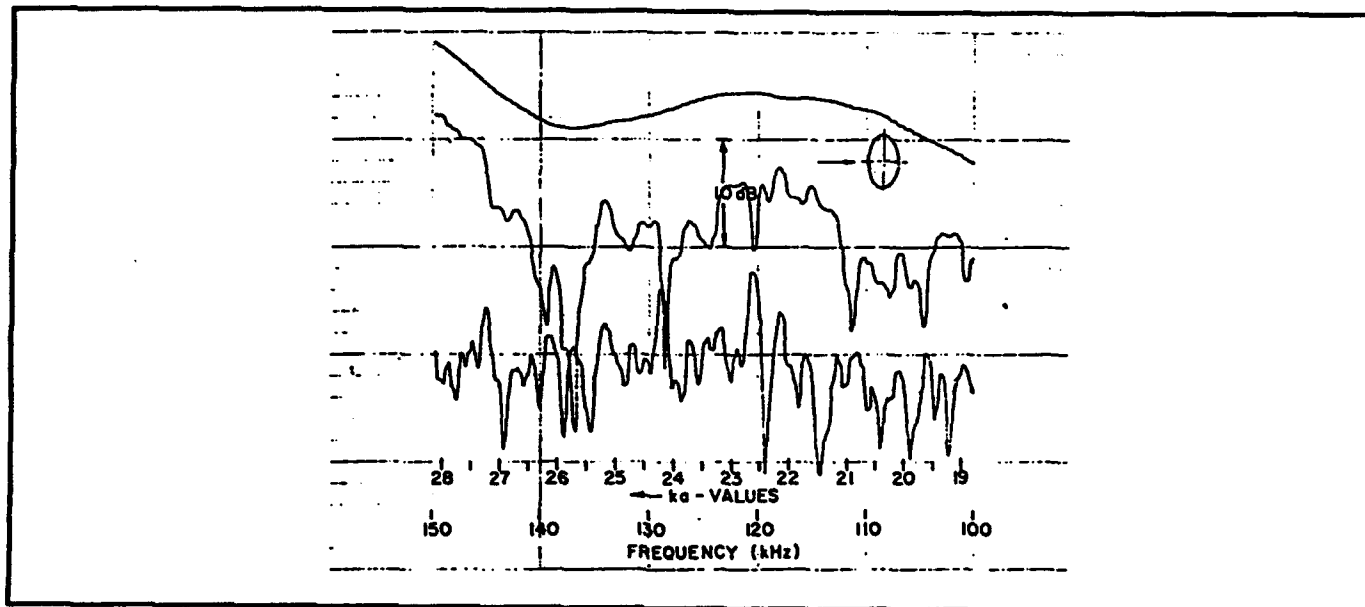
FIGURE 5-20. SPECTROGRAM OF A 3.5" BY 7" SPHEROID AT BROADSIDE
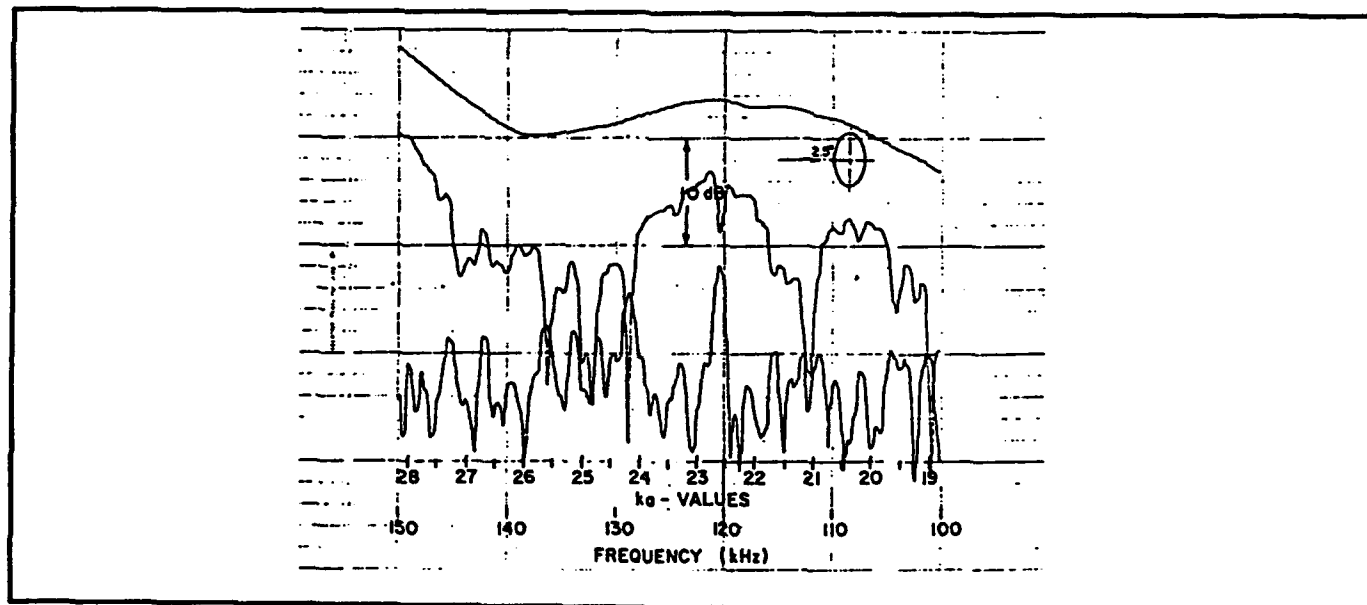
FIGURE 5-21.SPECTROGRAM OF A 3.5" BY 7" SPHEROID AT 2.5° OFF BROADSIDE
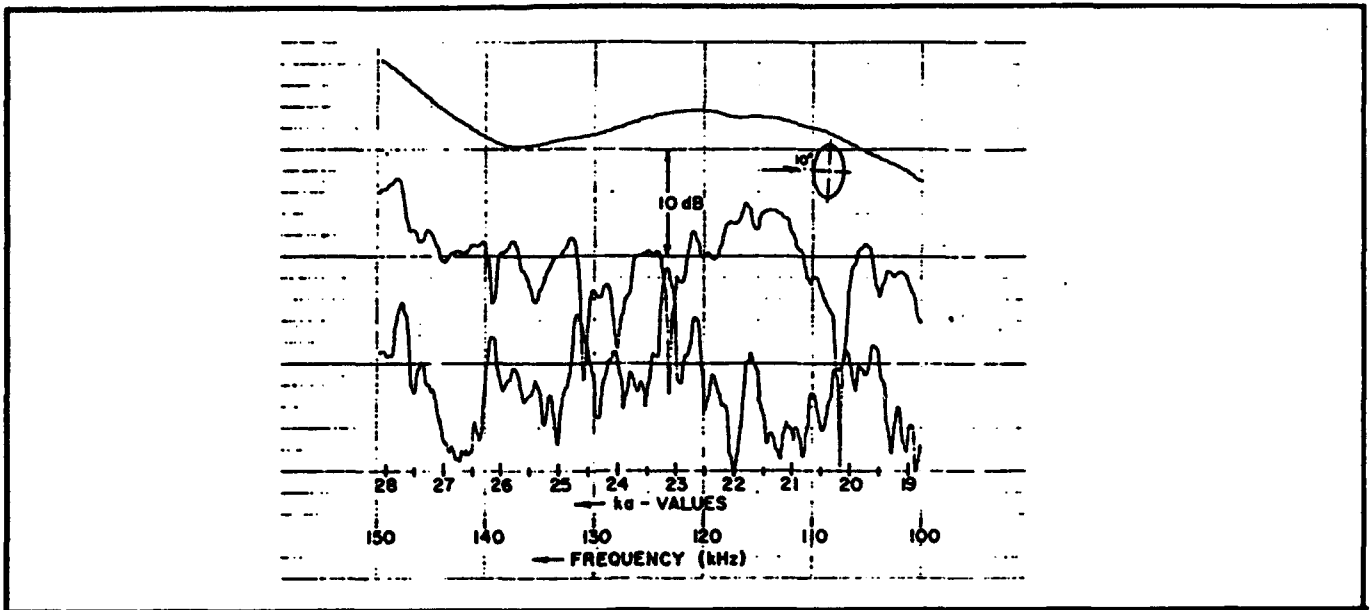
FIGURE 5-22.   SPECTROGRAM OF A 3.5" BY 7" HOLLOW SPHEROID AT 10° OFF
                BROADSIDE

Figure 5-23 is the polar patterns for the target strength and the re-radiated energy from
the hollow brass spheroid at resonance at 101.5kHz at a resonance shown in Figure 5-22.

REFLECTED   RERADIATED
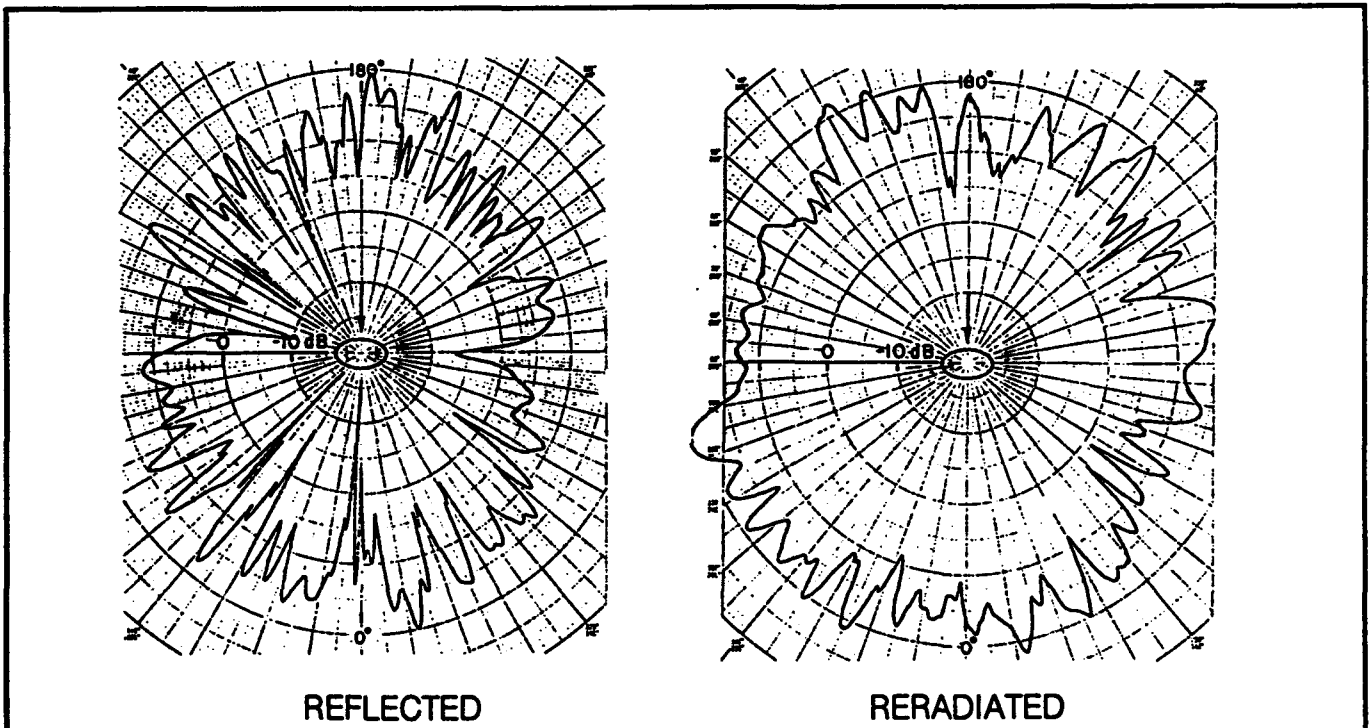
FIGURE 5-23.   REFLECTED AND RERADIATED PATTERN FOR A 3.5" BY 7" HOLLOW
                SPHEROID AT BROADSIDE

The resonance phenomenon can also be observed from the reflected time domain waves. As mentioned at several occasions previously, the envelope of the reflected waves virtually remains rectangular in shape at nonresonant states, but will gradually deviate from it at resonance due to the decrease in amplitude in the trailing cycles. The decrease signifies energy penetration into the elastic target. Moreover, at the end of the reflected pulse with no significant input forthcoming, the sudden burst of signal picked up by the hydrophone is due to the reradiation from the ringing target. Shown in Figure 5-24 are two sets of pictures to illustrate this phenomenon. The three pictures at the left pertain to the 0.74" solid aluminum rod at frequencies of 152, 153 and 154 kHz. The resonance frequency of 153 kHz corresponds to the (1,2) mode at $ka = 6.2$. The three pictures at the right pertain to the 1.5" hollow aluminum tube of ID/OD = 2/3 at frequencies of 285, 286 and 287 kHz. The resonance frequency of 286 kHz corresponds to the (2,3) mode at $ka = 22.7$. Both sets vividly illustrate the transitions towards and away from the resonance with the accompanying decrease in amplitude at the trailing portion of the pulse and the reradiated.
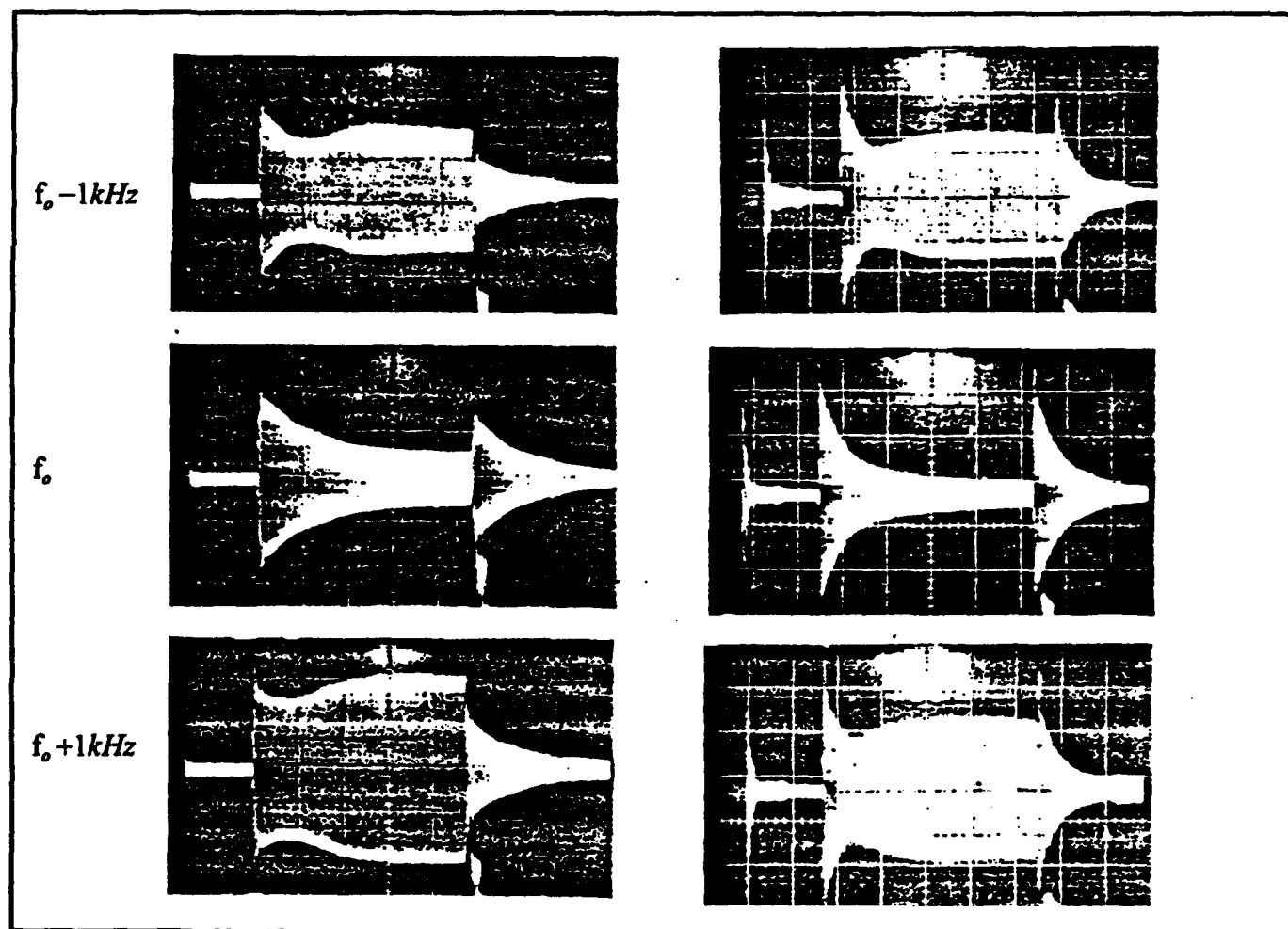

FIGURE 5-24.   REFLECTED AND RERADIATED TIME DOMAIN RESPONSE AT RESONANCE (f_o) AND $f_o \pm$ 1kHz.

Resonances occur at a set of k a values derived from the solution of the characteristic equation, Equation (2-53), where k is the wave number and a is the radius of the target. Since the wave number is proportional to the incident frequency, it is possible to achieve a specific resonance at various incident frequencies by using targets of appropriate sizes. This was indeed done in the experiments. Shown in Figure 5-25 are backscattered and reradiated pulses for the (4,2) resonance with k a = 16.2. The pictures marked (a), (b) and (c) pertain to hollow aluminum tubes of ID/OD = 2/3; of outside diameters of 6", 3", and 1.5" respectively. The corresponding incident frequencies are 52.0, 102.3 and 206.9 kHz. The pictures do not look as dramatic as those shown in Figure 5-25 but nevertheless exhibit the general features pertinent to a resonance state. The deficiencies often resulted from tuning problems and dynamic limitations in the projector and the hydrophone at the resonance frequencies which led to low signal to noise ratio.
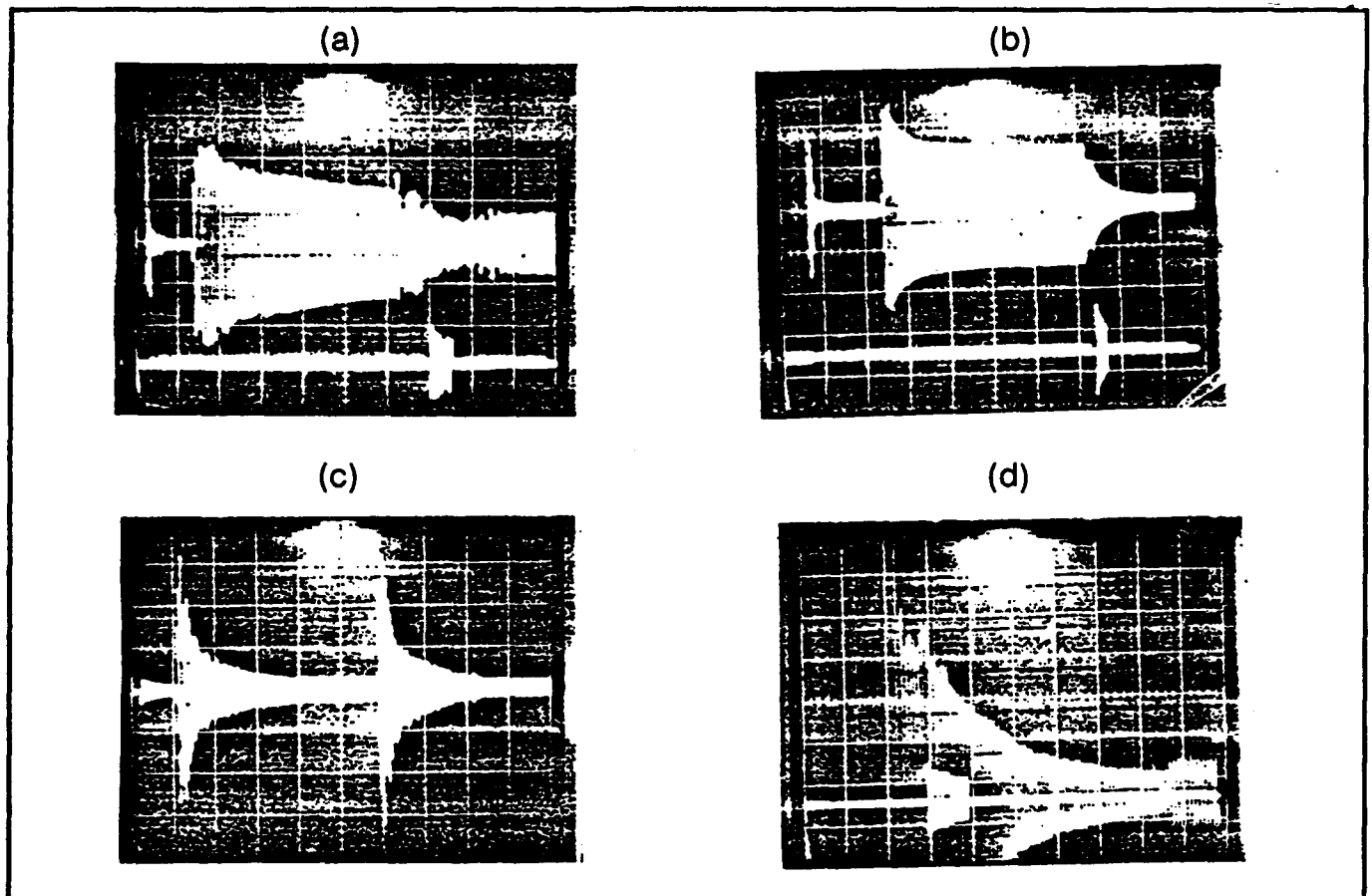
FIGURE 5-25.   REFLECTED AND RERADIATED TIME DOMAIN RESPONSE OF SIMULAR TUBES

The most interesting feature in the pictures is the reradiated pulse which immediately follows the reflected pulse. An enlarged picture of this portion pertaining to Figure 5-25(c) is given in Figure 5-25(d). The reradiated displays the rate of energy transmission to the surrounding inviscid fluid which is governed by the dissipation mechanism of the target.

If the history of the energy dissipation, given by the envelope of the reradiated decay is available, a simple mathematical derivation will show that the damping constant, ζ, can be given by any two amplitudes x_0 and x_m of the envelope, namely:

$$\zeta = \frac{1}{2\pi f \Delta T} \ln(x_0/x_m) \qquad (5-1)$$

where f is the resonance frequency and ΔT is the time lapse for the amplitude decay from x_0 to x_m. By using Equation (5-1) repeatedly over many of these envelopes at various resonances, it is possible to obtain damping information over a wide range of frequencies.

Finally an experiment can be conducted to see if this resonance could be exploited to determine the damping characteristics of a system. Two separate schemes are envisioned. First after partitioning the energy radiated from the system and that dissipated in the system, the damping factor of the material can be determined. The second scheme involves selecting a target with a resonance near the frequency of interest, measuring that resonance for a bare metal target, applying a coating to either the inside or outside dependent on the application, measuring the system with the coating, and finally comparing the results. This comparison can be done in the time domain by measuring the exponential decay of the reradiated energy of in the frequency domain by looking at the change in width of the resonance at the 3-dB down point.

The portion of the time domain signal pertaining to the free ringing can be used to determine the damping constant of the target material. A lightly damped exponential decay curve is presented in Figure 5-26. Several points on the curve are plotted in a semilog plot in Figure 5-27. The result of the plot yielded a damping ratio of 0.072 by Equation (5-1). This is probably a reasonable good value for aluminum but the radiation impedance of the process needs to be established.
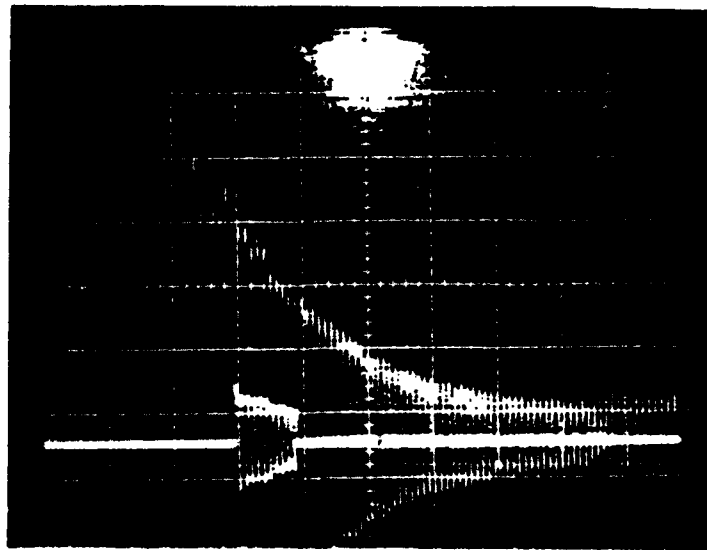
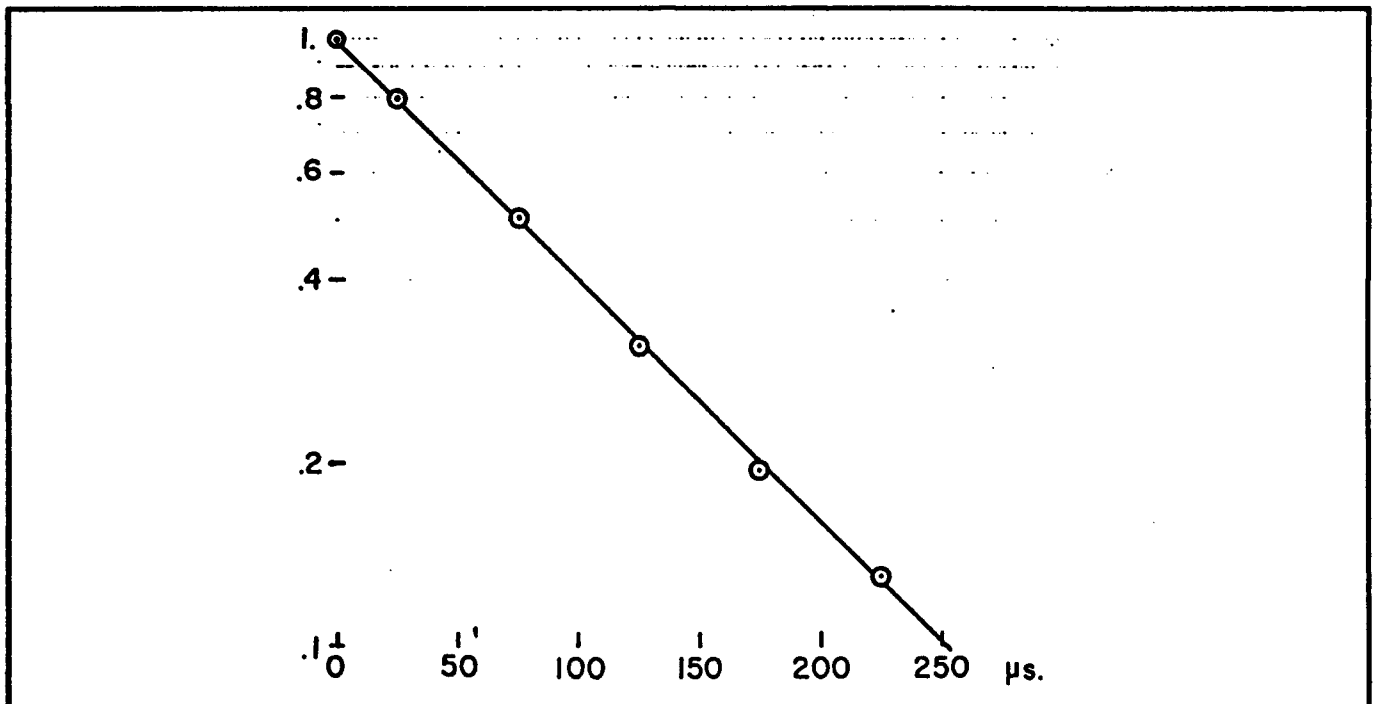FIGURE 5-26. LIGHTLY DAMPED RERADIATED PULSE

FIGURE 5-27. SIMILOG PLOT OF LIGHTLY DAMPED RERADIATED PULSE

CHAPTER 6

CONCLUSIONS AND RECOMMENDATIONS

In conclusion, the theoretical responses of simple shapes were compared to the measured values and the agreement was found to be excellent. More complex structures like spheroids were measured and were also found to have detectable resonances. A cursory review of the frequency dependence of the resonances at angles other than broadside and a scheme to use the resonances to determine the damping characteristics of the targets was completed. This body of experiments has proven beyond a shadow of doubt that the resonances of simple structures can be mathematically determined and that they can be measured. Resonances were measured for solid and hollow cylinders as well as for spheroids. The latter data were presented without analysis. In summary, the following extension of the present experiments is recommended:

The resonances of more complex structures need to be measured. This would involve building several small targets which resemble a target of interest with varied size. The experimentally determined set of resonances would become the "class" signature of that target.

To investigate the application of this scheme for identification of mines, a mine model should be built and tested in the free field and on the bottom to determine how the bottom interaction affects the resonance. It is suspected that an increase in the damping constant will be noted.

Perform additional experiments and analysis on the damping characteristic of metals. This scheme may prove valuable as a means of measuring the damping constant of a fluid loaded coated cylinder.

Finally an investigation of using an insonification pulse that is broadband or band limited in nature. The band of the signal should cover the class signature of the target previously discussed. This scheme should also use the Wigner-Ville distribution scheme to analyze the sonar returns. The Wigner-Ville distribution function is very easy to implement and it determines the time dependence of the frequency domain signal. If intensity modulation is used on a water fall display, bright spots will occur at the frequency where reflection or reradiation are present, and dark spots other places. At frequencies associated with the resonances of the target a bright, dark then bright sequence will occur in a line across the display. If this matches the class signature then a classification can be made. The reverberation will show up as a solid bright line for all frequencies.

The Navy has invested heavily in the task of underwater target classification and identification, and it seemes that this trend will be continued for years to come. The methodology herein developed is a very small part of the overall endeavor and, in the opinion of the authors, has shown promise of fruitful applications in real situations. It deserves close scrutiny for its practicability and potential for future development.

Finally Table 6-1 presents all the resonances that were measured during this research and reported in this report. Many other resonance modes have been determined. "H" signifies a hollow cylinder and "S" a solid cylinder.

TABLE 6-1. EXPERIMENTALLY DETERMINED RESONANCES MODES

Mode #											
1,2	1,3	1,4	2,2	2,3	3,2	3,3	4,2	4,3	5,2	5,3	6,1
H,S	S	S	H,S	H,S	H	H,S	H,S	H	H,S	H	S

REFERENCES

1. Gaunaurd, G. C., "High frequency acoustic scattering from submerged cylindrical shells coated with viscoelastic layers," *J. Acoust. Soc. Am.*, 62, 503-512, 1977.

2. Gaunaurd, G. C. and Uberall, H., "Theory of resona. ce scattering from spherical cavities in elastic and viscoelastic media," *J. Acoust. Soc. Am.*, 63, 1699-1712, 1978.

3. Gaunaurd, G. C. and Uberall, H., "Numerical evaluation of modal resonances in the echoes of compressional waves scattered from fluid-filled spherical cavities in solids," *J. Applied Physics*, 50, 4642-4660, 1979.

4. Gaunaurd, G. C. and Uberall, H., "Suppression of resonant modes from the backscattered echoes of acoustically coated air-filled cylindrical shells in water," Invited paper presented at the *IV (Hydroacoustic) Symp. on Ship-Related Acoustical R & D*, Monterey, CA, Proc. Vol. 1-B, 189-218, 1979

5. Gaunaurd, G. C. and Uberall, H., "Deciphering the scattering code contained in the resonance echoes from fluid filled cavities in solids," *SCIENCE*, 206, 61-64, 1979.

6. Gaunaurd, G. C., Scharnhorst K. P., and Uberall, "Giant monopole resonances in the scattering of waves from air-filled spherical cavities and bubbles," *J. Acoust. Soc. Am.*, 64, 573-594, 1979.

7. Gaunaurd, G. C. and Uberall, H., "Identification of cavity-fillers in elastic solids using resonance scattering theory," *J. Ultrasonics*, 18, 261-269, 1980.

8. Gaunaurd, G. C., "R-Matrix theory of sound scattering from solid spheres via the Mittag-Leffler expansion," *J. Acoust. Soc. Am.*, 68, 1850-1857, 1980.

9. Brill, D., Gaunaurd, G. C., and Uberall, H., "Resonance theory of elastic shear wave-scattering from spherical fluid obstacles inside solids," *J. Acoust. Soc. Am.*, 67, 414-424, 1980.

10. Brill, D., Gaunaurd, G. C., and Uberall, H., "The response surface in elastic wave-scattering," *J. Applied Physics*, 52, 3205-3214, 1981.

11. Uberall, H., Gaunaurd, G. C., and Murphy, J., "Acoustic surface-wave pulses and the ringing of resonances," *J. Acoust. Soc. Am.*, 72, 1014-1017, 1982.

12. Gaunaurd, G. C., and Kalnins, A., "Resonances in the sonar cross sections of coated spherical shells," *Int. J. Solids and Structure*, 18, 1083-1102, 1982.

REFERENCES (Cont.)

13   Brill, D. and Gaunaurd, G. C., "Acoustic resonance scattering by a penetrable cylinder," *J. Acoust. Soc. Am.*, 73, 1448-1455, 1983.

14.   Brill, D., Gaunaurd, G. C., and Uberall, H., "Mechanical eigenfrequencies of axisymmetrical fluid objects: acoustic spectroscopy," *Acoustic*, 53, 11-18, 1983.

15.   Gaunaurd, G. C., Tanglis, H., Uberall, H., and Brill, D., "Interior and exterior resonances in acoustic scattering, Part I: spherical targets," Il Nuovo Cimento, 76B, 153-175, (1983); also "Part II: targets of arbitrary shape," ibid, 77B, 73-86, 1983.

16.   Gaunaurd, G. C. and Uberall, H., "RST analysis of monostatic and bistatic acoustic echoes from an elastic sphere," *J. Acoust. Soc. Am.*, 73, 1-12, 1983.

17.   Jackins, P. D. and Gaunaurd, G. C., "Resonance reflection of acoustic waves by a perforated bilaminar coating model," *J. Acoust. Soc. Am.*, 73, 1456-1463, 1983.

18.   Gaunaurd, G. C. and Brill, D., "Acoustic spectrogram and complex-frequency poles of a resonantly excited elastic tube," 75, 1680-1693, 1984.

19.   Gaunaurd, G. C. and Uberall, H., "Relation between creeping-wave acoustic transients and the complex-frequency poles of the singularity expansion method," *J. Acoust. Soc. Am.*, 78, 234-243, 1985.

20.   Gaunaurd, G. C. and Werby, M., "Resonance response of submerged, acoustically excited thick and thin shells," *J. Acoust. Soc. Am.*, 77, 2081-2093, 1985.

21.   Gaunaurd, G. C. and Werby, M., "Proper background choice in resonance scattering by submerged elastic shells," *Int. J. Solids and Structure*, 22, 1149-1159, 1986

22.   Jackins, P. D. and Gaunaurd, G. C., "Resonance acoustic scattering from stacks of bonded elastic plates," *J. Acoust. Soc. Am.*, 80, 1762-1776, 1986.

23.   Tsui, C. Y., Reid, G. N. and Gaunaurd, G. C., "Resonance scattering by elastic cylinders and its experimental verification," *J. Acoust. Soc. Am.*, 80, 382-390, 1986.

24.   Werby, M. F. and Gaunaurd, G. C., "Transition from soft to rigid behavior in scattering from submerged thin elastic shells," *Acoust. Letters*, 9, No. 7, 89-93, 1986.

25.   Brill, D. and Gaunaurd, G. C., "Resonance theory of elastic waves ultrasonically scattered from an elastic sphere," *J. Acoust. Soc. Am.*, 81, 1-21, 1987.

26.   Gaunaurd, G. C. and Werby, M. F., "Lamb waves in submerged spherical shells resonantly excited by acoustic waves," *J. Acoust. Soc. Am.*, 82, 2021-2033, 1987.

27.   Brill, D. Ayres, V. and Gaunaurd, G. C., "The influence of natural resonances on scattering and radiation process," *J. Washington Academy of Science*, 77, 55, 65, 1987.

28.   Gaunaurd, G. C. and McCarthy, M., "Resonances of elastic bodies in fluid half-spaces," IEEE Jn. of Ocean Engineering, *Special Issue on Scattering*, OE-12, 395-404, 1987.

REFERENCES (Cont.)

29. Gaunaurd, G. C., "Techniques for sonar target-identification," IEEE Jn. of Ocean Engineering, *Special Issue on Scattering*, OE-12, 419-423, 1987.

30. Ayres, V. and Gaunaurd, G. C., "Acoustic resonance scattering by viscoelastic objects," *J. Acoust. Soc. Am.*, 81, 301-311, 1987.

31. Ayres, V. and Gaunaurd, G. C., "Inverse scattering from an elastic sphere," *J. Acoust. Soc. Am.*, 82, 1291-1302, 1987.

32. Ayres, V., Gaunaurd, G. C., Tsui, C. Y. and Werby, M., "The effects of lamb waves on the sonar cross-sections of elastic spherical shells," *Int. J. Solids and Structures*, 23, 937-946, 1987.

33. Gaunaurd, G. C., "Inverse scattering techniques for material characterization," Proc., *Ultrasonics Int. 1987 Congress*, London, Vol. 1, 520-525, 1987.

34. Werby, M. and Gaunaurd, G. C., "Classification of resonances in the scattering from submerged spheroidal shells insonified at arbitrary angles of incidence," *J. Acoust. Soc. Am.*, 82, 1369-1377, 1987.

35. Gaunaurd, G. C. and Tsui, C. Y., "Transient and steady-state target resonance excitation by sound scattering," *Applied Acoustics*, 23, 121-140, 1988.

36. Tsui, C. Y., Reid, G. N. and Gaunaurd, G. C., "Bistatic measurements of target scattering at resonance," *J. Acoust. Soc. Am.*, 83, 1946-1951, 1988.

37. Gaunaurd, G. C. and Uberall, "Resonances in Acoustic and Elastic Wave-scattering," Proc. of Symp. on *Recent Developments in Classical Wave Scattering: Focus on the T-Matrix Approach*, Columbus, OH, Pergamon Press, Varadan, V. K. and Varadan V. V., Editors, 413-430, 1980.

38. Flax, L., Gaunaurd, G. C. and Uberall, H., "The theory of resonance scattering," in *Physical Acoustics*, Vol. 15, Chap. 3, Mason, W. P. and Thurston, R. N., Editors, Academic Press, 191-294, 1981.

39. Gaunaurd, G. C., Uberall, H., Madigosky, W., and Dragonette, L. R., "Inverse scattering and the resonances of viscoelastic and electromagnetic systems," in *Wave Propagation in Viscoelastic Media*, Mainardi, F., Editor, Pitman Ltd., London, 235-257, 1982.

40. Gaunaurd, G. C., Scharnhorst, K., and Uberall, H., "New methods to determine shear absorption," Navy Case 62,944, U. S. Patent 4,249,421 granted on 10 Feb 1981

41. Gaunaurd, G. C. and Uberall, H., "Method to decipher the code indicating material composition contained in the resonance echoes from fluid-filled cavities in solids," Navy Case 63,359, U. S. Patent 4,249,422 granted on 10 Feb 1981.

REFERENCES (Cont.)

42. Gaunaurd, G. C. and Uberall, H., "New method to determine the material composition of dielectrically coated radar targets," Navy Case 64,857, U. S. Patent granted on 15 Nov 1983.

43. Faran, Jr. J. J., "Sound scattering by solid cylinders and spheres," *J. Acoust. Soc. Am.*, 23, 405-416, 1951.

44. Doolittle, R. D., Uberall, H., and Ugincius, P., "Sound scattering by elastic cylinders," *J. Acoust. Soc. Am.*, 43, 1-14, 1968

45. Brill, D. and Uberall, H., "Acoustic waves transmitted through solid elastic cylinders," *J. Acoust. Soc. Am.*, 50, 921-939, 1971.

46. Flax, L., Dragonette, L. R. and Uberall, H., "Theory of elastic resonance excitation by sound scattering," *J. Acoust. Soc. Am.*, 63, 723-731, 1978.

47. Dragonette, L. R., "The influence of the Rayleigh surface wave on the backscattering by submerged aluminum cylinders." *J. Acoust. Soc. Am.*, 65, 1570-1572, 1978.

48. Dragonette, L. R., "Evaluation of the relative importance of circumferential or creeping waves in acoustic scattering from rigid and elastic solid cylinders and cylindrical shells." NRL Report 8216, Naval Research Laboratory, D. C. 20375, 1978.

49. Hickling, R., "Analysis of echoes from a solid elastic sphere in water," *J. Acoustic. Soc. Am.*,34, 1582-1592, 1962

50. Vogt, R. H. and Neubauer, W. G., "Relationship between acoustic reflection and vibrational modes of elastic spheres," *J. Acoust. Soc. Am.*, 60, 15-20, 1976

51. Doolittle, R. D. and Uberall, H., "Sound scattering by elastic cylindrical shells," *J. Acoust. Soc. Am.*, 39, 272-275, 1966

52. Ugincius. P. and Uberall, H., "Creeping-wave analysis of acoustic scattering by elastic cylindrical shell," *J. Acoust. Soc. Am.*, 43, 1025-1035, 1968

53. Murphy, J. D., Breitenbach, E. D., and Uberall, H., Resonance scattering of acoustic waves from cylindrical shells," *J. Acoust. Soc. Am.*, 64, 677-683, 1978

54. Gaunaurd, G. C., "Methods for solving the viscoelasticity equations for cylinder and sphere problem." NSWC Report TR-76-20, Naval Surface Weapon Center, White Oak, Maryland 20910, 1976

55. Junger, M. C. and Feit, D., Sound, Structures, and Their Interactions, Second Edition, The MIT Press, Cambridge, MA., 1986

56. Breit, G. and Wigner, E., "Capture of slow neutrons," *Phys Rev.*, 43, 519, 1936

57. Gerber, H., "The hydroacoustic facility," *NAVSEA Jn.*, 75, 36-40, 1975

REFERENCES (Cont.)

58.   Reid, G. N., NSWC hydroacoustic facility," NSWC Report MP 86-90, Naval Surface
       Weapon Center, White Oak, Maryland, 20903-5000, 1986

DISTRIBUTION

	Copies			Copies

DoD Activities (CONUS)

DEFENSE TECHNICAL   12
INFORMATION CENTER
CAMERON STATION
ALEXANDRIA, VA 22304-6145

ATTN PROFESSOR A. HEALEY 67He 1
       PROFESSOR A. ACTHLEY 61Ay 1
NAVAL POSTGRADUATE SCHOOL
MONTEREY, CA 93943

ATTN PROFESSOR D. BRILL 1
PHYSICS DEPARTMENT
UNITED STATES NAVAL ACADEMY
ANNAPOLIS, MD

ATTN L. DRAGONETTE 1
NAVAL RESEARCH LAB
WASHINGTON, DC 20332

CENTER FOR NAVAL ANALYSIS 1
4401 FORD AVE
PO BOX 16268
ALEXANDRIA, VA 22302-0268

Non DoD Activities

ATTN GIFT AND EXCHANGE DIVISION 4
LIBRARY OF CONGRESS
WASHINGTON, DC 20540

ATTN PROFESSOR J. GILHEANY 1
      PROFESSOR H. UBERALL 1
CATHOLIC UNIVERSITY
WASHINGTON, DC 20011

ATTN LIN KRUPSAW 2
SEAP OFFICE
GEORGE WASHINGTON UNIVERSITY
725 23RD STREET NW
WASHINGTON, DC 20052

ATTN CHUNG TSUI 3
UNIVERSITY OF MARYLAND
COLLEGE PARK, MD 20742

ATTN DR. G. GILETTE STA GROUP 1
JOHNS HOPKINS UNIVERSITY
APPLIED PHYSICS LABORATORY
LAUREL, MD 20725

ATTN DR. GEE-IN GOO 1
ELECTRICAL ENGINEERING DEPT
MORGAN STATE UNIVERSITY
00 QUAINT ACRES DRIVE
SILVER SPRING, MARYLAND 20904

Internal

		Copies
E231		2
E332		3
260	G. REID	3
2620	W. PHELPS	1
2120	A. BOND	2
R34	G. GAUNAURD	1
	R. HARRISON	1
R31	W. MADIGOSKY	1
E29	LIBRARY	4
054	MSC	5